# Understanding the Structural and Functional Correlates of Acute Lung Inflammation in Two Murine Models

A Thesis Submitted to the

College of Graduate and Postdoctoral Studies

In Partial Fulfillment of the Requirements

For the Degree of Master of Science

In the Department of Small Animal and Clinical Sciences

University of Saskatchewan

Saskatoon

By

MANPREET KAUR

## PERMISSION TO USE

In presenting this thesis/dissertation in partial fulfillment of the requirements for a Postgraduate degree from the University of Saskatchewan, I agree that the Libraries of this University may make it freely available for inspection. I further agree that permission for copying of this thesis/dissertation in any manner, in whole or in part, for scholarly purposes may be granted by the professor or professors who supervised my thesis/dissertation work or, in their absence, by the Head of the Department or the Dean of the College in which my thesis work was done. It is understood that any copying or publication or use of this thesis/dissertation or parts thereof for financial gain shall not be allowed without my written permission. It is also understood that due recognition shall be given to me and to the University of Saskatchewan in any scholarly use which may be made of any material in my thesis/dissertation.

## DISCLAIMER

Reference in this thesis/dissertation to any specific commercial products, process, or service by trade name, trademark, manufacturer, or otherwise, does not constitute or imply its endorsement, recommendation, or favoring by the University of Saskatchewan. The views and opinions of the author expressed herein do not state or reflect those of the University of Saskatchewan and shall not be used for advertising or product endorsement purposes.

Requests for permission to copy or to make other uses of materials in this thesis/dissertation in whole or part should be addressed to:

1. Dean

   College of Graduate and Postdoctoral Studies
   University of Saskatchewan
   116 Thorvaldson Building, 110 Science Place
   Saskatoon, Saskatchewan S7N 5C9
   Canada

2. Head of the Department of Small Animal and Clinical Sciences
   Western College of Veterinary Medicine
   University of Saskatchewan
   52 Campus Drive
   Saskatoon, Saskatchewan, S7N 5B4

## ABSTRACT

The outcome of lung inflammation is important to host survival as lungs are necessary for oxygen exchange and fighting pathogens or any injurious stimuli. Thus, diagnosing and understanding the kinetics of lung inflammation is an emerging technological area in the field of imaging research and development. Dr. Aulakh's lab has two separate established models of neutrophilic murine acute lung injury namely, acute low-dose (0.05 ppm) ozone-induced and intranasal bacterial lipopolysaccharide (LPS)-induced lung inflammation. In order to characterize the dynamics of these models, there are two research hypotheses of my project, which are a) acute low-dose ozone exposure causes lung [18F]F-FDG retention because of increased leukocyte glucose uptake due to inflammation as assessed by sequential micro-Positron Emission Tomography-Computed tomography (microPET-CT) in murine lungs, similar to the effects of intranasal bacterial lipopolysaccharide, LPS and b) acute low-dose ozone exposure induces an increase in ultra-small-angle scatter (USAXS) (due to alveolar recruitment), absorption (due to alveolar edema) and a decrease in refraction (due to peri-bronchiolar edema) comparable to intranasal LPS induced changes in these X-ray optical properties as assessed by Lung Multiple Image X-Radiography (MIR). Thus, the premise of my thesis is to test the utility of longitudinal non-invasive imaging modalities, namely sequential [$^{18}$F]-fluoro-deoxy glucose ([18F]F-FDG) positron emission tomography-computed tomography (PET-CT) and synchrotron multiple image X-radiography (MIR), to assess the progression of acute murine low-dose ozone or intranasal bacterial lipopolysaccharide (LPS) induced lung inflammation over 24 and 70 h time periods, respectively. Both ozone and LPS induced an increase in murine lung [18F]F-FDG standard uptake ratio (SUR) and a heterogenous lung distribution which was unlike the craniocaudal [18F]F-FDG gradient observed in lungs before any exposure (called as baseline or control [18F]F-FDG). The whole-body distribution profiles revealed that lung [18F]F-FDG activity was

higher and prolonged up to 28 h in LPS compared to ozone exposed mice. While [18F]F-FDG is a useful marker to highlight areas with high metabolic uptake of glucose in cells such as neutrophils and macrophages recruited during inflammation, the resolution of PET-CT (hundreds of μm) precludes the evaluation of microscopic histopathologic changes especially in the alveoli. Using lung hematoxylin and eosin stained cryosections, the ratios of total lung tissue to air spaces and specifically alveolar parenchyma to air spaces were assessed in mice lungs exposed to 0.05 ppm ozone for 2 h. Results from the X-ray CT lung tissue volume quantifications as well as the histologically derived percent-stained lung or alveolar area quantifications suggest significant damage that is observed as reduced percentage area as well as variability or standard deviation (S.D.) of binary lung images in mice immediately i.e., at 0 h and 6 h after exposure to 2 h of 0.05 ppm ozone. Alveolar damage was also significant at 0 h as shown by reduction in percentage area and S.D. in the binary image region restricted to alveoli. The synchrotron study aimed at following mice lungs before, immediately i.e., at 0 h, and thereafter at 24, 48 or 70 h after saline, bacterial lipopolysaccharide (LPS, 50 μg), or low dose (0.05 ppm for 2 h) ozone exposure. Our results indicate that the lung ultra-small-angle scatter (USAXS), which is a metric of air-tissue boundaries and refraction (which is due to bending of X-rays across air-tissue conducting airways) reduces, especially in the cranial part of left lung, with a corresponding increase in absorption upon exposure to LPS or ozone and is detectable up to 70 h. The changes in lung X-ray optical properties are indicative of the gross inflammatory changes, in response to LPS or ozone exposure, as indicated by increases in lung absorption but reduction in refraction and USAXS. Overall, the results from my project indicate that for a comprehensive analysis of lung inflammation, a combination of lung histological analysis along with objective lung image analysis as described in the longitudinal microPET-CT and lung MIR experiments form powerful

techniques for sensitive delineation of inflammatory changes in gross lung structure and function.

## ACKNOWLEDGEMENTS

I would first like to thank my supervisor, Dr. Gurpreet Aulakh, for giving me the opportunity to join her lab. She has been extremely supportive and has provided valuable guidance throughout my program. I would not have been able to finish my studies without her guidance, support, and patience, for which I am forever grateful. Dr. Aulakh has been most supportive and patient throughout. She always made time for meetings and discussions regarding my project. I am very thankful for all her help and support.

I would also like to acknowledge my committee members, Dr. Monique Mayer and Dr. Shelley Kirychuk for their guidance and patience, the committee chair, Dr. Lynne Sandmeyer, for her support in facilitating committee meetings. They all have provided their valuable perspective into my project.

The current animal design was approved by the University of Saskatchewan's Animal Research Ethics Board (AUP 20170016) and adhered to the Canadian Council on Animal Care guidelines for humane animal use. I would like to thank several people for their technical assistance during my experiments**.** I would like to thank the animal facility staff of the Laboratory Animal Services Unit and Animal Care Unit especially, Brandee Pastoor, for providing immense support in animal care and guiding me through their facilities for my experiments. I would like to acknowledge Eiko Kawamura for her assistance with microscopy and Larhonda Sobchishin for her assistance in brightfield microscopy for histology part. I would also like to thank Jacqueline Cawthray and Debbie Frattinger for providing unparalleled radiation safety measures and Sam Ekanayake and Vanessa Brown for their excellent technical support during the experiments. The research conducted is funded by start-up funds from the Sylvia Fedoruk Canadian Center for

Nuclear Innovation. The Sylvia Fedoruk Canadian Center for Nuclear Innovation is funded by Innovation Saskatchewan. The funding body was not involved in the design of the study and collection, analysis, and interpretation of data and in writing the manuscript. The synchrotron MIR imaging was possible due to the team efforts of Drs. Shelley Kirychuk and Gurpreet Aulakh labs' personnel including tireless efforts by Upkardeep Pandher, Vanessa Brown. Impeccable technical support and beamline expertise by Drs. Arash Panahifar and Adam Webb is duly acknowledged. No words are enough to express our sincere gratitude towards Dr. Dean Chapman for his continued support in data analysis, interpretation, and valuable suggestions for the MIR study.

I am forever grateful to my family for their unconditional love and support throughout. I am thankful to my lab mates for their support and motivation especially Nguyen Phuong Khanh Le and Jessica Brocos Duda. They have been most helpful during difficult times and have been very kind to provide guidance and assistance during my experiments.

## TABLE OF CONTENTS

## TABLE OF FIGURES

## Supplementary Movies

**Movie 1:** Representative 3-d volumetric rendering of the segmented lung [18F]F-FDG volume at baseline. The 3-d render shows [18F]F-FDG activity normalized to16-color scale.

**Movie 2:** Representative 3-d volumetric rendering of the segmented lung [18F]F-FDG volume at 0 h after O3 exposure (0.05 ppm for 2 h). The 3-d render shows [18F]F-FDG activity normalized to16-color scale.

**Movie 3:** Representative 3-d volumetric rendering of the segmented lung [18F]F-FDG volume at 24 h after O3 exposure (0.05 ppm for 2 h). The 3-d render shows [18F]F-FDG activity normalized to16-color scale.

**Movie 4:** Representative 3-d volumetric rendering of the segmented lung [18F]F-FDG volume at 28 h after O3 exposure (0.05 ppm for 2 h). The 3-d render shows [18F]F-FDG activity normalized to16-color scale.

## LIST OF ABBREVIATIONS

| | |
|---|---|
| [18F]F-FDG | [18F]F-FDG (2-deoxy-2-[$^{18}$F] fluoro-D-glucose) |
| ALI | Acute lung injury |
| AP | Antero-posterior |
| ARDS | Acute respiratory distress syndrome |
| AT1 | Alveolar-type 1 |
| BALF | Bronchoalveolar lavage fluid |
| BMIT-BM | Biomedical imaging and therapy-Bending Magnet |
| CLS | Canadian Light Source |
| CT | Computed tomography |
| CT-AC | CT-based attenuation correction |
| DAMPs | Damage-associated molecular patterns |
| DOI | Depth of interaction |
| DEI | Diffraction enhanced imaging |
| ECs | Endothelial cells |
| FOV | Field of view |
| GLUT | Glucose transporters |
| H&E | Hematoxylin and Eosin |

| | |
|---|---|
| IL | Interleukin |
| IP Camera | Internet protocol camera |
| LPS | Lipopolysaccharide |
| PCXI | Phase contrast X-ray imaging |
| PET-CT | Positron emission tomography-computed tomography |
| PET-MR | Positron emission tomography-magnetic resonance hybrid imaging |
| MIR | Multiple Image X-Radiography |
| MODS | Multiple organ dysfunction syndrome |
| MRI | Magnetic resonance imaging |
| NETs | Neutrophil extra-cellular traps |
| O3 | Ozone |
| PMN | Polymorphonuclear neutrophils |
| RAGE | Receptor for advanced glycation end products |
| ROI | Region of interest |
| RT | Radiotherapy |
| S.D. | Standard deviation |
| SPECT | Single photon emission computed tomography |
| SIRS | Systemic inflammatory response syndrome |

| | |
|---|---|
| SUR | Standard Uptake Ratio |
| TLR-4 | Toll like receptor 4 |
| TNFα | Tumor necrosis factor alpha |
| USASX | Ultra-small-angle scatter |
| vWF | Von Willebrand factor |
| ATP ß | ATP synthase complex V subunit ß |
| ROS | Reactive oxygen species |
| SDF-1œ | Stromal cell derived factor 1alpha |
| NF-kB | Nuclear factor-kB signaling pathway |
| IgG | Immunoglobulin G |
| WT | Wild-type |
| SUV | Standard uptake value |

## KEYWORDS

[18F]F-FDG

Acute lung injury (ALI)

LPS

Dynamic lung inflammation

H&E

Image quantification

Lung inflammation

Micro PET/CT

Ozone (O3)

Ozone induced lung inflammation

Positron Emission Tomography (PET-CT)

Synchrotron Multiple Image X-Radiography (MIR)

Regional distribution analysis

Nuclear imaging

# CHAPTER 1: INTRODUCTION AND LITERATURE REVIEW

## 1.1 INTRODUCTION

Lung inflammation is a central feature of lung damage, and its progression is characteristic of respiratory diseases such as acute lung injury (ALI), emphysema, chronic obstructive pulmonary disease and interstitial pulmonary fibrosis to name a few (G. K. Aulakh, 2018; A. M. Groves et al., 2012). Damage to the delicate alveoli, lung tissue and obstruction of the small airways leads to significant inflammation, impaired gas exchange and, ultimately, hypoxemia and shortness of breath (G. K. Aulakh, 2018). These events are commonly diagnosed by lung function studies (Dauchet et al., 2018) as well as by detecting increase in pulmonary vascular permeability, neutrophil recruitment, glucose utilization (G. K. Aulakh et al., 2020b). However, these end-points are also upregulated in diseases such as lung cancers (Hofheinz et al., 2016). Higher hospitalization and mortality burden of acute (including COVID-19 infection) and chronic respiratory diseases points towards an unprecedented need for development of sensitive and efficient imaging tools for evaluation of lung inflammation therapeutics at the pre-clinical stage.

Exposure to ozone (O3), an environmental pollutant, impairs lung function, increases susceptibility to pulmonary infections, and short low-levels of O3 exposures increase the risk of mortality in those with underlying cardiorespiratory conditions (Cakmak et al., 2018; Dauchet et al., 2018; Delfino et al., 1997; Peterson et al., 1978; Rush et al., 2017; Rush et al., 2018; Stieb et al., 1996; Thomson et al., 2018). Thus, exposure to low concentrations of O3 serves as a model of lung inflammation to study fundamental mechanisms of inflammation (Cakmak et al., 2018; Dauchet et al., 2018). Our lab has recently established a murine model of low-dose O3 induced ALI (G. K. Aulakh et al., 2020a). After performing a dose and time-

response to low O3 concentrations, we observed that exposure to 0.05 ppm O3 for 2 h, induces acute lung injury that is marked by lung ATP synthase complex V subunit β (ATPβ) and angiostatin expression, like the LPS model. Intravital lung imaging revealed disorganization of alveolar actin microfilaments indicating lung damage, and ablation of alveolar septal reactive oxygen species (ROS) levels (indicating abrogation of baseline cell signaling) and mitochondrial membrane potential (indicating acute cell death) after 2 h exposure to 0.05 ppm O3 (G. K. Aulakh et al., 2020a), neutrophil recruitment and cytokine release, most notably IL-16 and SDF-1α. The take-home message from our lab's recent studies is that O3 produces exponentially high toxicity when exposed at concentrations below the allowed limits of 0.063 ppm over 8 h (per day) for human exposure. However, these techniques are at best capable of a post-mortem or microscopic analysis of a limited region of lung. These limitations are obvious when understanding the dynamics of lung inflammation which warrants a longitudinal analysis of these events. Sensitive methods to visualize and quantify murine lung adaptations, in response to low-dose (0.05 ppm) O3, a potent environmental pollutant or bacterial lipopolysaccharide, a TLR4 agonist, are crucial in order to understand the host inflammatory and repair mechanisms. Thus, my research project was designed to correlate the lung inflammatory changes between two different functional imaging techniques, namely, microPET-CT using [18F]F-FDG as the PET tracer and projection based functional multiple image X-radiography (MIR) using synchrotron X-rays.

In further coming sections, I will provide literature review of the anatomy and function of lung, our current understanding of the lung inflammation, animal models of lung inflammation, namely LPS and O3 induced lung inflammation, and finally animal imaging of

lung inflammation, with focus on synchrotron multiple image X-radiography (MIR) and nuclear imaging.

## 1.2 MAMMALIAN LUNG ANATOMY AND FUNCTION

Mammalian lungs are part of the lower respiratory tract that begins at the trachea and branches into the bronchi and bronchioles. They are largely divided into bronchopulmonary segments and pulmonary lobules (Ellis, 2011). The trachea divides into right and left bronchi to supply the respective lungs. The right primary bronchus divides into secondary bronchi from which bronchioles originate. The mammalian lungs have a double arterial supply with both pulmonary and bronchial arteries. This unique vascular design enables receiving deoxygenated blood from the heart to the pulmonary circulation for the purpose of receiving oxygen and releasing carbon dioxide and a separate supply of oxygenated blood to the tissues of the lungs in the bronchial circulation. Finally, the lungs of rodents are covered by a thin membranous pleura and thus is comprised of a single left lobe and four right lobes.

The study of respiratory system reveals a significant inter-species difference in airway branching patterns in rodent lungs as compared to the structure of the human lungs, because rodent lung displays single airway branching patterns. The pattern of the branching conducting airways is notably different in the humans. Local branching patterns are unique which reflect the asymmetry and the degree of expansion at each bifurcation, the ratio of the length of each branch to its diameter. Thus, differences between lungs of rodents and humans exists in both gross anatomy and histology of the lungs. The anatomy of the bronchial circulation varies across species (Miller et al., 1993). Bronchial circulation plays an important role in acute airway responses and airway defence against airborne pathogens (Suresh et al., 2016). Recruitment of inflammatory cells that participate in immune function

to the airway mucosa also occurs in acute inflammatory or chronic lung diseases. In relation to single occurrence where particulate matter causes pulmonary infarcts, the bronchial circulation provides collateral blood flow to the lungs. However, animal models transplanted with bronchial artery revascularisation show improved airway oxygenation compared to traditional transplant despite these structural differences (Rojas et al., 2005). The main role of the respiratory circulation is to deliver the entire cardiac output as a thin film of blood to the terminal respiratory units where gas exchange takes place. In human adult lungs, factors controlling pulmonary blood flow include vascular structure, mechanical effects of breathing and the influence of humoral factors (Suresh & Shimoda, 2016).

Lung is a highly quiescent tissue and lung has a remarkable reparative capacity. During ALI multiple factors such as the activation of inflammatory cells and release of inflammatory factors lead to damage of air-blood barrier. In the rodent lungs, several stem cells niches are important in maintaining the epithelial layers of lung tissue (Donne et al., 2015). After ALI, the milieu of the damaged tissue will determine the rate and nature of alveolar epithelial repair and is therefore considered to be of great interest. The pulmonary endothelial cells (ECs) are an essential component of the gas exchange machinery of the lung alveolus. Animal lungs are filled with tiny air sacs known as alveoli where the gas swap occurs, that preserves the animal's movement. The small blood vessels known as capillaries come in close contact with the alveoli allowing oxygen to be extracted from the air into the blood and carbon dioxide to be discharged from the blood into the air (Cheung et al., 2018). The primary function of the respiratory system is to exchange oxygen and other gases with the external environment. The functional compartment or niche responsible for gas exchange in the lungs is called alveolus and is comprised of multiple epithelial, endothelial, and

mesenchymal cell lineages. Alveolar epithelium has two types of cells which includes: Type 1 which are flat and elongated cells and Type 2 which are cuboidal cells that produce surfactant. The pulmonary vascular plexus interacts intimately with alveolar type 1 (AT1) cells to form a very thin gas diffusible interface. The lung alveolus and its gas exchange function are seriously disrupted upon acute lung injury such as occurs during a viral infection. The clinical features of ALI include acute hypoxemic respiratory failure and bilateral pulmonary infiltrates that are not attributable to left heart failure. During ALI, inflammatory cells particularly polymorphonuclear neutrophil (PMNs) come into close contact with lung alveolar epithelial cells (Niethamer et al., 2020). Alveoli are the terminal spaces which are lined by alveolar septum. Alveolar septum has alveolar epithelial cells and capillary endothelial cells. The oxygen and carbon dioxide exchange occurs across this septum.

The blood flow is very slow through the lung capillaries and many times immune cells such as neutrophils pass slowly. Lung alveoli also have important cells called alveolar macrophages. Alveolar macrophages protect the alveolar epithelium from inhaled particulate material or infection agents (Charo et al., 2006). Macrophages contribute to acute and chronic inflammatory responses releasing both pro- and anti-inflammatory mediators as well as angiogenic, mitogenic and under pathological conditions, profibrotic proteins (Driscoll et al., 1987).

The size of the lungs varies depending on age, sex, height, and ethnicity (Suresh & Shimoda, 2016) as supported by reports showing 3-fold more mortality in older patients; also more susceptible mouse strain such as C57BL/6NJ vs the C57BL/6J (G. K. Aulakh et al., 2020a; Thiesse et al., 2010). More studies are required to be enlarged to different animal

models and animal strains within one species to consider for the inter-individual genetic variability and to different species including primates that best reflect the structural characteristics and developmental stages of lungs in humans (Yao et al., 2018).

## 1.3 LUNG INFLAMMATION

Inflammation is a body's response to physical, chemical, or biological insults. Inflammation is characterized by heat, redness, swelling and loss of function. There is increased flow of blood to the site of injury to provide more energy (that is why the inflamed area is hot) and the immune cells to fight infection. The site of inflammation swells because of the leakiness of the capillaries and venules leading to edema formation. The inflammatory cells such as neutrophils move from blood circulation into the inflamed tissue. Neutrophils first attach to the endothelium and then crawl out of the capillaries. Their activation and movement is guided by chemical mediators called selectins, chemokines and consequent interactions with integrins containing β1 and β2 subunits (Ley et al., 2007). When acute inflammation becomes chronic, there are fewer neutrophils but more monocytes and macrophages that resolve the acute inflammation and restore organ function (Barreiro et al., 2010).The outcome of lung inflammation depend on the cause of the inflammation. The inflammatory response is regulated by the nuclear factor-kB (NF-kB) signaling pathway (Mitchell et al., 2016).

In humans, lung inflammation can refer to infection of the lung itself or thin membranes, the pleura, that covers the lungs and lines the chest cavity. This infectious condition is commonly known as pneumonia, which is a leading cause in which the lung tissue itself becomes infected due to bacteria or viruses which could lead to acute respiratory distress syndrome (ARDS). Lung inflammation is also defined as pneumonitis, which may be due to any non-infectious reasons causing alveoli which are tiny balloon shaped air sacs to become inflamed which makes it hard

for oxygen to directly flow across the alveoli into the blood stream (Netea et al., 2017). Thus, ALI may develop from direct (pulmonary) reasons e.g., in pneumonia aspiration of the gastric content, near drowning, inhalation of toxic gases etc. or from indirect (extrapulmonary) reasons because of significant systemic injury like in sepsis, severe trauma with shock or pancreatitis (Cereda et al., 2019). The features of ARDS pathophysiology include poorly regulated inflammation, unsuitable growth, starting with aggregates of leukocytes and platelets, spontaneous activation of coagulation pathways and altered permeability of alveolar-capillary barrier (Han et al., 2015).

There are also extra differences between the direct and indirect forms of ALI/ARDS. In direct ALI/ARDS the injury is more fixed to the alveolar epithelial cells with alveolar collapse, aggregation of neutrophils, fibrin deposition, formation of hyaline membranes and alveolar wall oedema (Cheung et al., 2018). On the other hand, in indirect ALI/ARDS the injury to endothelial cells is more scattered and it is the typical finding of interstitial oedema and smaller lung accumulation of neutrophils in comparison to the direct form (Cheung et al., 2018). Besides, in the direct form of ALI/ARDS concentrations of pro-inflammatory cytokines TNFα, IL-1β, IL-6 and IL-8 increases in the bronchoalveolar lavage fluid (BALF) or lung tissue homogenates while in the indirect form of ALI/ARDS increased cytokines levels are revealed mostly in the plasma indicating that the lung injury was induced due to the action of mediators released from extrapulmonary foci into the systemic circulation (Matute-Bello et al., 2008). Regarding an initial injury to the epithelial cells in the direct ALI/ARDS surfactant protein D has been identified as an important marker of injury to type II alveolar cells and a receptor for an advanced glycation end products (RAGE) as a marker of type I alveolar cells injury. The damage of endothelial cells and systemic inflammation which are more prominent in the indirect

ALI/ARDS can be confirmed by increased plasma levels of von Willebrand factor (vWf), IL-6. The progression of ARDS can be characterized into three phases which includes exudative, proliferative and fibrotic phases. The starting or exudative phase day (1–7) is characterized by a diffuse alveolar damage of epithelial and endothelial cells which release various factors leading to the injury and cell death. The loss of unity of alveolar-capillary barrier leads to rushing of the alveoli with proteinaceous fluid and dilution of pulmonary surfactant. The interstitial and intra-alveolar lung oedema decreases lung compliance and impairs gas exchange. Damage to the lung tissue is related with massive movement of immune cells into the unhealthy lung as well. The activated neutrophils, alveolar macrophages and fixed lung cells produce huge quantities of pro-inflammatory substances e.g., IL-1β, IL-6, IL-8, TNFα and proteases leading to further aggravation of the lung tissue injury. In a mouse sepsis model, IL-6 was established to be linked with increased mortality and increased lung complement 5 a receptor expression (Kasahara et al., 2014; Mishra et al., 2016). IL-6 is secreted by immune cells and lung endothelial, epithelial cells in response to environmental insults. The overproduction of oxidants and decrease in antioxidants leads to oxidation changes and cross-linking of proteins, lipids, DNA, carbohydrates, deterioration of cell structures and their function, increased endothelial receptiveness, lung oedema development, pulmonary epithelial dysfunction with reduced sodium ion transport and fluid reabsorption from the alveoli etc. Moreover, due to intrinsically generated oxidants derived from phagocytic cells, recruited neutrophils and residential lung macrophages and alveolar epithelial and endothelial cells, an additional main source of oxidants is the in-take of high concentrations of oxygen used for mechanical ventilation of patients with severe ARDS conditions. Within several days the exudative phase freely proceeds to a proliferative phase that is distinguished by the diffuse pattern of pulmonary oedema and restoration of damaged tissue by

proliferation and phenotypic changes in type II alveolar cells, myofibroblasts, fibroblasts and new proteins are deposited. In the absence of retrieval, the situation in some patients sometimes reaches to a fibrotic stage distinguished by diffuse fibrosis and irreversible changes of lung architecture. In direct lung injury, the noxious stimulus mainly hits the lung structures and the activation of the innate immune response by binding of the microbial products or cell-injury related endogenous molecules like (danger-associated molecular patterns DAMPs) to the pattern recognition receptors e.g. Toll-like receptors (TLRs) on the lung epithelium and alveolar macrophages prompt an acute lung inflammation (Morgan et al., 2020). An extra immune effector mechanism leading to the tissue injury, neutrophil extracellular traps (NETs), extracellular histones and granular proteins (e.g., neutrophil elastase and myeloperoxidase) established by dying neutrophils have been recognized. The freed histones major proteins of chromosomes are extremely cytotoxic and act as DAMPs further producing epithelial and endothelial cell death. When entering the circulation histones stimulate platelets which promote recruitment of neutrophils and aggravate systemic inflammation. However, numerous substances like pro-inflammatory cytokines TNFα and IL-1β, high-mobility group box 1 protein, mitochondrial DNA also act as DAMPs and produce lung inflammation and ARDS. The systemic leukocyte activation can lead to systemic inflammatory response syndrome (SIRS), multiple organ dysfunction syndrome (MODS) and multiple organ failure.

Thus, the progression of lung inflammation is incumbent upon the status of pro- and anti-inflammatory processes and imaging the kinetics of lung inflammation in animal models can enhance our current understanding of the inflammatory components.

## 1.4 ANIMAL MODELS OF LUNG INFLAMMATION

In small animals such as rodents, lung injury can be induced by infectious such as bacteria, viruses as well as non-infectious (or sterile) agents such as hyperoxia, ventilator induced high pressure, O3, bacterial lipopolysaccharide (intranasal, intravenous or intraperitoneal), hydrochloric acid, oleic acid or ischemia-reperfusion to name a few (Matute-Bello et al., 2008). Rodents, e.g., mice, rats, ferrets and hamsters serve as useful small animals to model mammalian lung inflammation. Mice are a reductionist model species which is in keeping with the 3R principles for testing our research hypothesis in mammalian species (Matute-Bello et al., 2011). Finally, due to the availability of generic and conditional knock-out as well as specific pathogen free mice, molecular mechanisms can be tested making these as the animal of choice in pre-clinical research (Matute-Bello et al., 2011; Matute-Bello et al., 2008; Moitra et al., 2008).

Male sex has been associated as a risk factor for multiple morbidities associated with preterm birth, including bronchopulmonary dysplasia as well in adult mice exposed to innate immune stimulants such as LPS(Larcombe et al., 2011; Moitra et al., 2008; Nguyen et al., 2019). On the other hand, the incidence of autoimmune syndromes display a strong a female bias (Markle et al., 2013); females have been announced to release higher leukotriene levels which correlate with airway hyperreactivity, pulmonary inflammation and mast cell activation and recruitment in response to allergens (Rossi et al., 2019). By using the same sex mice, the number and variability is supposed to be lower compared to mix sex mice groups. To minimize such variabilities in lung inflammatory phenotypes, I planned my imaging experiments with young i.e., 6-8 week old male C57BL/6J mice. Although mice are naturally nocturnal animals, I had to resort to a day-time design of my experiments (owing to repeated time-dependent imaging in a limited amount of time window, involved in our study design) and included appropriate controls to account for the additional stress due to treatments given during the day (Nolan et al., 2021). In

the further coming two sub-sections, I will discuss the characteristics of LPS and O3 induced murine lung inflammation.

### 1.4.1 Lipopolysaccharides (LPS) induced lung inflammation

The lipopolysaccharide (LPS), which is known as lipoglycans, made up of large molecules comprising of a lipid and a polysaccharide attached by covalent bond; they are found in the outer membrane of Gram-negative bacteria. LPS also acts as endotoxins and produces strong immune responses in animals, and it is also considered as the predominant inducer of inflammatory responses in these bacteria. The recognition of LPS by cells of the innate immune system provides an important first step to identify invading pathogens and to initiate a protective response. LPS promotes barrier disruption via initiating derangements of extracellular endothelial components as observed in models of murine lung injury, human pulmonary endothelial cells (Nieman et al., 2020; Rizzo et al., 2020).

Lipopolysaccharide extracted from pathogenic micro-organisms including E. coli and P. aeruginosa is often used as an endotoxin to induce ALI in animal models. We need to understand the pathology of acute lung injury although ARDS is a complex syndrome. It features four well-accepted central components known as the pathologic tetrad namely capillary congestion, atelectasis, intra-alveolar hemorrhage, and alveolar edema which if unchecked will lead to loss surfactant function you should list all the components of the tetrad (Thompson et al., 2017). The resultant high alveolar surface tension will exacerbate the permeability-induced increase in alveolar flooding with edema fluid. Surfactant dysfunction will alter alveolar mechanics resulting in alveolar recruitment and de-recruitment with each breath (Beitler et al., 2019). Each component of the tetrad has a profound impact on alveolar mechanics. Lung injury can also be induced by shear forces from regional differences in lung mechanics. Adjacent alveoli share an

interalveolar septum and are mechanically inter-dependent. When one alveolus is collapsed, or fluid-filled and an adjacent alveolus is aerated their shared interalveolar septum stretches to shift toward the non-aerated alveolus (Dong et al., 2018). Other animal models utilize intrapulmonary deposition of immunoglobulin (IgG) immune complexes which trigger an intense inflammatory reaction which is identified by the rush of polymorphonuclear neutrophils (PMN), interstitial and alveolar edema. During inflammatory states, neutrophils enter the lung by exiting from the vasculature through crossing the endothelial barrier at the capillary level. Infiltrating immune cells including T and B cells, macrophages, and mast cells have also been observed in the vascular lesions in, for example, Pulmonary Arterial Hypertension (Hu et al., 2020). Macrophages and mast cells also play critical role in promoting vascular dysfunction in animal models of pulmonary hypertension.

The toll like receptor (TLR) family plays a key role in pathogen recognition and activation of innate immunity (Takeda et al., 2015). Once activated by stimuli, TLR's family performs corresponding response by stimulating a cascade of various distinct events. TLR-4's exogenous ligands include LPS. Accumulating evidence has showed that toll like receptor-4 (TLR4) stimulated by LPS can induce acute lung injury by activating TLR4/ NF-kB associated with inflammatory response. The neutrophils and macrophages are the important inflammatory cells in acute lung injury (Kenyon et al., 2006). These cells infiltrate into the lung tissues releasing enzymes and phagocytizing the pathogen. In LPS induced inflammation neutrophils and macrophages are activated. After activation, neutrophils and macrophages were recruited to the inflammation site. Additionally, pro-inflammatory cytokines including TNF-a, IL-1b, IL-8, IL-6, and IL-17 are main factors causing inflammatory response and their activation is key to accelerate disease progression in animal models as well as human subjects. TLR4 could identify

pathogenic micro-organisms in a natural immune system, bind the specific ligand and generate corresponding inflammation following identification (Lou et al., 2019).

That much of the pathogenesis of ALI is due to endothelial cell injury which guides to increased vascular receptiveness and extensive inflammatory pulmonary infiltrates and because ALI is one of the most repeated causes of morbidity and mortality in critically ill patients there is a need for novel therapeutic targets. Tissue factor dependent coagulation contributes to lung inflammation and the pathogenesis of ALI which is a clinical syndrome identified by diffuse interstitial pulmonary and non-cardiogenic pulmonary edema that results in severe hypoxemia and dyspnea. For instance, the infusion of endotoxin or bacteria into the vascular space to activate inflammation is quickly followed by intravascular coagulation that is activated by enhanced tissue factor activity (Mumby et al., 2019).

Using the intranasal lipopolysaccharide (LPS) model, it is possible to measure and characterize cellular profile of recruited leukocytes to the lung airways as well as the levels of pro-inflammatory cytokines (G. K. Aulakh et al., 2014; Meyerholz et al., 2017; Szarka et al., 1997). Even more important is the capacity to image these events non-invasively. Therefore, I embark upon non-invasive imaging of mice exposed to intranasal LPS.

### 1.4.2 Ozone (O3) induced lung inflammation

Ozone (O3) is a poisonous and highly reactive gaseous oxidizing chemical with factual adverse health effects in humans. Inhaled O3 does not enter cells but reacts with components of the airway lining fluid to generate other reactive oxygen species to enhance local inflammation and epithelial cell injury. The secondary oxidation products activate the airway epithelium to enhance inflammatory signaling pathways and induce several pro-inflammatory pathways in

airway epithelium (Zychowski et al., 2016). Controlled human exposure to O3 causes decrements in lung function, increased lung neutrophilia and increased airway levels of pro-inflammatory cytokines. Apart from respiratory manifestations, O3 increases sensitivity to lung infections, and even increases the risk of death in those with underlying cardiorespiratory conditions (Låg et al., 2020; Zychowski et al., 2016). Based on animal and human evidence, environmental analysis and air quality standards suggest a threshold for disclosure of no more than 0.063 ppm of O3 (daily concentrations) (Heuss et al., 1971). The experiments done in animal models have shown that O3 induces acute lung injury, albeit at much higher and longer O3 exposures (near 2 ppm for 3-6 h). Acute exposure of animals to high levels of O3 causes characteristic pathogenic responses in the airway and lung parenchyma and allow elucidation of the key transcriptional mechanisms of inflammation. Thus, it is crucial to understand the biological effects of O3 at concentrations feasible in the environment. Exposure to low concentrations of O3 mimics ALI and enables the study of fundamental mechanisms of inflammation. Dr. Aulakh's lab has standardized a sensitive model of sterile murine lung inflammation by exposing mice for two hours at 0.05 ppm O3, a level below the current recommendations for what is considered a safe or "ambient" O3 concentration for humans (Gurpreet K Aulakh et al., 2019; Brocos et al., 2019).

Innate immunity plays an important role against infection and oxidative damage from inhaled air pollutants including O3. Acute airway responses to inhaled ground-level O3 are distinguished by recruitment of inflammatory cells to the lung epithelium and by the production of inflammatory mediators including cytokines, chemokines, and adhesive molecules (Hollingsworth et al., 2007; Manzer et al., 2008). Cytokines have thus been implicated as potential mediators of lung oxidative injury. Recent studies have shown induction of acute phase

cytokines including IL-1, IL-2, IL-6, IL-8, and TNF-a as well as the neutrophil chemotactic factors such as keratinocyte derived chemokine, MIP-2 and LPS induced CXC chemokine following O3 exposure (G. K. Aulakh et al., 2020a; Tighe et al., 2011). The downstream activation of pro-inflammatory factors plays an important role in response to ambient O3. At the cellular level, an inflammatory focus is mainly identified by recruitment of neutrophils which is afterwards replaced by inflammatory monocytes and T-cells. IL-6 also plays a key role in both acute and chronic inflammation and can dictate the profile of leucocyte recruitment during the inflammatory response via selective regulation of inflammatory chemokines/cytokines and apoptotic events (Kasahara et al., 2014). Macrophages from elderly rodents release increased quantities of cytokines which amplify their pro-inflammatory activity; sex-based differences in IL-6 and its receptor levels have also been reported in response to O3 (Angela M. Groves et al., 2013; Mishra et al., 2016). Studies indicate the analytical role of mediators including IL-1, IL-17, and IL-33 in driving O3 effects on airway inflammation. There are differences in the responses of cells and animals to particulate matter and O3 (Bouthillier et al., 1998). Both particulate matter and O3 can activate membrane receptors, intracellular kinases particularly NF-kB and phosphatases that regulate inflammatory responses (Bouthillier et al., 1998). O3 impacts on airway hyper-responsiveness and neutrophilic inflammation through activation of TLR2 and TLR 4 (Mishra et al., 2016). In addition, there is a priming effect of O3 on the innate immune response as exemplified by enhanced TLR2, TLR4 and TLR1 expression and functional responses to their respective agonists (Au - Duda et al., 2021; Mumby et al., 2019). Ambient O3 exposure results in impaired antibacterial host defense in part related to disruption of epithelial barrier and effective phagocytosis of pathogens. The functional response to ambient O3 is dependent on many components of the innate immune signaling (Angela M. Groves et al., 2013).

A combination of structural cells including epithelial cells and resident immune cells such as macrophages are critical for the lung innate immune response to O3. IL-33 is critical in mediating O3 effects in murine models. Respiratory effects of O3 in mice are well characterized (Zychowski et al., 2016) however vascular pathology including pulmonary hypertensive effects from O3 exposure has not been explored at ambient O3 concentrations.

Acute O3 exposure has known deleterious effects on the respiratory system and has been linked with respiratory disease and infection (Mokra et al., 2019). Both severe damage to the bronchial- alveolar epithelium and malfunctioning of bronchial-blood barrier have been largely attributed to the pathobiology of O3 induced inflammatory response (Driscoll et al., 1987). Exposure to O3 even within the safe concentration range, as per the standard definition by environmental protection organization, can affect breathing and lung function and impair pulmonary innate immunity (Devlin et al., 1991). Acute O3 exposure and manifestation of clinical respiratory systems can mainly be allocated to development of cytotoxic outcome and acute cellular injury between oxidative stress giving rise to biochemical and physiological changes in the lung epithelium (G. K. Aulakh et al., 2020a; Devlin et al., 1991; Hollingsworth et al., 2007). These are interposed by an increased production of reactive oxygen species, accumulation of oxidized biomolecules and activation of inflammatory process both locally and systemically (Giuranno et al., 2019).The malfunction of the bronchial-alveolar epithelium and bronchial-blood barrier due to loss of coherence of tight junctions may expand immune cell infiltration and inflammatory response (G. K. Aulakh et al., 2020a; Broeckaert et al., 1999).

Diffuse alveolar injury generation of lung oedema, neutrophil mediated inflammation and ventilation-perfusion mismatch decrease lung compliance and cause profound hypoxemia. Intravital lung imaging reveals disorganization of alveolar actin microfilaments, and a drop in

reactive oxygen species (ROS) and mitochondrial membrane potential (i.e., cell death) after 2 h exposure to 50 ppb O3 which correlates with lung neutrophil recruitment and cytokine release (G. K. Aulakh et al., 2020a). $^{18}$[18F]F-FDG (Fluorodeoxyglucose) microPET/CT imaging is a sensitive method to detect lung cancer and study various inflammatory diseases. The current quantification methods focus on tracer kinetics and compartment modelling with methods such as the Patlak method (D. L. Chen et al., 2009). For understanding disease progression and regional tracer uptake kinetics in relation to specific organs such as lungs, we developed an imaging protocol cum image analysis strategy to quantify the sequential uptake and distribution of [18F]F-FDG in murine lungs. We applied this novel methodology to track changes in the lung [18F]F-FDG uptake before as well as after O3 exposure by sequential [18F]F-FDG imaging.

## 1.5 IMAGING LUNG INFLAMMATION

Animals have been used for many years as research models to study the physiological changes in relation to human diseases including those of the lung. There are many ways to study lung inflammation. Most of the methods involve imaging of the lung either within the living animal or after collection of the lung samples. There are two main categories of pre-clinical imaging modalities, namely structural (such as X-ray i.e. radiographic planar and CT-based techniques (absorption or phase contrast-based X-ray imaging (PCXI), magnetic resonance imaging i.e. MRI)) and functional or molecular imaging techniques (such as microPET/SPECT-CT, MRI, optical imaging modalities) (Ehsan Samei, 2019). The hybrid imaging techniques, which can combine structural and functional modalities, have greatly improved our investigative research abilities to study various experimental models of human diseases in rodents (Schuster et al., 2004).

**1.5.1.1 Structural imaging techniques:** X-ray imaging is commonly done to identify organs and detect anomalies to ensure the accurate detection of a disease. Applying sensitive and specific imaging techniques helps in visualization and diagnosis of the disease affected area (Morton et al., 2017). An enormous amount of useful anatomical spatial information is generated from measured differences in tissue absorbance of X-radiation as it moves through the body from an external source (Behnke et al., 2020).These differences in tissue absorbance especially for soft tissues such as the lungs are largely the result of variations in tissue density.

Unlike imaging in humans, small animal imaging always requires anaesthesia to maintain the animal in one position without movement. Imaging is mainly performed in anaesthetized animals by replacing blood sampling and other painful interventional techniques so that anatomical and functional information can be easily interpreted. Anaesthesia lasting longer than 10-15 minutes may result in hypothermia in rodents. Considering the time-period between imaging sessions, it also depends upon the animal's tolerance to anaesthesia and the half-life of the contrast agents.

Computed tomography (CT) is another anatomical imaging method where a narrow beam of X-rays is passed through the subject and then quickly rotated around the body thereby generating transmission signals and then these signals are prepared and reconstructed to form cross sectional images of the subject under investigation. CT is a tomographic imaging method that gives us the adjoining axial images which can be stacked digitally together to form 3-dimensional, high-resolution images of the investigated area. The diagnostic CT imaging is based on the measurement of X-ray absorption from many different view angles across the patient. CT systems offer a sub-second rotation time and can acquire multiple slices at the same time thereby covering a longitudinal range of 2 cm to 16 cm during a single rotation (Sam Bayat

et al., 2020). CT also gives an isotropic spatial resolution of about 0.5 mm and the physical property that is displayed in CT is the outcome distribution of the linear attenuation coefficients and here the contrast injection is commonly coexist with the acquisition of the CT scan to make sure that sufficient contrast in the organ of interest during the short time of scanning and functional properties can also be assessed with CT by performing dynamic perfusion scans a 4D acquisition is carry out by repeatedly imaging the same region of interest in accordance of 3 s to 5 s time lapses for about 30 s post administration of the contrast agent. By using the so called "time attenuation curve" main hemodynamic parameters can be acquired such as the blood flow, blood volume, the permeability surface area product and these functional parameters have been correlated with histopathology and therapy response. In computed tomography (CT), the radiation dose experienced by an animal is related to the desired resolution of the image, the number and duration of scans and the energy of the X-ray used. Good practices in rodent handling are critical for preparing and monitoring animals post imaging (Koo et al., 2006). The modern CT systems comprise up to 100 detector rows, and it allows for routine acquisitions with spatial resolution of 0.5 mm within scans which take less than a second to a few seconds at a dose value ranges of sub mSv (millisievert) to 15 mSv. The CT images are highly quantitative and reproducible and come with very good contrast resolution compared to other imaging methods e.g., CT and PET. MRI have the natural advantage of providing multifaceted and excellent image contrast especially for soft tissues by not utilizing ionizing radiation. Using Synchrotron based X-ray CT imaging in rats, the development of the conducting airways has been visualized (Sam Bayat et al., 2020; S. Bayat et al., 2009).

Lung do not appreciably absorb X-ray energies of the range of 35-45 keV, due to the lack enough tissue. This produced very little absorption contrast in conventional planar lung X-ray

images. X-ray CT is able to delineate the soft tissue contrast in lungs, but this is accompanied by enormous radiation exposure. In contrast to X-ray CT, multiple image radiography (MIR) provides the best soft tissue determination and is used for high resolution anatomic and functional imaging. MIR is an imaging tool that provides unique tissue contrast with high spatial resolution which helps in the assessment of lung functions.

#### 1.5.1.2 Synchrotron Multiple Image X-Radiography (MIR) Imaging

Synchrotron sources provide highly collimated and powerful bright beams with linear polarization, circular polarization for special devices. The wavelength of synchrotron X-rays can be adjusted over a large spectral range. The emission of synchrotron sources is highly coherent producing detectable diffraction and interference phenomena that can be used for imaging. A useful source of synchrotron radiation is a storage ring which uses many bending magnets to maintain an electron beam at relativistic speeds in a closed trajectory. By bending the electron path x-rays are emitted at each bending magnet in a direction that is tangential to the beam trajectory. The resulting X-rays are emitted as dozens of thin beams each directed toward a beamline next to the accelerator. A horizontal line of un-monochromatized synchrotron radiation goes through a specially designed double-crystal monochromator, that produces two fan shaped beams with the two desired wavelengths. The monochromatic x-ray energy can be adjusted by the monochromator to 15–25 keV to produce high contrast images of the lung specimens (Wysokinski et al., 2016). Synchrotron-based X-ray imaging yields images with high spatial resolution ranging from several micrometers approximately 5 μm to tens of nanometers approximately 30 nm depending on the wavelength and devices. The synchrotron light source exhibits excellent focusing properties through partial coherence based on very short wavelengths ($10^{-7}$-$10^{-10}$ m) and diffraction (Wysokinski et al., 2016; Zhong et al., 2000) along with

remarkably capacity to produce monochromatic X-ray beams at energies that are comfortable for imaging biological samples and producing phase contrast.

X-ray phase contrast imaging (PCXI) is a standard tool for the non-destructive inspection of the internal structure of samples. The X-rays crossing the sample are subjected to different amount of absorption in different parts of the samples. By means of phase contrast-sensitive techniques it is possible to generate contrast in relation to the phase shifts transmitted by the sample and to increase the potential of X-ray imaging to those facts that lack enough absorption contrast to be visualized in conventional radiography. The phase of the waves moving through the sample contributes to the modulation of the detected intensity in an x-ray phase contrast imaging system. This can be expressed by means of the complex refractive index (Lewis et al., 2005). Phase contrast techniques utilize the phase disturbances introduced by the sample to correct the potency recorded at the image receptor in efficient way that these effects can be detected and interpreted (Schuster et al., 2004). Absorption imaging is a transmission type imaging method in which the image receptor looks at the source and between the sample. The internal structure of the specimen can be examined in such manner because the dissimilarity in the diminishing of the x-rays along their trajectories from the generator to the receptor produce contrast. Diffraction enhanced imaging is a new x-ray radiographic imaging modality using monochromatic x-rays from a synchrotron which produces images of thick absorbing objects that are almost completely free of scatter. There are various ways to achieve phase contrast, namely x-ray interferometry, diffraction enhanced imaging, in-line holography, coded aperture x-ray imaging, and grating-based interferometry (Bech et al., 2013; Bravin et al., 2012). Small animal physiology studies are typically complicated, but the level of complexity is greatly increased when performing live-animal X-ray imaging studies at synchrotron. This requires equipment

modified for physiological monitoring and test substance delivery as well as shuttering to reduce the radiation dose. The PCXI methods are specifically sensitive in detecting interfaces between soft tissue and air by which the lungs and airways can be clearly envision. One challenge while imaging living soft tissue structures like the lungs is that the continual motion of the tissue which are captured rapidly leads to a blurry image projection (Bravin et al., 2012). This challenge is accentuated in small lab animals e.g., mice which are often used in research studies because a detector with reduced pixel size will need longer exposures to get the exact statistics in each pixel and hence the same image quality and the small pixels also mean that a visually insignificant movement of only a few micrometers can result in motion blur across a few pixels. These difficulties are addressed by high-flux synchrotron X-ray sources which can provide very high intensity small-area X-ray beams compared with conventional X-ray sources. This high flux enables researchers to capture high speed videos to envision not just the structure but also the function by capturing changes in the tissue. The second advantage of synchrotron X-ray beams is the connected high coherence which means smaller and more fine features can be seen in the sample. Imaging of the mice and rats is typically performed at 25–30 keV and these energies balance enough penetration of the X-ray beam through the animal to the detector which are used at high energies with the effects of phase and absorption contrast which are seen at low energies. The synchrotron X-ray beam has a fixed location and a horizontal direction of propagation which can affect the plan of experiments that's why the careful location of the animal is therefore essential in producing a clear view of the exact anatomy and to minimize the presence of overlying bone or tissues in the beam and to get the anterior–posterior (AP) images of the lungs of rodents the animals position must be held head high hang by their incisors which we have achieved with the use of custom designed 3D printed holders or physical maneuvers to

appropriately support the weight of the animal because this is not a normal physiological position for these animals (G. K. Aulakh et al., 2018). The monochromatic light selected exhibits excellent focusing characteristics through coherence-based interference and contributes to greater resolution. Therefore, it is possible to obtain high resolution images of very small objects and to image internal microstructure of materials. The synchrotron radiation has proven to be a powerful high resolution imaging tool. The synchrotron radiation micro-CT has been used for high resolution lung specimen imaging (Evangelista et al., 2020). Medical research conducted using synchrotron radiation can promote the development of cutting-edge medical technology for global applications (Rao et al., 2006).

However, experiments should be designed in such a way that the radiation doses are maintained to the acceptable levels for longitudinal studies to be performed. Since the animals are isolated in a radiation shielding enclosure during imaging, high magnification remote controlled IP cameras can be used to visually confirm the animal's status throughout the experiments (Kusmirek et al., 2020). This kind of system allows comprehensive remote monitoring of the animal and image acquisition parameters from outside the X-ray imaging radiation enclosure. Synchrotron beamlines are carefully designed to deliver high X-ray flux because while conducting imaging experiments it is important to be mindful of the radiation dose. Synchrotron X-ray sources has a low divergence, so the beam size does not change remarkably through the imaging setup.

A setup of a diffraction-enhanced imaging (DEI) system uses synchrotron x-rays, silicon crystals: one crystal oriented to select a specific beam energy band which is approximately 30 keV in our case. A second crystal called as analyzer crystal, similar to the monochromator, diffracts the transmitted beam, and acts as sensitive angular filter (with scatter rejection optics) to

produce images of the gradients of the refractive indices of samples (Chapman et al., 1997; Johnston et al., 1996), in addition to x-ray absorption and scattering by the object. Algorithms have been established to decompose the images into separate refraction and apparent absorption components (Chapman et al., 2006; Chapman et al., 1997; Glendon et al., 2013; Rhoades et al., 2015). Both planar and CT modalities have been applied in DEI mode to visualize weakly absorbing features of soft tissue, albeit free of scattering (Chapman et al., 1998; Rhoades et al., 2015). Multiple image X-radiography (MIR) is an improved version of DEI, which simultaneously solves for the X-ray optical properties namely absorption, refraction, and ultra-small-angle scatter (USAXS) images (Khelashvili et al., 2006; Wernick et al., 2003). The angular intensity spectrum describes the beam intensity as a function of angle, which contains the information for the three X-ray optical properties. The USAXS parameter provides microstructural details of objects as exemplified by robust studies on scattering phantoms of multiple thickness which reveal that the MIR parameters are analyzed pixel by pixel and are shown to successfully decompose the three X-ray optical properties (Khelashvili et al., 2006).

Lungs serve as an ideal organ for imaging through MIR due to the air-tissue interfaces of alveoli, conducting airways and the weakly attenuating lung parenchyma. Thus, USAXS, which is dependent on air-tissue boundaries, is hypothesized to be directly proportional to the number of air-filled alveoli. However, seminal studies conducted in a mouse model of acute lung inflammation, showed that the USAXS contrast ratio increased during the initial 9 h after exposure to 80 μg of bacterial lipopolysaccharide (LPS), indicating a more complex alveolar mechanics at work following acute lung injury (G. K. Aulakh et al., 2018). Nevertheless, there was a reduction in the refraction contrast ratio, and an increase in the absorption contrast ratio,

indicating accumulation of fluid and compromised air-tissue interface in the conducting airways (G. K. Aulakh et al., 2018).

Thus, synchrotron MIR imaging allows for the sensitive evaluation of gross changes in lungs exposed to inflammation or carcinogens offering the prospective for longitudinal and accurate estimation of pathological events as well as the response to and the effectiveness of therapies while reducing the number of animals required in research.

#### 1.5.2.1 Functional/Molecular imaging techniques

The importance of animal models to human diseases in an area of intense scientific discussion. The extent to which mouse models of lung injury recapitulate human lung injury has been extensively critiqued (Matute-Bello et al., 2011; Matute-Bello et al., 2008; Proudfoot et al., 2011). Neutrophils are enriched in both animal and human lung injury. The experimental work done in animal models, mostly rodents, presume that animal models of lung injury can lead to understanding into the human clinical condition but there is dispute over the degree to which animal models repeat human disease in acute illness at a molecular level (Neudecker et al., 2017). There are respective possible models of experimental lung injury in animals which makes extrapolating results from any individual study difficult. The degrees to which animal models of lung injury are like one another and whether any animal models recapitulate human lung injury are thus open questions. A new creation of imaging devices now makes it possible to create both structural and functional pictures for the study of lung biology in small animals including common laboratory mouse and rat models. Images from more than one technique can also be fused allowing structure–function and function–function relationships to be studied on an anatomic regional basis. These newly emerging suite of techniques called “molecular imaging” provides exceptional depth for elucidating lung biology (Sweeney et al., 2017), and has proven

to identify, follow and evaluate biologic processes at the cellular and subcellular level in intact organisms (Min et al., 2008). The molecular imaging methods can target and track cells, molecules or antigens late hours showing dynamic cellular processes for instance, immune activation and response. For example, it is now achievable to evaluate with imaging the distribution, magnitude, and timing of gene expression in genetically altered animals (Min & Gambhir, 2008). Also, molecular imaging can provide a seamless translation from studies in animals to later studies in humans and vice-versa. Molecular imaging of the earliest events related to the development of acute lung injury (ALI) could facilitate therapeutic development and patient management in inflammatory lung diseases (D. L. Chen et al., 2009).

Single Photon Emission Computed Tomography i.e., SPECT and Positron Emission Tomography i.e., PET, are tomographic techniques in which computer-generated image of local radioactive tracer distribution in tissues is produced through the detection of single photo emissions (in case of SPECT) or annihilation events due to positron emission (in case of PET) from specific radionuclides introduced into the body (Delphine L. Chen et al., 2017). Acquisition of both SPECT and CT (SPECT-CT) further improves accuracy and provides 3-dimensional anatomic reference. SPECT-CT imaging is often used with improved image quality and accuracy. The SPECT (single-photon emission computed tomography) use a gamma camera or multiple gamma cameras that rotate around the patient obtaining multiple 2-D images (projections). The SPECT scans have been viewed as slices in the transverse, sagittal or coronal dimensions and for cardiac applications reoriented into oblique short end or long axis slices. It significantly improves image contrast and can separate the overlapping structures. The advantage of SPECT scanning lies in improved quantification of cardiac function and for cancer mass discovery and for the quantification of radioisotope uptake in clinics as well as animal models

(Ehsan Samei, 2019). In human SPECT imaging, projection views are acquired at uniformly separate angles around the long axis of the patient developing in images with rows and columns of equidistant sample areas.

The SPECT to planar images helps to localize the abnormal uptake improves diagnostic accuracy and assessment of the disease extent. SPECT-CT further improves detection of abnormal radiotracer accumulation (Meinel et al., 2013). SPECT scan takes about 12–20 min. The effective doses from CT portion of SPECT-CT exam were reported as 0.6–2.6 mSv depending on body area imaged (Ehsan Samei, 2019). PET and SPECT tracers have been advanced aiming for early detection and monitoring of disease activity.

Nuclear medicine imaging can be both highly sensitive and highly specific but gives images of the tracer allocation that are of lower spatial resolution than that from CT or MRI, given the fundamental differences in their molecular vs anatomical modalities. The general disputes of localizing focal uptakes of highly specific tracers has led to the evolution of hybrid imaging methods which includes the merger of PET-CT, SPECT-CT or PET-MRI. The PET is a non-invasive imaging technique that gives us visual and assessible information on molecular pathways and here the imaging is performed post injection of a radiotracer which in the case of PET is a biomolecule labelled with a neutron-deficient radioisotope. The tracer idea gives us the power to trace few residues of a biomolecule of interest for example glucose with a radioactive isotope which allows the radioactive tracer to give us the information of the region of interest by means of the emitted radiation without disturbing normal tissue function. PET-CT is playing an important role in development of precision medicine leading to improved therapies and lung cancer patient outcomes (Guo et al., 2022).

Image resolution is determined by the size of the imaging detector elements which is of 3 mm in clinical and 1 mm in pre-clinical PET systems and the related imaging outcome is somewhat lower due to harmful effects from positron range effects which usually varies depending on the energy of the positron emitted from the detector penetration and depth of interaction (DOI). It can also be affected by image reorganization and respiratory physiological movement during acquisition and regardless of the final image resolution of PET being lower compared to MRI or CT lesions with a less diameter than that of the theoretical image resolution it can still be detected if their contrast is sufficiently high. In PET-CT the importance of CT has been added for the purpose of CT based attenuation correction (CT-AC) and scatter correction. A key challenge to high quality and assessable PET is its physiological motion including respiratory and cardiac motion that may cause noticeable contradictions between the PET and CT images and blurring due of the PET images (Gradl et al., 2019). Advanced scanner designs allow for larger coverage of axial FOVs the new PET-CT systems allows shorter acquisition times by lowering the administered radiotracer amount and the easily repeated imaging of any region of the body. First, it increases responsiveness which can be interpreted into higher image quality or can be used for a reduced injected activity and secondly it increases the scanner's throughput by reducing acquisition time. A total body PET-CT scan can then be performed in one minute or less and with a remarkably reduced amount of administered radiotracer which accordingly reduces radiation exposure of the subject.

PET/SPECT-CT studies involve collecting a background scan, transmission scan and a series of emission scans. The background and transmission scans are performed to correct emission scans for errors in the measurement of tissue activity introduced by tissue attenuation because activity attenuation is directly related to tissue density (Ehsan Samei, 2019). The

transmission scan also provides a density image resembling a standard x-ray computed tomography image which was used to define anatomic regions of interest (Delphine L. Chen et al., 2017). PET provides faster scan speeds and better image quality due to its higher sensitivity and spatial resolution compared with SPECT. PET scan requires approximately 10 min i.e., two bed positions at 5 min each. The main component of image analysis is to take the images of defined regions of interest, visualize and quantify the changes encountered in that region in relation to specific injury or inflammation.

The functional imaging modalities have enabled researchers to recognize viable lung regions. This analysis judged the feasibility of nuclear medicine imaging to avoid doses to the functional lung in radiotherapy (RT) planning for patients and RT planning with nuclear functional lung imaging has potential to reduce radiation-induced lung injury. The local lung function and distribution have been set out to be quantitatively visualized with various functional imaging methods such as single photon emission computed tomography (SPECT), positron emission tomography (PET). Among functional lung images used for RT planning SPECT images provided a unique quantitative 3-dimensional map of the distribution of functioning pulmonary vascular/alveolar subunits for the first time. Historically, patients who were to receive radiation therapy for various portions of tumor affected lung , the healthy lung would be incidentally irradiated and prospectively studied (Marks et al., 1997). Regional function was assessed pre- and post-radiation therapy with SPECT lung perfusion scans obtained following the intravenous administration of tracers such as technetium ($^{99m}$Tc)-labelled macroaggregated human albumin (Bajc et al., 2010). Pre-radiation therapy computed tomography CT scans were used to calculate the 3-D dose distribution reflecting tissue density in homogeneity corrections.

Each SPECT scan was correlated with the pre-CT scan and the 3-D dose distribution (Marks et al., 1997).

MRI is non-invasive and does not rely on ionizing radiation like CT. Approaches with a lower MRI magnetic field strength have the disadvantage of lower signal to noise and reduced contrast enhancement. Systems with higher magnetic field strength have superior image quality. However, magnetic fields affect radiation dose distribution, and this effect is amplified with higher magnetic field strengths especially if the MRI magnetic field is oriented perpendicular to the radiation beam (Rubinstein et al., 2018). Magnetic fields do impact radiobiological damage, in lungs (characterized by acute syndrome, radiation induced pneumonitis followed by chronic radiation induced fibrosis) because magnetic field outcomes cause larger dose disturbances in homogenous target areas. Radiation induced lung injury has unique clinical histopathologic and radiographic characteristics. Studies have shown a correlation between radiation induced lung toxicity occurring as a result of depletion in arterialized blood and occurring after exposure to radiation changes in the lungs using thoracic imaging (Rubinstein et al., 2018). The respiratory rate has also shown to be correlated with histological changes in the lungs after irradiation and is often used as non-invasive technique to measure radiation induced lung damage in mice (Rubinstein et al., 2018). The radiation therapy is an important treatment modality for multiple thoracic malignancies. However, radiation induced lung injury which is the term normally used to describe damage to the lungs caused by exposure to ionizing radiation remains an interpretative issue affecting both tumor control and patient quality of life. The radiation pneumonitis typically occurs within three months after radiation therapy and is pathologically characterized across diverse grades by numerous infiltrating inflammatory cells in the edema interval of broken alveolar and in the bronchus (Nieman et al., 2020).

By following the onset of stand-alone anatomical and functional imaging there is a push towards integrating molecular image information through various methods including anatomical-metabolic imaging e.g., PET/CT advanced MRI, optical or ultrasound imaging (Eling et al., 2019).

### 1.5.2.2 Nuclear Imaging of Lung Injury

The conventional PET radiotracer is a glucose analog, 2-deoxy-2-[$^{18}$F] fluoro-D-glucose ([18F]F-FDG), which is the most widely used radiopharmaceutical to date (Jamar et al., 2013). FDG or [18F]F-FDG, mainly used in oncological imaging studies, can also detect various cells taking part in infectious and inflammatory conditions even with a low quality (Jamar et al., 2013). The engaged inflammatory cells increase the expression of glucose transporters (GLUT 1, GLUT 3). Moreover, cytokines and growth factors released in inflammatory sites increase the affinity of glucose transporters for the deoxy glucose. [18F]F-FDG uptake is proportional to the cellular metabolic rate and binds to cells such as neutrophils, lymphocytes, and macrophages. The fasting can be an effective way to ensure uniformity in fluorodeoxyglucose ([18F]F-FDG) PET imaging, especially by decreasing blood glucose levels. [18F]F-FDG-PET can quantify lung inflammation levels and may thus be a useful biomarker of inflammatory cell activity. [18F]F-FDG uptake can be detected when neutrophils are activated and sequestered within the lungs before their trans-endothelial migration into airways. Previous studies have indicated the infiltration of neutrophils may represent the major component of [18F]F-FDG uptake in lung parenchyma in ALI (Rodrigues et al., 2017). Methods to quantify early neutrophil activation and recruitment would be valuable in informing the development and efficacy of novel therapies. The [18F]F-FDG uptake by the lungs has been shown to correlate with neutrophil influx into the lungs in a variety of experimental pulmonary inflammation lesions (Lorente et al., 2012; Serkova

et al., 2008). Increases in X-ray computed tomographic (CT) attenuation values in the lungs could theoretically increase quantitative or semi-quantitative measurements of [18F]F-FDG activity. PET with [18F]F-FDG has been used to monitor cellular metabolic activity which in the setting of lung inflammation is believed to reflect the presence and activity of inflammatory cells.

Review data evaluating [18F]F-FDG PET quantification approaches in lung diseases focus on methods to account for variations in lung components and the interpretation of the derived parameters (Delphine L. Chen et al., 2017). The [18F]F-FDG signals within each pre-defined region of interest in the lungs represents the contribution of activity in parenchymal (alveolar) airway wall, vascular wall (endothelial) and immune cells as well as blood and water. The ideal parameter quantifying [18F]F-FDG lung uptake would reflect metabolic activity only from the cells thought to contribute to lung disease progression namely the metabolically activated lung cells (recruited leukocytes and activated parenchymal cells) to determine their pathogenic role. In PET imaging [18F]F-FDG can be used for the assessment of glucose metabolism in the heart, lungs, and the brain (de Prost et al., 2010).

Thus, PET imaging with [18F]F-FDG has emerged as a non-invasive and highly sensitive imaging technique to quantify pulmonary inflammation (Pourfathi et al., 2020). [18F]F-FDG-PET may serve as marker of level of disease activity in ALI.

The purpose of using two imaging techniques (the synchrotron MIR X-ray and PET-CT), in my project, is to evaluate the lung inflammation progression, as visualized through projection-based functional lung X-ray optical properties and the 3-dimensional distribution of [18F]F-FDG in mice exposed to LPS or O3 and thus contribute towards diagnostic strategies for evaluation of lung injury/inflammation.

# CHAPTER 2

## 2.1 HYPOTHESES

1. Acute low-dose O3 exposure causes lung [18F]F-FDG retention (increased leukocyte glucose uptake due to inflammation) upon sequential micro-Positron Emission Tomography-Computed tomography, microPET-CT, in murine lungs similar to the effects of bacterial lipopolysaccharide, LPS.

2. Acute low-dose O3 exposure induces an increase in lung scatter (alveolar recruitment), absorption (alveolar edema) and a decrease in refraction (peri-bronchiolar edema) comparable to LPS induced changes in the X-ray optical properties (Lung Multiple Image X-Radiography, MIR) mimicking murine acute lung inflammation.

## 2.2 OBJECTIVES

The following are specific objectives of my thesis:

1) to test the utility of longitudinal non-invasive imaging modalities, namely sequential [$^{18}$F]-fluoro-deoxy glucose ([18F]F-FDG) positron emission tomography-computed tomography (PET-CT) and synchrotron multiple image X-radiography (MIR), to assess the progression of acute murine low-dose O3 or bacterial lipopolysaccharide (LPS) induced lung inflammation over time 24 and 70 h time periods respectively for sensitive delineation of inflammatory changes in gross lung structure and function.

2) The synchrotron study aimed at delineating time-dependent changes in lung inflammation by following mice before, immediately i.e., at 0 h, and thereafter at 24, 48 or 70 h after

saline, bacterial lipopolysaccharide (LPS, 50 μg), or low dose (0.05 ppm for 2 h) O3 acute exposure.

The next chapter (Chapter 3) is the first manuscript from microPET-CT in line with my first hypothesis and objective just mentioned.

# CHAPTER 3

## (Thesis Manuscript 1)

## Quantification of Regional Murine Ozone- or LPS-Induced Lung Inflammation Using [18F]F-FDG MicroPET/CT Imaging

**Authors:** Gurpreet Kaur Aulakh[1*], Manpreet Kaur[1], Vanessa Brown[1], Samanthan Ekanayake[1], Behlol Khan[2] & Humphrey Fonge[2,3]

**Affiliations:** [1]Western College of Veterinary Medicine, University of Saskatchewan, Saskatoon, Canada. [2]College of Medicine, University of Saskatchewan, Saskatoon, Canada. [3]Department of Medical Imaging, RUH Saskatoon, Saskatoon.

Canada. *Email: gurpreet.aulakh@usask.ca

**Author contributions:** Manpreet Kaur (40%), Behlol Khan, Gurpreet Aulakh and Humphrey Fonge designed the study and the imaging protocol. Vanessa Brown, Samantha Ekanayake and Gurpreet Aulakh executed the experiments. Manpreet Kaur (60%), Gurpreet Aulakh and Humphrey Fonge analyzed the results and wrote the manuscript. All the authors have read and edited the manuscript.

**Additional information:** Supplementary information is available for the published paper, "Quantification of regional murine O3-induced lung inflammation using [18F]F-FDG microPET/CT imaging" at https://doi.org/10.1038/s41598-020-72832-8.

## 3.1 ABSTRACT

Ozone (O3) is a highly potent and reactive air pollutant. It has been linked to acute and chronic respiratory diseases in humans by inducing inflammation. Our studies have found evidence that 0.05 ppm of O3, within the threshold of air quality standards, is capable of inducing acute lung injury. LPS, i.e., bacterial polysaccharide, is a known Toll-like receptor-4 (TLR-4) mediated innate immune activator, which causes acute lung inflammation. This study was undertaken to examine O3- or LPS-induced lung damage using [18F]F-FDG (2-deoxy-2-[$^{18}$F] fluoro-D-glucose) microPET/CT imaging in wild-type mice (model). [18F]F-FDG is a known PET tracer for inflammation. Sequential [18F]F-FDG microPET/CT imaging was performed at baseline (i.e., before O3 or LPS exposure), immediately (0 h), at 24 h and at 28 h following 2 h of 0.05 ppm O3 or intranasal LPS (50µg/50µl) exposure. The images were quantified to determine spatial standard uptake ratio of [18F]F-FDG in relation to lung tissue density and compared with baseline values. LPS induced predictable lung [18F]F-FDG uptake up to 28 h (% lung [18F]F-FDG SUR of 1.3-1.7 at baseline vs 1.54 -2.01 at 28 h). Immediately after O3 exposure, we detected a 72.21±0.79% increase in lung [18F]F-FDG uptake ratio when compared to baseline measures, indicating lung metabolic cellular activation. At 24 h post-O3 exposure, the [18F]F-FDG uptake becomes highly variable (S.D. in [18F]F-FDG = 5.174 X $10^{-4}$ units) with a 42.54±0.33% increase in lung [18F]F-FDG compared to baseline. At 28 h time-point, [18F]F-FDG uptake ratio was similar to baseline values. However, the pattern of [18F]F-FDG distribution varied and was interspersed with zones of minimal uptake. Our microPET/CT imaging protocol can quantify and identify atypical regional lung uptake of [18F]F-FDG to understand lung response to O3 or LPS exposure.

**Keywords:** [18F]F-FDG; microPET/CT; O3; LPS; lung inflammation; dynamic lung imaging; regional distribution analysis

## 3.2 INTRODUCTION

Ozone (O3) is a toxic and highly reactive gaseous oxidizing chemical with well-documented adverse health effects in humans. On the basis of animal and human data, environmental guidelines and air quality standards recommend a threshold for exposure of no more than 0.063 ppm of O3 (daily concentrations). Experiments done in animal models have shown that O3 induces acute lung injury, albeit at much high and long O3 exposures (near 2 ppm for 3-6 h). Our research has standardized a sensitive model of sterile murine lung inflammation by exposing mice for two hours at 0.05 ppm O3, a level below the current recommendations for what is considered a safe or "ambient" O3 concentration for humans (G. K. Aulakh et al., 2020a; Gurpreet K Aulakh et al., 2019; Brocos et al., 2019). 0.05 ppm O3 exposure causes immediate lung neutrophil recruitment, release of IL-1β dependent cytokines in broncho-alveolar lavage and bone marrow mobilization of pan-leukocyte chemokine, SDF1α (G. K. Aulakh et al., 2020a; Brocos et al., 2019). Thus, it is important to understand the progression of O3-induced early lung metabolic changes, at concentrations feasible in the environment.

[18F]F-FDG (2-deoxy-2-[$^{18}$F] fluoro-D-glucose) microPET/CT imaging is a sensitive method to detect lung cancer and study various inflammatory diseases. The current quantification methods focus on tracer kinetics and compartment modelling such as the Patlak and Sokoloff methods (D. L. Chen et al., 2009; Schroeder et al., 2008). However, the compartmental modelling does not convey the regional [18F]F-FDG activity pattern unless

images are acquired through dynamic gating protocols and invasive blood sampling. Many pre-clinical microPET scanners resolve only up to 80 μm structures, which cannot resolve functional activity in the murine alveolar septa. Thus, we sought to fast-track the imaging protocol without invasive blood sampling. For understanding disease progression and regional tracer localization in relation to specific organs such as lungs, we developed an imaging protocol cum image analysis strategy to quantify the sequential uptake and distribution of [18F]F-FDG in murine lungs. We imaged each animal at four separate imaging time-points spanning over 2 days.

The resulting CT attenuation grey values were plotted against the percent (%) lung [18F]F-FDG SUR (standard uptake ratio). These plots provide quantifiable spatio-temporal lung [18F]F-FDG distribution pattern. Our results indicate that O3 initially induces higher and heterogeneous lung [18F]F-FDG uptake, when analyzed by X-ray CT guided region of interest (ROI) analysis of the PET image slices.

## 3.3 MATERIALS AND METHODS

***3.3.1 Mice:*** The study was approved by the University of Saskatchewan's Animal Research Ethics Board (AUP 20170016) and adhered to the Canadian Council on Animal Care guidelines for humane animal use. Six-eight-week-old male C57BL/6J (Stock No. 000664) wild-type (WT) mice were procured from Jackson Labs (CA, US).

***3.3.2 O3 exposures:*** For O3 exposures, three WT mice were continuously exposed in an induction box for 2 h (Gurpreet K Aulakh et al., 2019; Brocos et al., 2019), during day-time to enable sequential imaging there-on. These mice were housed in custom induction box and had free access to food and water. O3 (0.05 ± 0.02 ppm) was generated, at 3 litres/minute, from

ultra-high-purity air using a silent-arc discharge O3 calibrator cum generator (2B Technologies, CO, USA). Constant chamber air temperature (72±3°F) and relative humidity (50 ± 15%) were maintained. O3 concentrations were calibrated in small box using a real-time O3 monitor (2B Technologies, CO, USA).

***3.3.3 Intranasal LPS exposures:*** For LPS exposures, three WT mice were lightly anesthetized with intraperitoneal (i.p.) ketamine (50 mg/kg)/xylazine (1 mg/kg) mix. A 50 µl aliquot of LPS (1 mg/ml) was filled into a sterile pipette tip. Thereafter, the mice were laid in supine position and the LPS solution was instilled into the external nares. The solution was instantaneously breathed in by the mice, soon after which the mice regained consciousness.

***3.3.4 Experiment design:*** Three pre-weighed mice were acclimatized to the cyclotron facility, overnight, and fasted for at least 4 hours before imaging. The experiment design is shown in the schematic (Fig. 1).

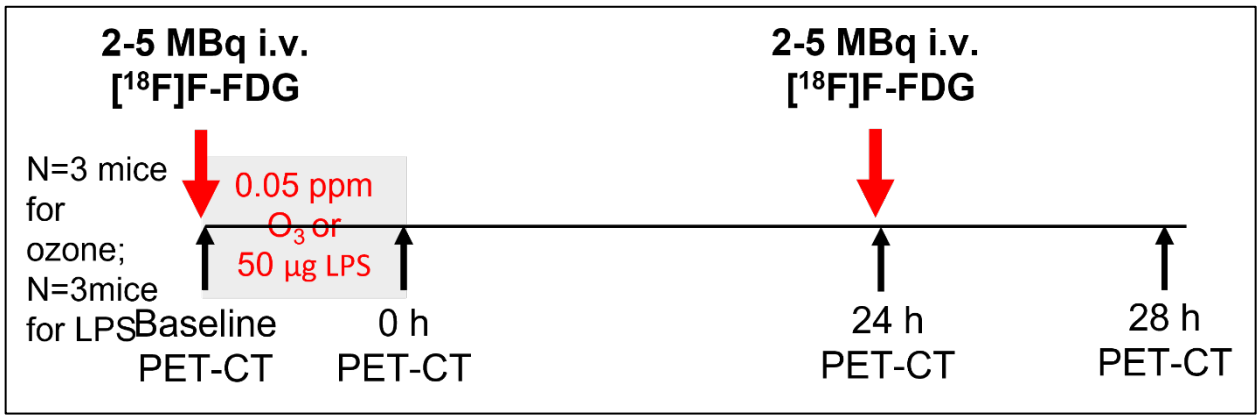


**Fig. 1: Experiment design and [18F]F-FDG PET-CT imaging protocol:** Three pre-weighed fasted wild-type (WT) C57BL/6J mice were injected intravenously (i.v.) with 2-5 MBq of [18F]F-FDG. Each mouse was then prepared for isoflurane anaesthesia and imaged. After baseline imaging, mice were exposed to either 0.05 ppm of ozone (O3) for 2 h or intranasal 50

μg of LPS. After exposure i.e., O3/LPS-0 h, the mouse was prepared for follow-up imaging of residual [18F]F-FDG activity. The mice were brought back to their cages and left in room-air. At 24 h after O3/LPS exposure, the mice were injected with another intravenous dose of 2-5 MBq of [18F]F-FDG and imaged (O3/LPS-24 h). After imaging, mice were returned to their cages. After 4 h, i.e., O3/LPS-28 h, the mice were imaged again for residual [18F]F-FDG activity.

Mice were imaged individually. At the beginning of the experiment, mice were prepared for baseline (i.e., before O3 or LPS exposure) imaging. Immediately after inducing isoflurane (5%) anesthesia, mice were maintained under 1.5-2.5% isoflurane on a warm water circulated heating pad and monitored for vital signs (*BioVet*, breathing rate 40-100 breaths per min, body temperature 36.5-38ºC and blood oxygen saturation by pulse oximetry i.e., $SpO_2$ 98-100%). Mice were injected with 2-5 MBq of [18F]F-FDG via a tail vein. Within 15-30 min post injection, mice were imaged at baseline, for 3-5 full-body time-frames (800 μm voxel size), where each frame spanned 5 min (*VECTor$^4$CT, MI Labs*), for over 25 minutes. [18F]F-FDG microPET imaging was followed by a 2-minute X-ray CT (2 bed positions). After baseline imaging, the mice were continuously exposed for 2 h at 0.05 ppm O3 or instilled with LPS as explained above. Immediately after O3 or LPS exposure (i.e., 0 h post-O3 or LPS exposure), the mice underwent similar full body microPET/CT imaging. The next day, at approximately 24 h after O3 or LPS exposure, the mice were again injected i.v. with 2-5 MBq of [18F]F-FDG and imaged for 3-5 full body [18F]F-FDG PET-CT scans. Roughly four hours later, i.e., at 28 h post-O3 or LPS exposure, mice were imaged for any residual [18F]F-FDG activity with similar full-body [18F]F-FDG scans.

***3.3.5 Image processing and analysis:*** The acquired X-ray and PET-CT image data sets were processed for flat and dark current normalization, reconstruction, co-registration (MI Labs software) and quantification by Pmod (pmod.com). As all the time-points, before and after O3 or LPS exposure, were acquired through the same imaging protocol, the [18F]F-FDG counts were decay corrected in order to plot tissue [18F]F-FDG uptake or elimination, and not decay, for the 30 minute imaging time. Thereafter, the images were quantified and analyzed on Image J (https://fiji.sc/#). The image stacks from X-ray CT were threshold-selected to segment out the lungs. Depending upon the data-set, anywhere from 130-160 ortho slices spanned the entire lung region. The selected regions of interest (ROIs) were then copied on to the corresponding [18F]F-FDG PET image slices across multiple frames (F0-F4). The ROIs, from X-ray CT as well as the PET images, were simultaneously quantified for the various image parameters such as the area, perimeter, mean, median, mode, standard deviation (SD), range and integrated counts. After exporting the data to excel file, data was sorted, filtered, and analyzed for corresponding imaging time-points, frames and/or CT parameters *(DOI: 10.6084/m9.figshare.12233576)*. Finally, a SUM of the full-body parameters of Z-stacks were analyzed for every frame in order to calculate the full body [18F]F-FDG SUV (Standard Uptake Value). After [18F]F-FDG SUV is quantified for lung slice(s) as well as the full-body, the ratio of these values is termed as the Standard Uptake Ratio (SUR). The lung CT grey values were plotted against "lung [18F]F-FDG SUR", which was overlaid for multiple frames on the same graph. These plots were then smoothened using the second polynomial function (Savitzky et al., 1964), in order to compute trends in lung [18F]F-FDG SUV or S.D. and subsequently, % increase in lung [18F]F-FDG post-O3 or LPS exposure. Please refer to Fig. 2 for flow-chart of the image processing. To investigate the [18F]F-FDG activity in other organs, such as the brain, heart (representing the circulating blood

pool) and urinary bladder (representing the excretory pool), we also plotted [18F]F-FDG time-activity curves in these organs over 30 minutes at baseline, 0, 24 and 28 h time-points.

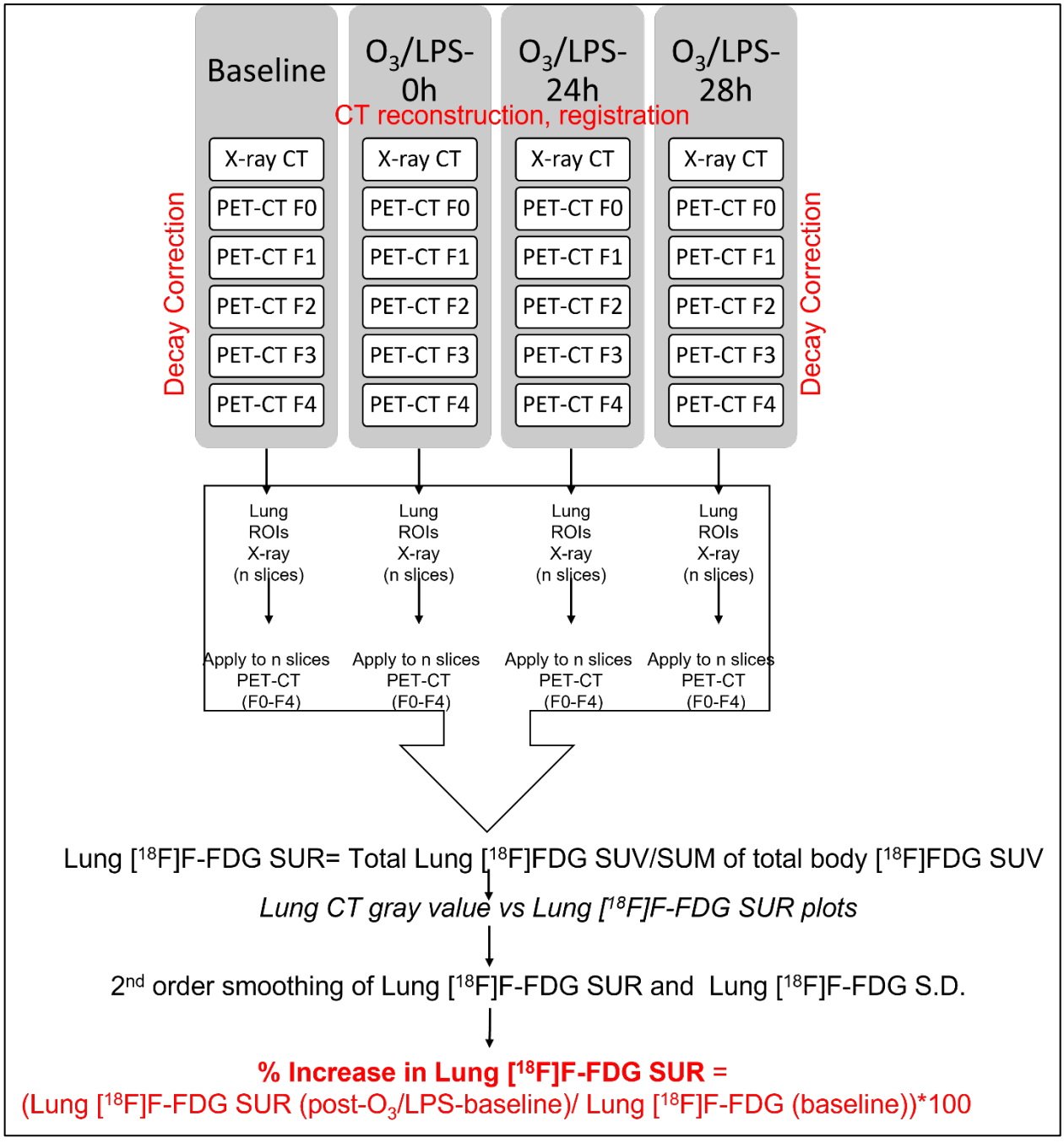


**Fig. 2: Image processing and analysis for sequential lung [18F]F-FDG SUR determination:** The acquired X-ray and PET-CT image data sets were processed for flat and dark current

normalization, reconstruction, co-registration (MI Labs software) and preliminary quantification by Pmod (***pmod.com***). As all the time-points, before and after O3/LPS exposure, were acquired through the same imaging protocol, the [18F]F-FDG counts were decay corrected in order to plot tissue [18F]F-FDG uptake or elimination, and not decay, for the 30-minute imaging time. Thereafter, the image sequences were quantified and analyzed on Image J (***https://fiji.sc/#***). The image stacks from X-ray CT were threshold-selected to segment out the lungs. The selected lung regions of interest (ROIs) were then copied on to the corresponding [18F]F-FDG PET image slices across multiple frames (F0-F4). The ROIs, from X-ray CT as well as the PET images, were simultaneously quantified for the various image parameters such as the area, perimeter, mean, median, mode, standard deviation (S.D.), range and integrated counts. After exporting the data to excel file (DOI: 10.6084/m9.figshare.12233576), data was sorted, filtered, and analyzed for corresponding mouse time-points, frames and/or CT parameters. Finally, a SUM of the same full-body parameters of Z-stacks were analyzed for every frame in order to calculate the [18F]F-FDG SUV. After [18F]F-FDG SUV is quantified for lung slice(s) as well as the full-body, the ratio of these values is termed as the Standard Uptake Ratio (SUR). The lung CT grey values were plotted against "lung [18F]F-FDG SUR" or "lung [18F]F-FDG S.D." which was overlaid for multiple frames on the same graph. These plots were then smoothened using the second polynomial function (Savitzky & Golay,1964), in order to compute trends in final lung [18F]F-FDG SUR or S.D. and subsequently, % increase in lung [18F]F-FDG post- O3/LPS exposure.

### 3.4 STATISTICAL ANALYSIS

Data are expressed as median with inter-quartile range of the respective parameter (% lung [18F]F-FDG SUR, lung [18F]F-FDG SD, lung CT grey values) and for testing the differences

for a given treatment at various time points (before or after exposure) were analyzed by one-way analysis of variance (ANOVA) (GraphPad Prism 9 software, LLC, CA, US).

## 3.5 RESULTS

### *3.5.1 O3 causes lung [18F]F-FDG retention immediately and up to 24 h after exposure:*

At baseline (i.e., within 15-30 min after [18F]F-FDG injection), 1.90-2.28% of [18F]F-FDG is extracted by lungs (Fig. 3, Movie 1) compared to the full-body uptake (Fig. 4a), with majority excreted through the urinary bladder (Fig. 9a, b, Suppl. Fig. 1a). Notice the steady uptake in bladder (up to 37 minutes of imaging) versus already peaked concentrations in lungs (by 17 minutes) and heart (by 24 minutes) (Supp. Figs. 1a, a1).

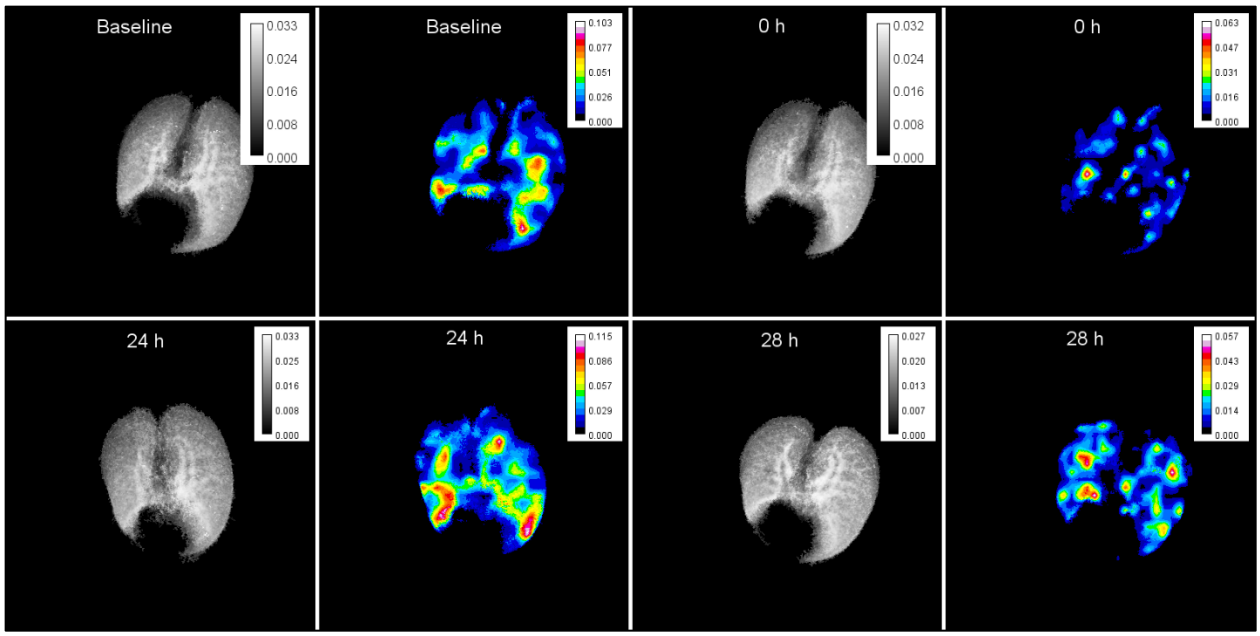


**Fig. 3: Sequential lung [18F]F-FDG distribution before and after acute 2 h 0.05 ppm ozone (O3) exposure using X-ray region-of-interest:** Representative lung X-ray CTs, displaying standard deviation of the CT pixels, sum of lung [18F]F-FDG activity normalized to16-color

scale shown for the first frame (F0) from a mouse at baseline (i.e., before any exposure), or at O3-0, 24 and 28 h time-point.

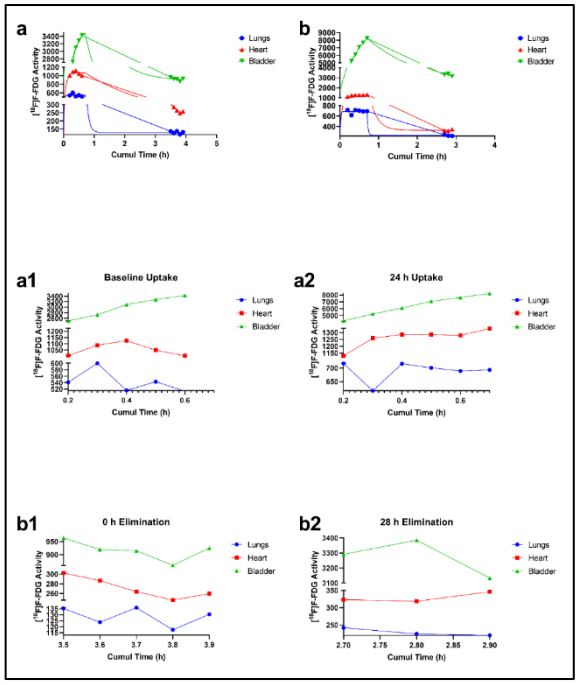


**Fig. 4:** [18F]F-FDG time activity curves for lungs (shown in blue), heart (shown in red) and urinary bladder (shown in green) on **a)** quantified for Day 1 (over 4 h), showing **a1)** initial [18F]F-FDG uptake phase at baseline and **a2)** [18F]F-FDG elimination phase at 0 h post O3 exposure time-points (spanning 0.6 h). Similar time activity curves are also shown for **b)** Day 2 (over 4 h), further showing **b1)** [18F]F-FDG uptake phase at 24 h and **b2)** [18F]F-FDG elimination phase at 28 h post O3 exposure time-points (spanning 0.6 h).

The physical half-life of [18F]F-FDG decay is 109.8 min and biological half-life of 16 min, which means that >50% of [18F]F-FDG was decayed by the 2$^{nd}$ imaging time, which is immediately after O3 exposure (at 0 h i.e., 2 h after baseline imaging). However, because we took account of full-body counts at every imaging time-point, regional lung [18F]F-FDG SUR was expressed as a percent (%) normalized lung [18F]F-FDG, which is irrespective of the time of imaging. Lung [18F]F-FDG SUR (units) varied from 0.019 to 0.0228, at baseline. The % regional lung [18F]F-FDG SUR varied from 7.42 X $10^{-5}$ to 0.043%, at baseline. Immediately after O3 exposure (O3-0 h), mid-level lung slice shows large alveolar regions devoid of [18F]F-FDG uptake (Fig. 3). The [18F]F-FDG SUV (units) varied from 0.0147 to 0.0164, at 0 h. The % regional lung [18F]F-FDG SUR varied from 7.42 X $10^{-6}$ to 0.032, at 0 h. At 0 h, the [18F]F-FDG

elimination kinetics is slowed in the lungs, compared to the heart and bladder (Figs. 4a, a2). The [18F]F-FDG signal has a lower background signal at this time-point owing to significant renal clearance of [18F]F-FDG.

It must be noted that O3 induces instant lung tissue damage, as indicated by attenuated lung CT grey values, at 0 and 24 h post-exposure, compared to baseline values (Fig. 5j). Despite the loss of lung tissue, O3 induced a 72.21±0.79% increase ($p<0.05$) in lung [18F]F-FDG at 0 h compared to baseline (Figs. 5a, b, e, f, i). This is not very obvious in the single ortho-slice shown but evident in the volume rendered [18F]F-FDG uptake in lungs shown in Fig. 3 and Movie 2. Upon re-administration of [18F]F-FDG at 24 h post O3 exposure, all three organs continued to accumulate the [18F]F-FDG compared to the elimination phase observed in lungs and heart at baseline (Figs. 4b, b1). The [18F]F-FDG SUV (units) varied from 0.0123 to 0.0166, at 24 h. The % regional lung [18F]F-FDG SUR varied from $1.51 \times 10^{-4}$ to 0.032, at 24 h. At 24 h post-O3 exposure, [18F]F-FDG was 42.54±0.33% higher ($p<0.01$) compared to baseline (Figs. 3, 5c, g, Movie 3). There were multiple areas of high concentration near the higher attenuating lung regions. The [18F]F-FDG SUV (units) varied from 0.0158 to 0.0183, at 28 h. The % regional lung [18F]F-FDG SUR varied from $3.64 \times 10^{-5}$ to 0.041, at 28 h. Thus, at 28 h post-O3 exposure, there wasn't a significant change ($p>0.05$) in lung [18F]F-FDG compared to baseline (Figs. 3, 5d, h, Movie 4), but the pattern of [$^{18}$F] [18F]F-FDG uptake shifted towards the lower attenuating lung regions. The lung CT grey values also showed higher values, indicating inflammatory influx, at 28 h post-O3 exposure compared to baseline i.e., before any exposure.

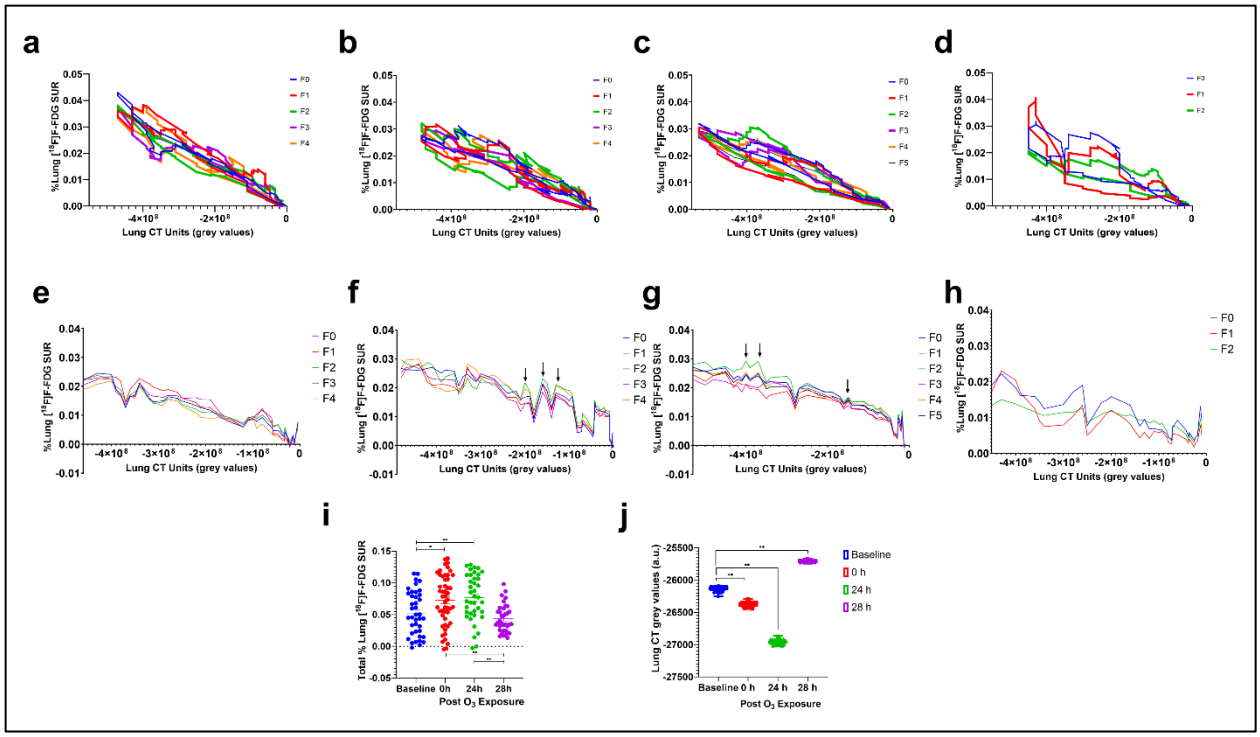


**Fig. 5: Quantification of lung [$^{18}$F]F-[18F]F-FDG Standard Uptake Ratio (SUR) and CT parameters:** Representative SUR data from a mouse quantified for each 5 minute imaging time-frame a-d) Percent (%) lung [$^{18}$F]F-[18F]F-FDG SUR plotted against corresponding lung X-ray CT units (in arbitrary grey values), e-h) Smoothened % lung [$^{18}$F]F-[18F]F-FDG SUR plotted against the lung X-ray CT units (grey values), i) Three imaging time-frames were then pooled to plot the % Lung [$^{18}$F]F-[18F]F-FDG at baseline, as well as 0, 24 and 28 h post-O3 exposure. j) regional lungs mean, upper and lower range CT grey (arbitrary) values shown at baseline, as well as 0, 24 and 28 h post-O3 exposure. For graphs i) and j), baseline data is shown in blue, O3-0 h in red, O3-24 h in green and O3-28 h in purple scatter plots. Data from figures I and J were analysed by one-way ANOVA, * represents significance at $p<0.05$ and ** at $p<0.01$.

The regional lung [18F]F-FDG distribution standard deviation (S.D.) values indicate the variation in [18F]F-FDG uptake across the analysed lung regions i.e., low vs high grey value regions. At baseline, the [18F]F-FDG S.D. ranged from 0.000153 to 0.000958 (Fig. 6a).

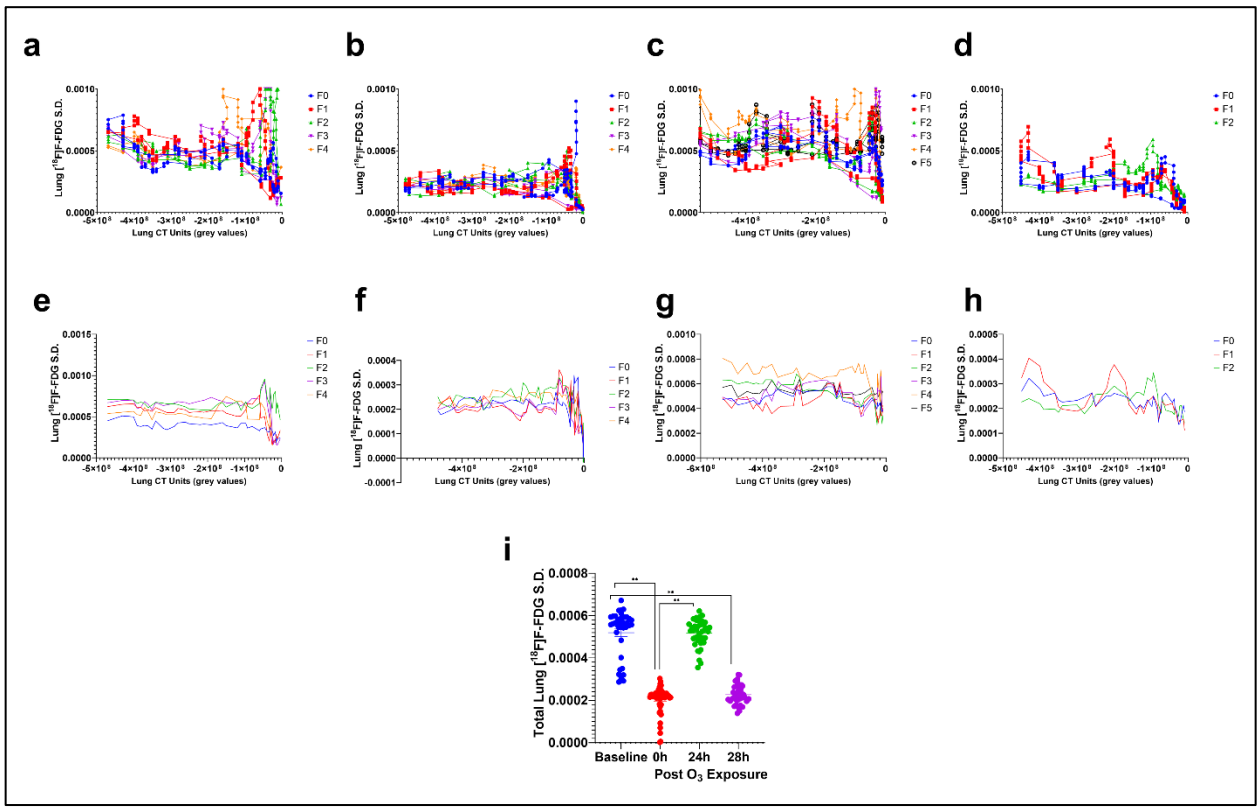


**Fig. 6: Quantification of lung [18F]F-FDG Standard Deviation (S.D.) parameters:** Representative S.D. data from a mouse quantified for each 5-minute imaging time-frame a-d) Percent (%) lung [18F]F-FDG S.D. plotted against corresponding lung X-ray CT units (in arbitrary grey values), e-h) Smoothened % lung [18F]F-FDG S.D. plotted against the lung X-ray CT units (grey values). Please note that F0 is shown in blue, F1 in red, F2 in green, F3 in purple and F4 is shown in orange data points and line plots. i) Three image time-frames were then pooled to plot the Total Lung [18F]F-FDG S.D. at baseline, as well as 0, 24 and 28 h post-O3 exposure. For graph i), baseline data is shown in blue, O3-0 h in red, O3-24 h in green and O3-28 h in purple scatter plots. Data from figure I was analysed by one-way ANOVA, * represents significance at $p<0.05$ and ** at $p<0.01$.

We initially observed an attenuation in the lung [18F]F-FDG S.D. (1.78 X $10^{-5}$ to 3.62 X $10^{-5}$) at 0 h ($p<0.01$) (Fig. 6a, b, e, f, i) but at 24 h, we observed a heterogeneous distribution (higher [18F]F-FDG S.D. ranging from 2.65 X $10^{-4}$ to 8.07 X $10^{-4}$, $p<0.01$) when compared to baseline (Figs. 3, 6a, c, e, g, i). The lower S.D. at 0 and 28 h post O3 exposures (i.e., almost 3 h after respective [18F]F-FDG injections on 1st and 2nd day) are very likely due to clearance of [18F]F-FDG resulting in lower background activity. At 28 h post O3 exposure, lung [18F]F-FDG S.D. distribution was not significantly high (ranging from 1.12 X $10^{-4}$ to 4.04 X $10^{-4}$, $p>0.05$), when compared to the baseline S.D. (Figs. 3, 6a, d, e, h, i). However, there were specific areas of high [18F]F-FDG uptake (Fig. 3). At 28 h post O3 exposure, lungs but not the heart, cleared a significant proportion of [18F]F-FDG, as observed in the time-activity curve (Figs. 4b, b2) as well as the 3-d rendered views (Fig. 3 and Movie 4).

### *3.5.2 LPS causes lung [18F]F-FDG retention up to 28 h after exposure:*

Regional lung maps of total [18F]F-FDG activity showed characteristic high cranio-caudal gradient at baseline (Fig. 7).

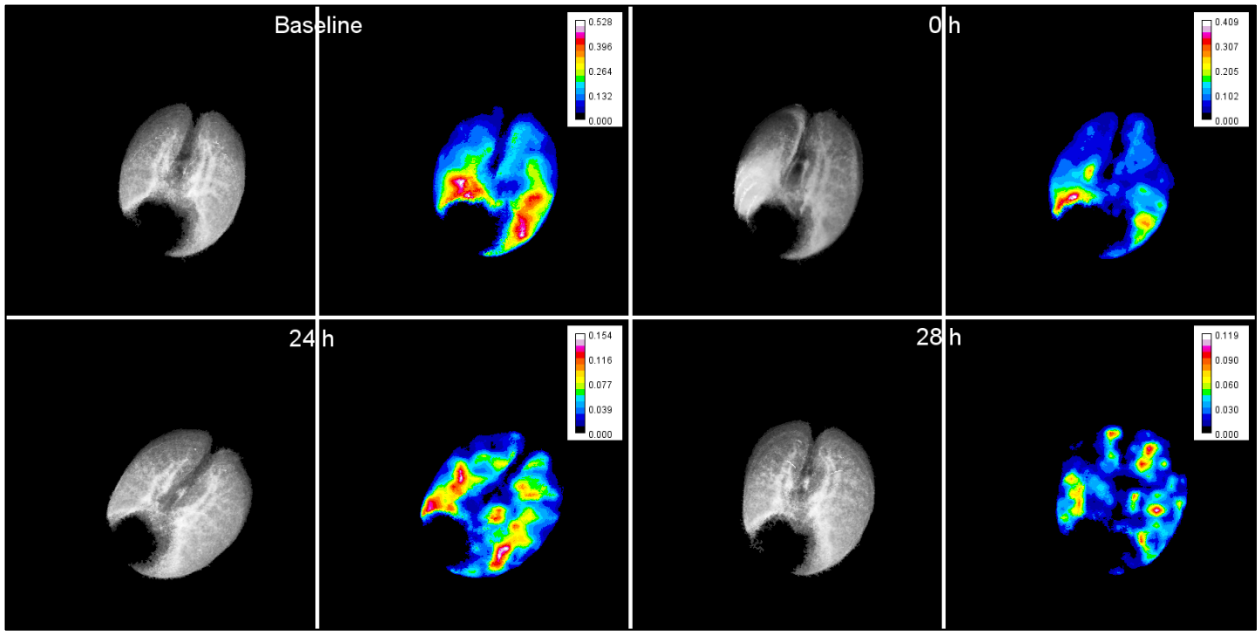

**Fig. 7: Sequential lung [18F]F-FDG distribution before and after intranasal LPS (50 µg) exposure using X-ray region-of-interest:** Representative lung X-ray CTs, displaying standard deviation of the CT pixels, sum of lung [18F]F-FDG activity normalized to16-color scale shown for the first frame (F0) from a mouse at baseline (i.e., before any exposure), or at LPS-0, 24 and 28 h time-point.

Lung [18F]F-FDG SUR (units) varied from 0.013 to 0.017 at baseline. The F0: S.D = $4.05X10^{-5}$ to 0.001 and SUR = $7.15X10^{-7}$ to 0.00037, F1: S.D = $3.74X10^{-5}$ to 0.001 and SUR = $6.50X10^{-7}$ to 0.00036, F2: S.D = $2.31X10^{-5}$ to 0.0009 and SUR = $1.96X10^{-7}$ to 0.00044 (Fig. 8a, e, Fig. 9a, e). The % regional lung [18F]F-FDG SUR varied from 1.30 to 1.70 % at baseline. Immediately after LPS exposure (LPS-0 h), mid-level lung slice shows heterogenous alveolar regions with [18F]F-FDG uptake (Fig. 7). The [18F]F-FDG SUR (units) varied from 0.0099 to 0.0224 at 0 h. After LPS exposure, at 0 h the F0: S.D = $2.75X10^{-5}$ to 0.0006 and SUR = $1.20X10^{-6}$ to 0.00034, F1: S.D = $1.18X10^{-6}$ to 0.001and SUR = $4.53X10^{-8}$ to 0.00038, F2: S.D = $2.61X10^{-5}$ to 0.00079 and SUR = $8.82X10^{-7}$ to 0.00041 (Fig. 8b, f, Fig. 9b, f).

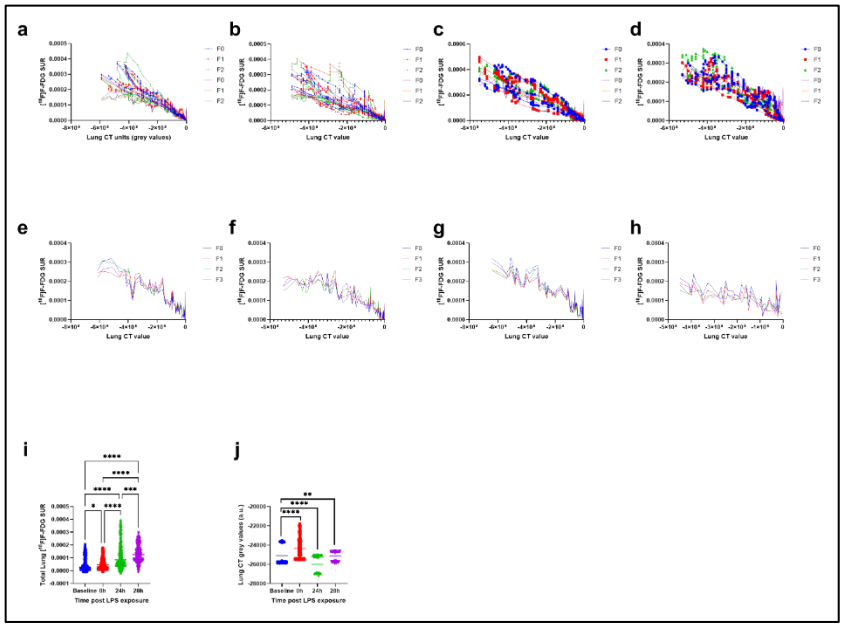


**Fig. 8: Quantification of lung [18F]F-FDG Standard Uptake Ratio (SUR) and CT parameters:** Representative SUR data from a mouse quantified for each 5 minute imaging time-frame a-d) Percent (%) lung [18F]F-FDG SUR plotted

against corresponding lung X-ray CT units (in arbitrary grey values), e-h) Smoothened % lung [18F]F-FDG SUR plotted against the lung X-ray CT units (grey values), i) Three imaging time-frames were then pooled to plot the % Lung [18F]F-FDG at baseline, as well as 0, 24 and 28 h post-LPS exposure. j) regional lungs mean, upper and lower range CT grey (arbitrary) values shown at baseline, as well as 0, 24 and 28 h post-LPS exposure. For graphs i) and j), baseline data is shown in blue, LPS-0 h in red, LPS-24 h in green and LPS-28 h in purple scatter plots. Data from figures I and J were analysed by one-way ANOVA, * represents significance at $p<0.05$ and ** at $p<0.01$.

The % regional lung [18F]F-FDG SUR varied from 0.99 to 2.24 at 0 h. After LPS exposure at 24 h, the F0: S.D = $2.92X10^{-5}$ to 0.00069 and SUR = $7.72X10^{-7}$ to 0.00044, F1: S.D = $1.18X10^{-5}$ to 0.00067 and SUR = $8.24X10^{-7}$ to 0.0005, F2: S.D = $7.54X10^{-7}$ to 0.00083 and SUR = $1.97X10^{-8}$ to 0.00044 (Fig. 7c, g, Fig. 8c, g). The % regional lung [18F]F-FDG SUR varied from 1.69 to 2.49 at 24 h, which is 61% higher when compared to baseline [18F]F-FDG SUR. After LPS exposure at 28 h, the F0 S.D = $4.07X10^{-6}$ to 0.0007 and SUR = $1.57X10^{-7}$ to 0.00034, F1: S.D = $3.32X10^{-5}$ to 0.001 and SUR = $1.60X10^{-6}$ to 0.00032, F2: S.D = $9.13X10^{-7}$ to 0.00081 and SUR = $2.23X10^{-8}$ to 0.00038 (Fig. 7d, h, Fig. 8d, h). The % regional lung [18F]F-FDG SUR varied from 1.54 to 2.01 at 28 hr, which is 56.6% compared to baseline. The cranio-caudal gradient of lung [18F]F-FDG was lost at 24 and 28 h post-LPS exposure (Fig. 6). Non-parametric comparisons between different time-points in lungs revealed that the total lung [18F]F-FDG was significantly lower at 0 h ($p=0.015$), but higher at 24 ($p<0.0001$) and 28 h ($p<0.0001$) post LPS exposure when compared to baseline values (Fig. 7i). The variation, as measured by the standard deviation, in [18F]F-FDG uptake in lungs was significantly low at 0 ($p<0.0001$), 24 ($p<0.0001$) and 28 h ($p<0.0001$) post-LPS exposure when compared to baseline (Fig. 8i).

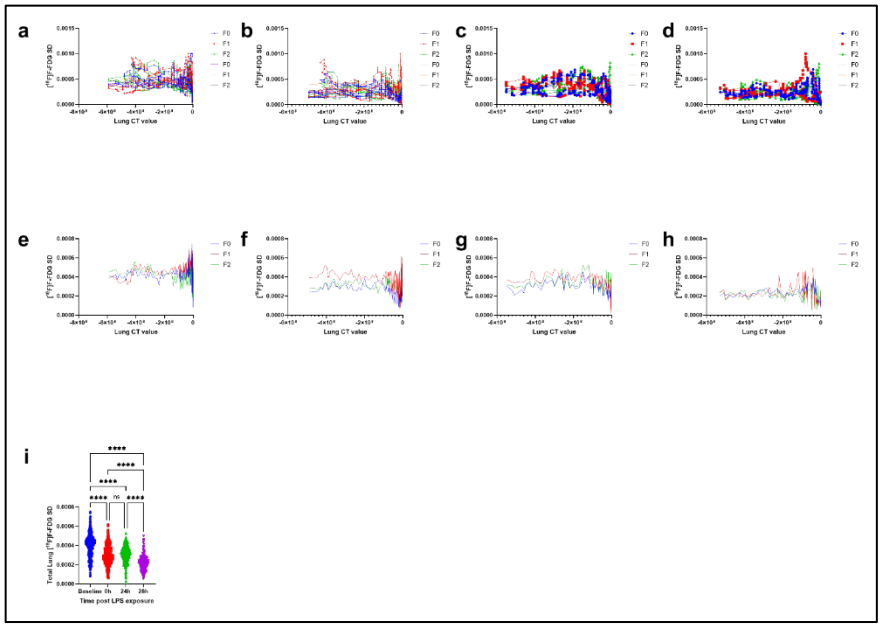


**Fig. 9: Quantification of lung [18F]F-FDG Standard Deviation (S.D.) parameters:** Representative S.D. data from a mouse quantified for each 5-minute imaging time-frame a-d) Percent (%) lung [18F]F-FDG S.D. plotted against corresponding lung X-ray CT units (in arbitrary grey values), e-h) Smoothened % lung [18F]F-FDG S.D. plotted against the lung X-ray CT units (grey values). Please note that F0 is shown in blue, F1 in red, F2 in green, F3 in purple and F4 is shown in orange data points and line plots. i) Three image timeframes were then pooled to plot the Lung [18F]F-FDG S.D. at baseline, as well as 0, 24 and 28 h post-LPS exposure. For graph i), baseline data is shown in blue, LPS-0 h in red, LPS-24 h in green and LPS-28 h in purple scatter plots. Data from figure I was analysed by one-way ANOVA, * represents significance at $p<0.05$ and ** at $p<0.01$.

Time activity curves revealed that LPS exposure causes a higher retention of [18F]F-FDG in lungs especially at 20 h which is more than, that observed in the heart (Fig 10d). Note that the urinary bladder showed highest activity at 24 h, followed by cranium (i.e. brain), lungs and then heart (Fig. 10c). At 28 h, cranium showed higher [18F]F-FDG activity followed by urinary bladder, lungs, and the heart (Fig. 10d).

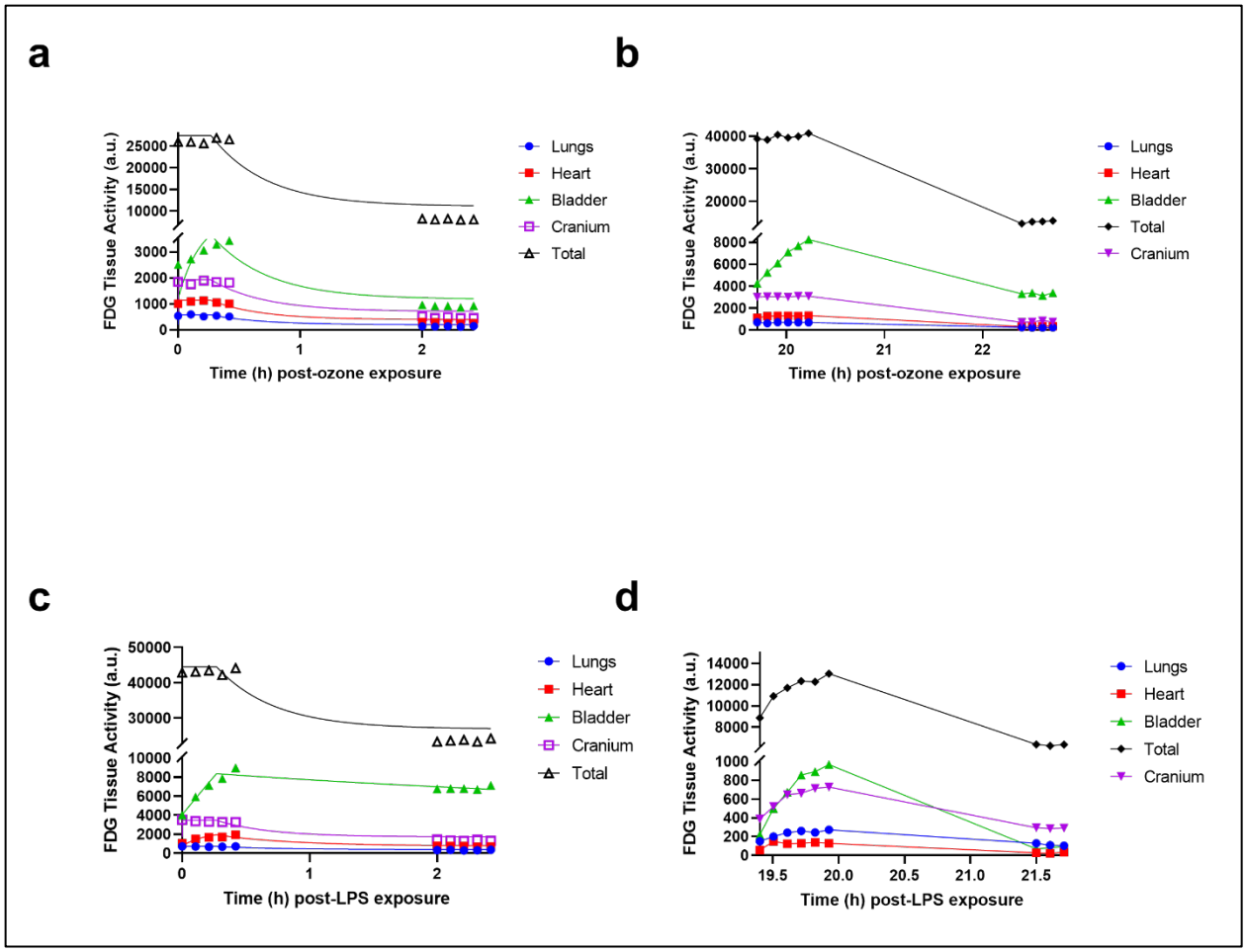


**Fig. 10: [$^{18}$F]F-[18F]F-FDG time activity curves** for lungs (shown in blue), heart (shown in red) and urinary bladder (shown in green), cranium (shown in purple) and the total body activity (shown in black) **a)** quantified for Day 1 (over 2 h), showing initial [$^{18}$F]F-[18F]F-FDG uptake phase at baseline and the [$^{18}$F]F-[18F]F-FDG elimination phase at 0 h post O3 exposure time-points (spanning 0.6 h) **b)** and then for Day 2 (over 4 h), further showing [$^{18}$F]F-[18F]F-FDG uptake phase at 20 h and [$^{18}$F]F-[18F]F-FDG elimination phase at 23 h post O3 exposure time-points (spanning 0.6 h). Similar time activity curves are also shown for **c)** Day 1 baseline i.e., before LPS exposure and the [18F]F-FDG elimination phase at 0 h (i.e., immediately) post LPS exposure time-points (spanning 0.6 h) **d)** Day 2 (over 4 h), further showing [18F]F-FDG uptake

phase at 19.5 h and [18F]F-FDG elimination phase at 21.5 h post LPS exposure time-points (spanning 0.6 h).

The lung CT grey values were significantly different amongst the different groups before or after LPS exposure with 0 h showing the highest CT value ($p<0.0001$), followed by 28 h ($p=0.0084$) when compared to baseline, i.e., before any exposure (Fig. 8j). The 24 h time point had the lowest CT values when compared to baseline ($p<0.0001$), 0 ($p<0.0001$) or 28 h ($p<0.0001$) time points (Fig. 8j).

### *3.5.3 Lung volume does not change significantly after LPS or O3 exposure:*

Lung attenuation values were thresholded to segment out the lungs and then calculate the total lung volume. The low and high attenuation values within the already segmented lungs were further thresholded and binarized to compute the percentage of lung volume occupied by tissue or fluids. For the group consisting of O3 exposed mice, the mean lung volume before exposure, i.e., at baseline, was 283.57±18.02 $mm^3$, immediately after exposure i.e., at 0 h, was 239.57±21.79 $mm^3$, at 24 h after exposure, was 232.21±17.65 $mm^3$ and at 28 h after exposure the lung volume was back up to 239.08±12.30 $mm^3$ (Fig. 10a).

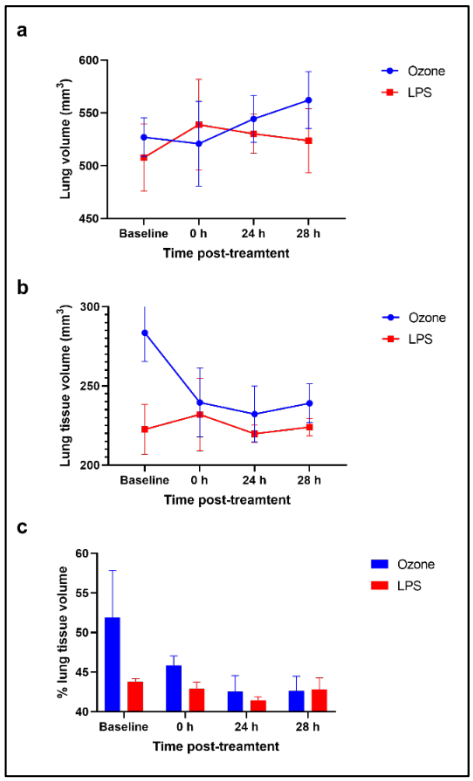


**Fig. 11: X-ray CT grey values guided lung pixel thresholding, segmentation, and quantification** of a) total lung volume (mm3), b) lung tissue/fluid volume (mm3) and c) percentage (%) of the lung tissue/fluid volume at baseline (i.e., before) and at 0 h (i.e.,

immediately), 24 and 28 h after 2 h of 0.05 ppm O3 (shown in blue bar graphs) and intranasal 50 μg LPS (shown in red bar graphs) exposure. Note that the X-ray CT thresholding was not able to segment out the tissue from fluid due to lack of resolution of the imager. Thus, we observe trends and not significant differences over various time points.

There wasn't any significant change in the total lung volume following the acute low-dose O3 exposures. The percentage of lung volume occupied by tissue or fluids was next determined by applying a narrower threshold. For the group consisting of O3 exposed mice, the mean percent (%) lung volume occupied by tissue or fluids before O3 exposure, i.e., at baseline, was 51.92±5.92%, immediately after exposure i.e., at 0 h, was 45.87±1.18%, at 24 h after exposure, was 42.52±2.06% and at 28 h after exposure the lung volume was back up to 42.63±1.86% (Fig. 11b, c). Thus, there wasn't any significant change in the percentage of lung volume occupied by tissues or fluids, following the acute low-dose O3 exposures.

For the group consisting of LPS exposed mice, the mean lung volume before LPS exposure, i.e., at baseline, was 222.56±15.76 $mm^3$, immediately after exposure i.e., at 0 h, was 232.00±22.86 $mm^3$, at 24 h after exposure, was 219.77±5.51 $mm^3$ and at 28 h after exposure the lung volume was back up to 223.93±5.48 $mm^3$ (Fig. 11a). There wasn't any significant change in the total lung volume following the acute LPS exposures.

The mean percent lung volume occupied by tissue or fluids, before LPS exposure, i.e., at baseline, was 43.80±0.39%, immediately after exposure i.e., at 0 h, was 42.93±0.82%, at 24 h after exposure, was 41.47±0.42% and at 28 h after exposure the lung volume was back up to 42.85±1.43% (Fig. 11b, c). Thus, there wasn't any significant change in the percentage of lung volume occupied by tissues or fluids, following the acute LPS exposures.

## 3.6 DISCUSSION

Positron emission tomographic (PET) imaging with [18F]F-FDG is a promising technique that may serve as a more sensitive outcome measure for pulmonary inflammation. The advantages of PET imaging include its noninvasiveness, ease of quantification, and ability to assess the entire lung. [18F]F-FDG-PET exploits the "Warburg effect", the observation that many cancers use aerobic cytoplasmic glycolysis as opposed to mitochondrial glucose oxidation as a major energy source, a process that requires increased cellular glucose uptake. Aerobic glycolysis is also a characteristic of nonmalignant proliferating cells and is observed in acute lung inflammation (Ostroukhova et al., 2012; Srivastava et al., 2015). Evidence to date suggests that neutrophils contribute primarily to the increased uptake of [$^{18}$F]F-[18F]F-FDG in lung inflammation and that the [$^{18}$F]F-[18F]F-FDG-PET signal correlates with the presence of activated neutrophils (Rodrigues et al., 2017). Clinical studies have also demonstrated that [$^{18}$F]F-[18F]F-FDG-PET imaging can be used to assess the neutrophilic inflammatory burden in the lungs in cystic fibrosis, pneumonia, and experimentally induced lung inflammation (D. L. Chen et al., 2006; Harris et al., 2011; Rodrigues et al., 2017; Vanfleteren et al., 2014). These results together indicate that [18F]F-FDG-PET imaging can potentially be used to measure changes in pulmonary inflammation in response to anti-inflammatory treatments.

We set out to explore 2 questions: (1) the utility of dynamic [18F]F-FDG-PET acquisition in discriminating before and after O3 exposure; (2) the feasibility of [18F]F-FDG-PET in tracking the pathology of O3 induced lung inflammation in in vivo O3 models and their response over time (0, 24 and 28 h). Recently, (Hofheinz et al., 2016) have shown that tumor to blood SUR, and not SUV, correlate with Patlak based $K_m$ i.e., metabolic [18F]F-FDG uptake in tumors, when imaged at dual-time points (Hofheinz et al., 2016). Along similar lines, we

performed two dual-time point imaging on the same animal to create lung [18F]F-FDG SUR maps, which allows longitudinal characterization of lung inflammation. Our data demonstrate time-dependent variability in [18F]F-FDG uptake in O3 exposed lungs. Dual-time [$^{18}$F]F-[18F]F-FDG imaging has been done in the past to evaluate pulmonary fibrosis (Umeda et al., 2015) and idiopathic interstitial pneumonia (Umeda et al., 2009), where positive lung [$^{18}$F]F-[18F]F-FDG retention is predictive of earlier deterioration of pulmonary function and mortality. However, these studies quantified [18F]F-FDG in a few 2-5 ROIs in lungs, whereas our study evaluates whole lung [18F]F-FDG distribution and provides both fractional as well as total lung [18F]F-FDG distribution over time.

While [18F]F-FDG uptake in normal lungs is quite low, there is regional variability in lung [18F]F-FDG distribution. Our data shows that at baseline, i.e., before O3 or LPS exposure, [18F]F-FDG showed ventro-dorsal (with dorsal portions showing higher values) and craniocaudal gradients (with caudal regions showing higher values), which has been reported in earlier studies. These patterns observed are partly due to the mouse positioning during imaging. Despite of the position of the mouse, we observed a differential pattern of lung [18F]F-FDG distribution immediately after O3 exposure. [18F]F-FDG transported from the blood to tissues by a carrier-mediated diffusion mechanism. Hexokinase catalyzes the phosphorylation of [18F]F-FDG to [18F]F-FDG -6-phosphate, which is metabolically trapped in the tissues. Blood [18F]F-FDG activity is generally low. Tissue [18F]F-FDG uptake is dependent upon blood flow, glucose metabolism and tissue density. Thus, the [18F]F-FDG gradients observed in lungs are also multifactorial. There is a predominant [18F]F-FDG uptake observed in the myocardium, and the liver. Scatter from these organs might contribute to the increased [18F]F-FDG uptake in the

lower lungs (Miyauchi and Wahl, 1996). Regional differences in lung [18F]F-FDG uptake, while modest, are significant and should be considered while interpreting PET studies.

The immediate (0 h) increase in O3-induced lung [18F]F-FDG was detectable as multiple spikes in the regions with lowest CT attenuation number near cranial and caudal regions. The increase in lung [18F]F-FDG uptake was observed despite O3 induced lung damage, as indicated by lowered CT values, at 0 and 24 h post O3 exposure. Some ortho-slices showed large gaps in [18F]F-FDG distribution, which also indicate the immediate alveolar damage by O3. Thus, the strength of our systematic regional as well as gross lung [18F]F-FDG analysis lies in the fact that our analysis could detect O3-induced metabolic activation of different alveolar regions, as a result of inflammation, despite alveolar damage. At 24 h after O3 exposure, the opposite pattern was observed i.e., the [18F]F-FDG spikes were smaller and observed in the high attenuation regions or the mid-lung regions. At 28 h after O3 exposure, there was an overall reduction in the lung [18F]F-FDG uptake. However, the distribution pattern was homogenous, indicating that the pulmonary circulation homogenously extracts [18F]F-FDG.

LPS induced predictable [18F]F-FDG distribution patterns by accumulating in lungs up to 28 h after exposure.

We did not report the uptake or elimination [18F]F-FDG rate constants in our current study, owing to fewer data points, spanning a total of 30-35 minutes imaging in 5-minute increments, which adds to the lack of time resolution for effective uptake and elimination rate constant calculations. Future studies will aim at modifying the acquisition parameters for plotting [18F]F-FDG time activity curves and repeated blood sampling. Our sequential [18F]F-FDG imaging strategy is capable of objective analysis of the lung [$^{18}$F]F-[18F]F-FDG retention before as well as up to 28 h after O3 exposure.

## 3.7 CONCLUSION

Thus, our study reveals that longitudinal [18F]F-FDG-PET imaging may offer a tool for deep phenotyping of lung inflammation to understand the response to new targeted treatments in animal models and later in clinical trials. Acute low-dose O3 induced lung inflammation is detected as a transient increase in lung [18F]F-FDG activity in sparse pockets leading to a variable distribution compared to baseline [18F]F-FDG distribution. Intranasal LPS exposure, on the other hand, induced a relatively prolonged increase in lung [18F]F-FDG activity which was detectable up to 28 h, which was the time-point followed-up after exposure. However, the cranio-caudal and ventro-dorsal [18F]F-FDG gradients, observed at baseline, were abolished after respective exposures. The baseline gradients are partly due to the position in which the mouse was imaged in the scanner resulting in re-distribution of the blood in lungs, owing to gravity.

## 3.8 TRANSITION

The microPET-CT imaging of the two models provided us with a picture into the very early events i.e. up to 28 h, which are neutrophil dominated and thus reflected by lung [18F]F-FDG uptake. In order to look into the dynamics of acute inflammatory structural alterations in the lung air-tissue boundaries of mice modelled by the same inducers, the second thesis manuscript provides the details of the non-invasive synchrotron multiple image x-radiography (MIR) study conducted at the Canadian Light Source (CLS) in the University of Saskatchewan.

**(THESIS MANUSCRIPT 2)**

## CHAPTER 4

# Longitudinal Multiple Image X-Radiography of Mouse Lungs Exposed to Saline, Bacterial Lipopolysaccharide or Low-dose Acute Exposure to Ozone

**Authors:** Manpreet Kaur[1], Upkardeep Pandher[2], Vanessa Brown[1], Adam Webb[3], Arash Panahifar[3], Shelley Kirychuk[2], Dean Chapman[2], Gurpreet Kaur Aulakh[1]

**Affiliations:** [1]Western College of Veterinary Medicine, University of Saskatchewan, Saskatoon, Canada. [2]College of Medicine, University of Saskatchewan, Saskatoon, Canada. [3]Biomedical Imaging and Therapy Beamline, Canadian Light Source, Saskatoon.
Canada. *Email: gurpreet.aulakh@usask.ca

**Author contributions:** Manpreet Kaur (70%), Adam Webb, Arash Panahifar and Gurpreet Aulakh designed the study and the imaging protocol. Manpreet Kaur, Upkardeep Pandher, Vanessa Brown, Gurpreet Aulakh executed the experiments. Manpreet Kaur (35%), Shelley Kirychuk, Dean Chapman, Gurpreet Aulakh analyzed the results and wrote the manuscript. All the authors have read and edited the manuscript.

**Status:** The data from this thesis manuscript will be combined with more synchrotron and biochemical data collected by the lab, and thus incorporated into a larger manuscript.

## 4.1 **ABSTRACT**

The outcome of lung inflammation is important to host survival as lungs are necessary for oxygen exchange and fighting pathogens or any injurious stimuli. Thus, tracking the kinetics of lung inflammation is an important technological area of imaging research and development. The biomedical beamline at the Canadian Light Source is home to a novel multiple image radiography (MIR) set-up that allows measurement of the projected X-ray optical properties namely absorption, refraction and of most interest to us, ultra-small-angle x-ray scattering (USAXS), which has been hypothesized to reflect the number of lung air-tissue boundaries. Our current study aimed at following mice lungs before, immediately i.e., at 0 h, and thereafter at 24, 48 or 70 h after saline, bacterial lipopolysaccharide (LPS, 50 μg), or low dose (0.05 ppm for 2 h) ozone exposure. Our results indicate that the lung USAXS and refraction reduces, with a corresponding increase in absorption upon exposure to LPS or ozone and is detectable up to 70 h time-period which was followed in the current study. The results from this study reflect the inter-dependence of the X-ray optical properties as the build-up of fluid in the inflamed lungs, as observed in LPS or ozone group, contribute increases in absorption but reduction in refraction and USAXS.

## 4.2 **INTRODUCTION**

Traditional X-ray imaging methods are based solely on absorption of X-rays. The high attenuation coefficient of bones compared to the surrounding tissue offers a reasonable contrast to visualize bones and certain soft tissues, but low lung attenuation precludes reasonable tissue structure contrast in the lungs (Chapman et al., 1998; Zhong et al., 2000). Several phase-based X-ray imaging systems are under development for clinical as well as pre-clinical use e.g., in-line phase contrast imaging, analyzer-based or diffraction enhanced imaging and grating

interferometry imaging (Snigirev et al., 1995; Umkehrer et al., 2020; Wysokinski et al., 2016). These phase contrast methods make use of the shift in the X-ray phase because of changes in thickness and refractive indices of features in the objects being imaged. Multiple image radiography is a variant of the commonly known technique, DEI i.e. diffraction enhanced imaging that offers spatial resolution of three separate properties of X-rays interacting with matter, namely amplitude, refraction, and ultra-small angle scattering (USAXS) or width(G. K. Aulakh et al., 2018). Of particular interest in the lungs, the number of air-tissue boundaries in alveoli are directly proportional to the MIR width (Zhong et al., 2000). Thus, it is of interest to understand the X-ray optical properties in animal models of lung injury.

In an earlier study, we studied the X-ray optical properties in bacterial lipopolysaccharide (LPS) induced murine lung injury, albeit only up to 9 h post exposure (G. K. Aulakh et al., 2018). Contrary to our belief, the lung scatter and attenuation contrast ratios were higher at 9 h post LPS treatment. These results highlight the fact that acute lung injury induces an early increase in the number of air-tissue boundaries as a collective physiological response to injury and the accompanying vasodilatation and expansion of the alveolar septa. The MIR findings were supported by the accompanying measurement of air-tissue interfaces in DEI-CT from the healthy and LPS exposed lungs. Therefore, in the present study, we utilized two separate models of acute lung injury namely ozone (O3) induced and bacterial LPS induced lung inflammation, and control group comprising exposure to saline and followed the mice over 70 h to observe changes in the X-ray optical properties.

## 4.3 **MATERIALS AND METHODS**

The animal experiments conducted in this study were approved by the institutional animal care ethics committee. The beamline experimental protocol was approved by

the Canadian Light Source' proposal committee. Young male C57BL/6J mice, around six-eight-week-old, were procured from the Jackson Laboratories (CA, US). E. coli 0127: B8 lipopolysaccharide (LPS) was obtained from a commercial source (Sigma Chemicals, St. Louis, MO, US).

### *4.3.1* ***Synchrotron Multiple Image X-Radiography (MIR) imaging set-up***

Mice were imaged at the Biomedical Imaging and Therapy Bending Magnet (BMIT-BM) beamline of the Canadian Light Source located at the University of Saskatchewan, Canada. All objects were positioned in hutch POE-2 of the BMIT beamline, approximately 24 m downstream of the synchrotron source. The horizontal and vertical beam size was 250.0 mm and 4.0 mm, respectively.

A double crystal monochromator was used to select an imaging beam energy of 29.994 keV using a pair of Si crystals both using the (2,2,0) lattice planes. The matched analyzer crystal was positioned between the mouse and the detector (G. K. Aulakh et al., 2018). The choice of reflection planes and imaging energy is based on reasonable lung contrast and reduced absorption contrast. A Photonic Science SCMOS (Photonic Science, UK) detector, was placed 1.1 m downstream. This detector has a 25 μm by 25 μm pixel size with a field of view of 100.03 (horizontal) by 6.625 (vertical) mm. Because of the limited beam size, the mice lungs were covered, on an average, over 7 vertical stage increments (each increment had a unidirectional 80 pixels overlap; thus, effective image area being 100.03 by 5.600 mm) or fields of view (FOV). Each field of view was imaged over 14 separate angular analyzer crystal settings (Table 1) with each acquisition time being 0.55 s/image.

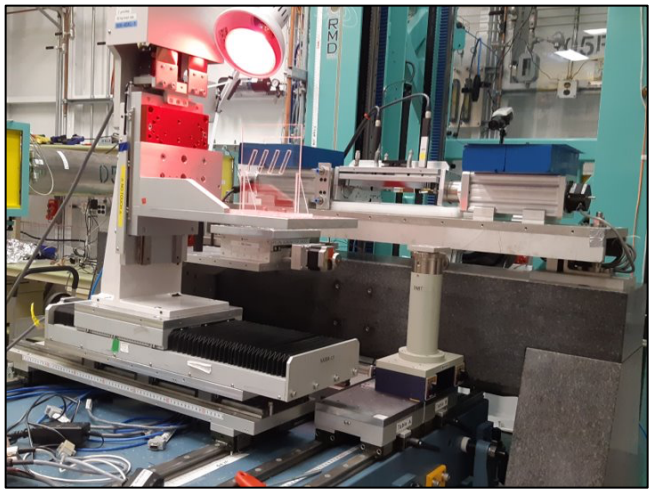

**Fig. 12.** Multiple image radiography (MIR) set-up inside the Biomedical Imaging and Therapy Bending Magnet (BMIT-BM) beamline imaging hutch

| Point | Before | After |
|---|---|---|
| 1 | -7.09 | -8.13 |
| 2 | -5.69 | -6.76 |
| 3 | -4.30 | -5.39 |
| 4 | -2.90 | -4.03 |
| 5 | -1.51 | -2.66 |
| 6 | -0.12 | -1.29 |
| 7 | 1.28 | 0.08 |
| 8 | 2.67 | 1.44 |
| 9 | 4.07 | 2.81 |
| 10 | 5.46 | 4.18 |
| 11 | 6.86 | 5.55 |

| | | |
|---|---|---|
| 12 | 8.25 | 6.91 |
| 13 | 9.65 | 8.28 |
| 14 | 11.04 | 9.65 |

**Table. 1:** Analyzer crystal angular positions (micro-radians) estimated from the flats obtained before and after imaging one group of mice at a given time point.

### *4.3.2 Mouse Ozone (O3) exposures*

The mice were housed in the veterinary college's animal care unit and transported a night before the day of CLS experiment. O3 exposures, at 0.05 ppm for 2 h, were performed in a custom-built chamber connected to in-line silent-arc discharge O3 calibrator & generator (2B Technologies, CO, US) on one end and O3 monitor (2B Technologies, CO, US) on the other end. Constant chamber air temperature (72 ±3°F) and relative humidity (50±15%) were maintained. Mice had the standard bedding and enrichment environment to mimic a standard housing cage (Au - Duda et al., 2021).

### *4.3.3. Intranasal LPS administration*

Mice were anesthetized under ketamine (100 mg/kg)/xylazine (5 mg/kg). A mouse was held upright with its back/dorsal side on the palm, holding the ears with the same hand(Au - Duda et al., 2021). Then, 50 µg/50 µl of the LPS solution was gently placed outside nostrils to let the mice inhale the liquid drop. Similarly, control mice are instilled with 50 µl sterile saline.

### *4.3.4 Mouse imaging protocol*

Two plexiglass mouse holders (Fig. 12) were custom built by the University of Saskatchewan's engineering shop. Three plexiglass partitions were equally spaced, at an angle of 45˚, in order to simultaneously image three mice (control, LPS and O3) over time. This design maximized the synchrotron beam's imaging capability by using the available beam

width. The mice were mounted at an angle of -45˚ (i.e., inclined counterclockwise when looking from the incident beam, Fig. 13) which provided refraction contrast of bronchial structures and transferred to the BMIT-BM beamlines hutch (Fig. 12). An infra-red heat lamp-maintained body temperature at 37 °C, and this was continuously monitored using a rectal probe (Figs. 12, 13). Eye lubrication gel protected the corneas. Fluid therapy was provided using bolus subcutaneous injection of normal saline (0.9% w/v: 0.06 ml per 10 mg body weight) every hour. Pulse oximetry was used to measure hemoglobin oxygen saturation (SpO2) by placing a probe on the right hind paw. The mice were maintained at normal body temperature and SpO2 remained at 99.9 ± 1% throughout the study. The breathing rate (180 ± 10 $min^{-1}$) was calculated by counting the number of diaphragmatic movements during 1 min from the control room using a camera directed towards mouse. Anesthesia was maintained with further 0.05–0.1 ml intraperitoneal injections with the same anesthetic combination and monitored remotely via breathing rate and $SpO_2$ as guide to vital signs (Fig. 13). Mice were imaged at baseline i.e., before any treatment, followed over time starting from immediately after the saline, O3 or LPS exposures i.e., 0 h, then followed at 24 h, 48 h and 70 h after respective exposures. As control mice received only saline and were housed in ambient room air, these mice served as time-matched controls for the x-ray imaging of LPS and O3 exposed mice. In this manner, a total of 15 mice accounting for 5 mice per treatment were imaged in groups of three.


**Fig. 13:** BMIT-BM Control Room Remote Image Monitoring of the mice and their vital signs. Note the inclined positioning of mice on the plexi-glass board.

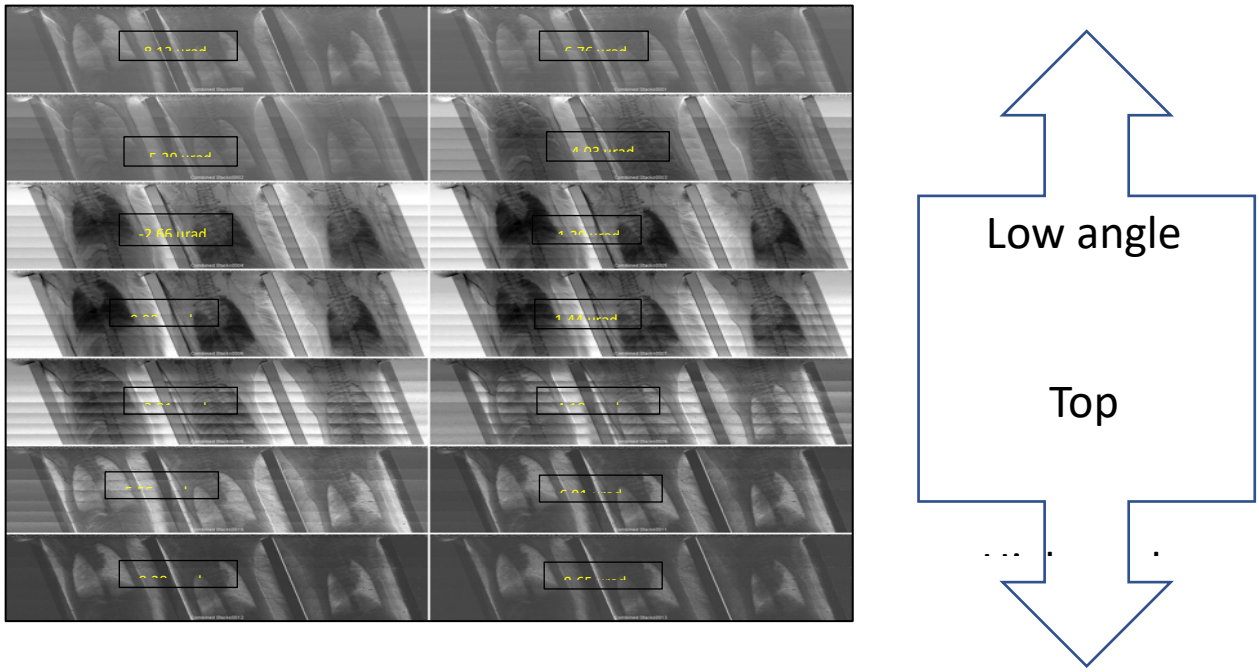


**Fig. 14.** Representative MIR data-set after dark and flat-field correction, stitching of 7 steps or fields of view (FOV) of mouse lung images collected across 14 angular analyzer positions (noted in yellow font on the top center of each image data point obtained from the flats 'after'). Note the flats intensity artifacts over the seven fields of views covering the lungs, especially at locations near the edges of the stitched images.

### *4.3.5 Multiple Image X-radiography (MIR) image analysis*

Following image acquisition, ImageJ (National Institutes of Health; rsbweb.nih.gov/ij/) and IDL (Interactive Data Language, Harris Geospatial Solutions, Inc.) software programs were employed to stich the entire lung from the 7 individual steps or fields of views (FOV). The flats before and after each imaging session was registered to correct for the vertical

drift. Normalization was achieved by recording a flat field with identical illumination to the experimental image but with no object and a dark image with the x-ray shutter closed. Identical exposure times were used for the experimental and the correction images (Fig. 14). Both the experimental image and the flat field image were first corrected by subtracting the dark image and then the dark corrected experimental image was divided by the dark corrected flat field image. Thus, the views were corrected for dark current and non-uniform beam intensity effects before execution of the MIR analysis in order to compute the amplitude, refraction, and the scatter width image (Hasnah et al., 2005; Hasnah et al., 2007).

The MIR analysis consisted of fitting the 14-point analyzer images, pixel-by-pixel, to a Gaussian function. The fitting parameters are the amplitude, angular center, and the width. Thus, the image dataset was reduced to three images (amplitude, refraction, and width). A fourth image referred to as “area” or “transmittance” was computed by combining the amplitude and the width images (Area = $\sqrt{2\pi}$ X amplitude X width). This area image represents the total of all the x-rays transmitted through the sample – thus we named it the area image. The negative log of the normalized area image is equivalent to a radiographic image and will be referred to as the “absorption” image. The refraction image is the angular displacement of the center of mass of the lung rocking curve with respect to the reference and measures the x-ray refraction angle in the vertical plane. The ultra-small-angle x-ray scattering is the lung rocking curve width

deconvolved from the reference rocking curve width which approximated by a Gaussian. This "width image" is a measure of ultra-small-angle x-ray scattering (USAXS) in vertical plane.

A data file stored all the information for MIR parameters for the entire dataset that was retrieved afterwards by a series of analysis programs. A thresholding operation was applied to the width image to delineate the lung outlines, which separate the lungs from the rest of the rectangular region.

The sum, average, median, standard deviation, skewness and kurtosis of absorption, width and absolute refraction angles were compared between mice from different treatments and time-points.

## 4.4 STATISTICAL ANALYSIS

Data were analyzed by two-way analysis of variance (GraphPad Prism 9 software, LLC, CA, US) to check for any effect of time or treatments on the above mentioned USAXS, amplitude, absorption or refraction parameters followed by Tukey's multiple comparisons as a post-hoc test.

## 4.5 RESULTS

### *4.5.1 Lung Ultra-small-angle-scatter (USAXS) is a sensitive parameter for longitudinal assessment of changes in lung air-tissue boundaries*

The USAXS image served as the template to segment out the lungs (Fig. 15e) and copy the same lung region in order to quantify the image parameters from USAXS, amplitude, refraction, and absorption images. Quantification of lung USAXS (scatter) revealed that the total or median lung width did not differ across treatments or time-points ($p>0.05$, Figs. 15a, b).

However, we did notice trends towards an earlier drop in net lung USAXS immediately after O3 exposure and 48 h after LPS exposure. Note that there is a slight trend towards higher scatter immediately after LPS and saline exposure. The frequency distribution of lung USAXS kurtosis was different, as time had a significant effect on USAXS kurtosis (p=0.0024). At 24 and 70 h time-point, the USAXS kurtosis was significantly higher in saline (p<0.05), LPS (p<0.05) or O3 (p<0.05) groups compared to their respective baseline group (p=0.0058) (Figs. 15d, e, 16a, b).

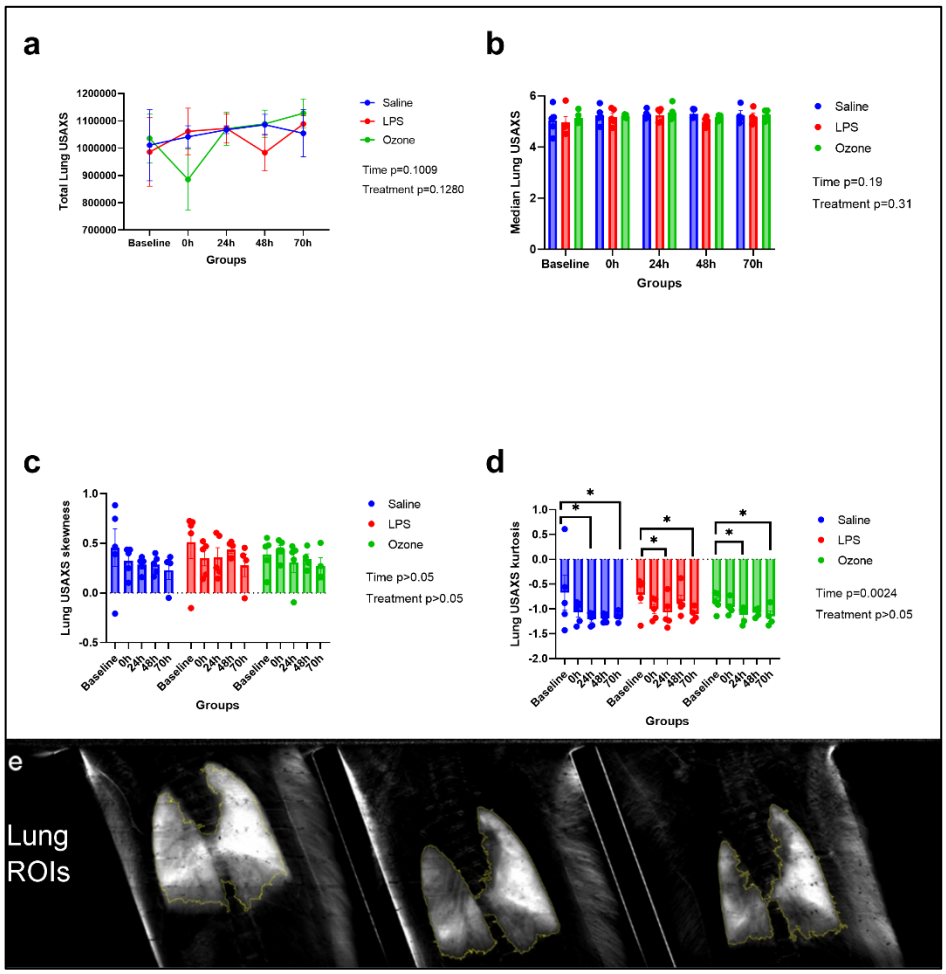


**Fig. 15. Lung USAXS parameters** (**a.** total lung USAXS, **b.** median lung USAXS, **c.** lung USAXS skewness, **d.** lung USAXS kurtosis) obtained after the gaussian fit program at baseline, 0, 24, 48 and 70 h post exposure. Note that the graphs were obtained after fitting the data using flat images acquired after the completion of imaging the MIR data-set. **e.** The lung regions were segmented, as shown by yellow outlines, by utilizing the threshold from the USAXS image. Time after respective exposures had a significant effect on the USAXS kurtosis

i.e., it's frequency distribution profile (p~0.05) indicating the scatter is a sensitive parameter for detecting changes in air-tissue boundaries after exposure to saline, O3 or LPS. Mice from groups or saline, LPS and O3, at baseline i.e., before any exposures, showed discrete or higher lung USAXS kurtosis distribution profile when compared to the respective groups at 24 ($p<0.05$) and 70 ($p<0.05$) h post exposure.

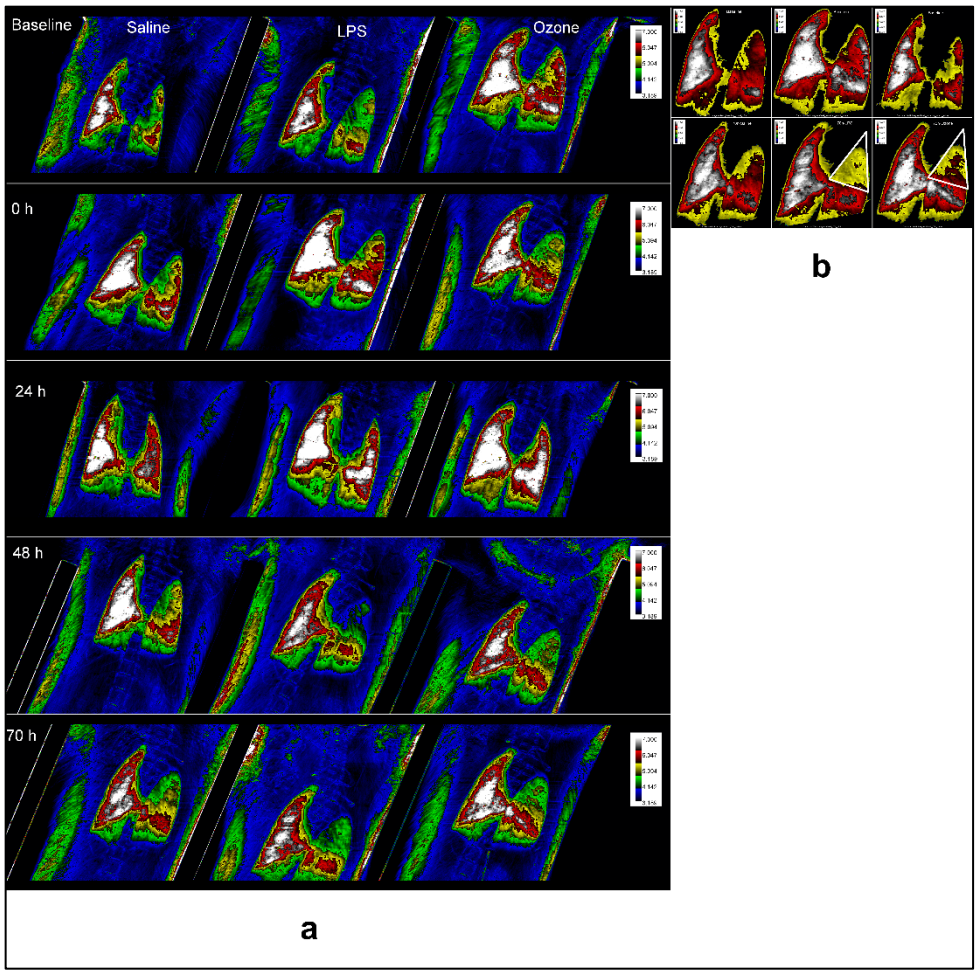


**Fig. 16. Representative regional USAXS (width/scatter) distribution in mouse lungs** at baseline, 0, 24, 48 and 70 h after saline, LPS or O3 exposure. **a.** The images are calibrated from 1.464 to 7.000 units on a 5-ramp color scale (shown on the images). **b.** The images on the right-hand side are calibrated from 0.000 to 7.000 units to highlight the compromised cranial lung regions in LPS and O3 exposed mice at 70 h time point. Note the regions (marked with white polyons) of the cranial lung where the USAXS intensity falls remarkably at 70 h, in LPS or O3, exposed mice.

### *4.5.2 Lung amplitude, refraction and absorption parameters are useful in delineating time-dependent changes in lung inflammation*

The amount of air in lungs is responsible for the transmittance of X-rays in the lung amplitude image observed in Figs. 17a, b, c, j. Thus, lesser tissue density should result in a higher lung amplitude, as recorded by the median lung amplitude values. There was a significant effect of time ($p=0.05$) on the median lung amplitude, refraction, and absorption, indicating variation in lung tissue density over time. The median refraction values were higher in the saline group, at baseline, when compared to the values at 0 ($p<0.05$), 24 ($p<0.05$) and 48 ($p<0.05$) h after O3 exposure. The change in refraction values indicate differences in macroscopic lung tissue to air boundaries over time. The median lung absorption, which is a derived parameter, from the amplitude and USAXS images, was significantly high in the O3 exposed groups after 24 ($p<0.001$), 48 ($p<0.001$) and 70 ($p<0.001$) h when compared to the respective saline treated group. Immediately after LPS exposure, the median lung absorption was higher, when compared at 48 h ($p<0.05$). Thus, MIR was successful in quantifying the different lung optical properties, observed in our current study to explore the effects of saline, LPS or O3 over a 70-h time-period.

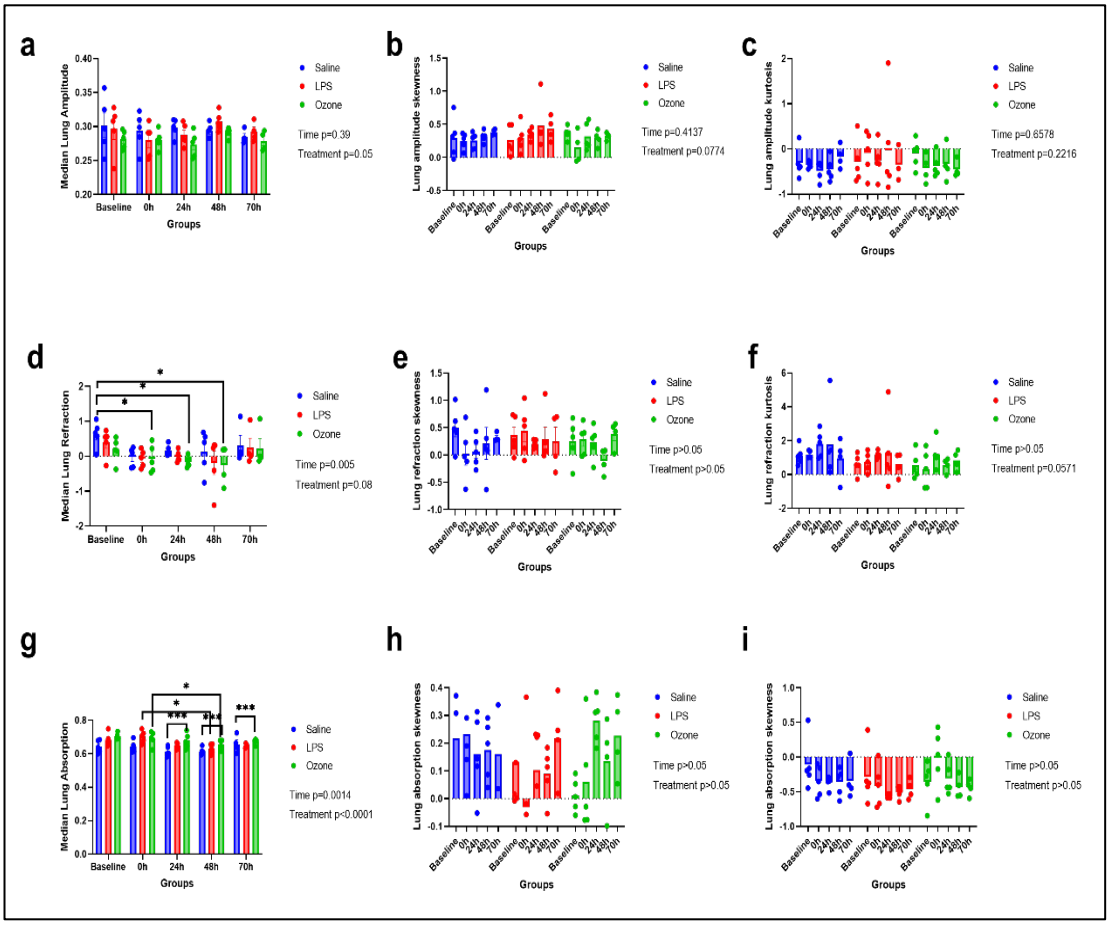


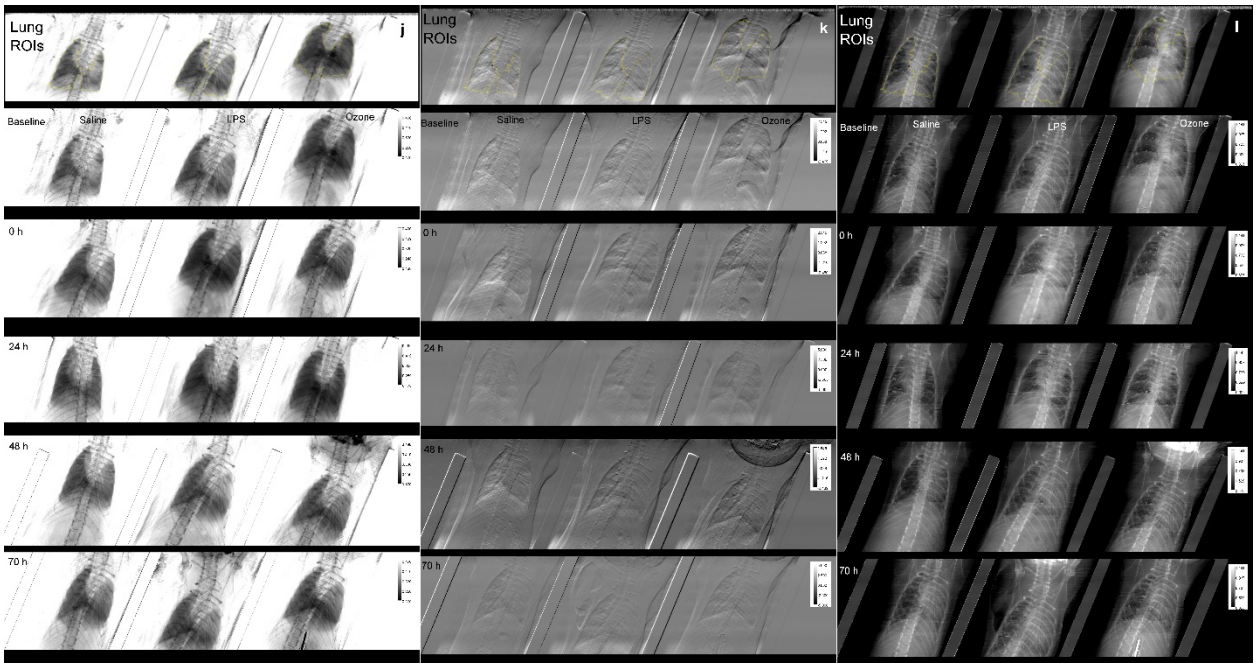


**Fig. 17. Lung MIR parameters** (**a.** median lung amplitude, **b.** lung amplitude skewness, **c.** lung amplitude kurtosis, **d.** median lung refraction, **e.** lung refraction skewness, **f.** lung refraction

kurtosis **g.** median lung absorption, **h.** lung absorption skewness, **i.** lung absorption kurtosis) obtained after the gaussian fit program at baseline, 0, 24, 48 and 70 h post exposure. Note that the graphs were obtained after fitting the data using flat images acquired after the completion of imaging the MIR data-set. The segmented lung regions, as shown by yellow outlines, after thresholding the USAXS image, were copied on to the **j.** amplitude**, k.** refraction and **l.** absorption images. Note the motion artifacts (observed as intense white pixels) over the seven fields of views covering the lungs, and the incongruency of flats with image data, at locations near the edges of the stitched images (pixel intensity gradation) in the refraction image. The image panels also show calibrated amplitude (from 0.170 to 0.490 units), refraction (from -2.469 to 2.545 microradians) and absorption (from 0.325 to 1.141 units) images from a representative group showing saline, LPS and O3 groups imaged before, 0, 24, 48 and 70 h after respective exposures. Treatment had a significant effect on median lung amplitude values ($p=0.05$). Time ($p=0.004$) had significant effect on median lung refraction values. The median lung refraction values in saline group, at baseline, was significantly high when compared to the median lung refraction values at 0 ($p<0.05$), 24 ($p<0.05$) and 48 ($p<0.05$) h after O3 exposure. Both time ($p=0.0014$) and treatment ($p<0.0001$), had significant effects on median lung absorption values. Saline group had significantly low median lung absorption values when compared to time-matched O3 treatment groups, at 24 ($P<0.001$), 48 ($p<0.001$) and 70 ($p<0.001$) h.

## 4.6 **DISCUSSION**

X-rays can penetrate through most tissues and are absorbed in bones and calcified structures. Tissues with high density block the x-rays and thus the detector would register black pixels behind the bones. On the other hand, thin tissues would let the x-rays pass through them and register as white pixels on the detector which are of an intensity corresponding to

the photons registered by the detector. These form the basis for the patterns observed on a negative x-ray film. When the film is developed, the pixels are inverted; thus, leading to the typical appearance of white bones and black tissues, other than calcified structures. In Diffraction Enhanced Imaging (DEI), there is an additional crystal, termed as the analyzer crystal, placed in between the object and the detector, which can be tilted or rocked within a miniscule range of angles, of the order of microradians, and thus effectively diffract the air-tissue boundaries in lungs, and other tissue edges i.e. wherever there are refractive index gradients, which are recorded as white pixels, usually a mix of the ultra-small angle scatter and refraction. When the analyzer crystal is in the way of the object (i.e., at the top position) as to block that object, it rejects all scatter and thus does not allow the x-rays to register the boundaries on the detector. This image is registered as black pixels and is called as the amplitude or the top image. The gradient in the analyzer crystal tilt i.e., the rocking angle, and the recorded scatter on the detector are recorded in a variant of DEI called as the Multiple Image Radiography (or MIR) (Chapman et al., 2006). The MIR USAXS scatter is thus hypothesized to be proportional to the number of such air-tissue boundaries in lung. However, in a free-breathing lung, rib movement and heartbeats can also contribute to the scatter. Thus, any gain in scatter width and a corresponding drop in amplitude, is indicative of more air-tissue boundaries. Therefore, any drop in the amplitude, is indicative of a gain in tissue density as in fluid build-up during inflammation observed during acute lung injury or fibrosis during chronic lung injury. The product of the square root of two times pi with the width and amplitude image is termed as the area or transmittance image. A negative log image of the area image is termed as an absorption image which is the equivalent of the clinical radiograph because it comprises of the scatter as well as the absorption components (G. K. Aulakh et al., 2018).

There are several differences in the images with the current study when compared to one by Aulakh et al in 2018(G. K. Aulakh et al., 2018). Firstly, our current study relies on stepwise acquisition of the MIR data-sets to cover the mouse lungs in contrast to the line-scan mode along with correction of analyzer tilt-error, used in the 2018 study. The flats were acquired before as well as after the acquisition of data from each mouse' imaging session. Thus, our present MIR acquisition led to a couple of alterations in the data analysis from the earlier study. The two flat rocking curves (before and after) were utilized to fit the lung MIR data-sets separately, which showed that the Flats "after" were more close to an optimal gaussian fit. This was likely due to the drift in the monochromator due to thermal expansion of the Silicon crystals over the period of imaging. The flats before and after were also offset from their center of mass for additional reasons such as the synchrotron beam decay as well as putative variations in the motor increment or step-up size. This resulted in banding at the edges of the different steps/fields of views, as well as near the moving parts of the free-breathing mouse lungs despite correcting for vertical displacement between flats and data images. Future analysis of the data will require aligning both before and after flats to create a single set of flats. The flats will need to be normalized in order to account for the beam decay. Then, these flats need to be angularly aligned with the data (i.e., lung) images.

As observed in our earlier study, the initial changes in the lungs scatter indicated trends towards an increase in the median lung scatter intensity, which attests to our earlier findings and adds to the fact that scatter is in-fact increased immediately after LPS induced lung injury. However, the median scatter intensity tends to fall at 48 h post LPS and 0 h after O3 treatment. The overall distribution of the frequency of lung scatter pixels is consistently observed towards the lower intensity values, in mice followed over 70 h after treatment with saline, LPS or

O3 when compared to baseline or unexposed mice. Intravital lung imaging from our group has shown that O3 increases the number of pores in the alveolar region, which could account for the maintenance of lung scatter properties. However, the lung scatter intensity profile tends to be diffuse i.e., shown by the low or flat kurtosis profile.

## 4.7 CONCLUSIONS

The current MIR imaging of lungs shows that a more detailed analysis of the lung ultra-small-angle scatter, amplitude and refraction are relevant parameters to follow over the course of lung inflammation. Our results indicate that the lung USAXS and refraction reduces (especially in the cranial part of left lung), with a corresponding increase in absorption upon exposure to LPS or O3 and is detectable up to 70 h time-period which was followed in the current study. The differences could be attributed to the anatomical differences in the single left lobe compared to the four right lung lobes such as lesser branching in left lung (Thiesse et al., 2010). However, during the curve fit of these gaussian parameters, we note that there are four major variables that affect the curve fit. First, as the mouse were free breathing, we observed motion artifacts over the seven fields of views covering the lungs, especially at locations near the edges of the lungs and ribs. These effects are even more pronounced in the refraction image. Secondly, the amount of time (approximately 10-15 minutes) that it takes to image the seven fields of view leads to decay of the synchrotron beam, also evident in the flats recorded before and after each mouse imaging. Thirdly, the variations in the beam across the horizontal axis leads to variations in the three mice. And lastly, the monochromator as well as analyzer drifts, due to thermal expansion of Si, likely account for changes across the different fields of view. Thus, future imaging should be aimed at more stable monochromator and analyzer positioning system, faster acquisition times, and larger fields of view to circumvent these artifacts.

# CHAPTER 5: DISCUSSION AND FUTURE DIRECTIONS

## 5.1 OVERALL DISCUSSION

The sequential lung imaging and analysis of O3 and LPS induced lung inflammation, reported in my thesis, is an attempt to explore the utility of (Micro-Positron Emission Tomography-Computed Tomography) micro-PET-CT and Multiple Image X-radiography (MIR) in non-invasive understanding of the kinetics of lung inflammation. We found unique features of pre-clinical application in both imaging modalities which will be discussed below.

The micro-PET-CT aimed at imaging mice first, at baseline, following the first intravenous (i.v.) [18F]F-FDG injection (2-5 MBq) and thereafter imaged immediately after injection, every 5-6 minutes for 25-30 minutes, which made up 5-6 imaging frames. Entire mouse was imaged over two-bed positions during each frame. At the end of PET imaging, a quick 1-minute X-ray CT was conducted. Mouse was then exposed to either 50 ug of intranasal LPS or 2 h of 0.05 ppm O3. Immediately after exposure (i.e., 0 h), the mouse was imaged again for residual [18F]F-FDG activity, in the manner described above. After 24 h of either exposure, i.v. [18F]F-FDG was again injected, and mouse was imaged with the same protocol. After 2-4 h, the mouse was again imaged for residual activity of the 2$^{nd}$ [18F]F-FDG injection. We plotted [18F]F-FDG lung SUR as a function of lung attenuation value (in arbitrary grey units) and observed interesting regional lung [18F]F-FDG distribution patterns. Baseline patterns showed cranio-caudal and ventro-dorsal gradients which were abolished irrespective of the LPS or O3 exposure. At 0 h, the O3 exposed lungs showed areas of extreme [18F]F-FDG inactivity in combination with [18F]F-FDG hot spots leading to a 72% increase in the [18F]F-FDG SUR compared to baseline values. At 0 h, the LPS exposed lungs showed lesser [18F]F-FDG SUR. The whole-body distribution revealed that lung [18F]F-FDG activity was higher and prolonged

up to 28 h in LPS compared to O3 exposed mice. While [18F]F-FDG is a useful marker to highlight areas with high metabolic uptake of glucose in cells such as neutrophils and macrophages recruited during inflammation, the resolution of PET-CT (hundreds of μm) precludes the evaluation of microscopic histopathologic changes especially in the alveoli. Using, binary masks of the available lung H&E stained cryosections, I assessed the ratio of lung and alveolar parenchyma to air spaces in mice left lungs exposed to 0.05 ppm O3 for 2 h. Our results from the X-ray CT lung tissue volume quantifications as well as the histologically derived percent-stained lung or alveolar area quantifications point towards significant damage that is observed as reduced percentage area as well as variability or standard deviation (S.D.) of binary lung images in mice immediately i.e., at 0 h and 6 h after exposure to 2 h of 0.05 ppm O3 exposure. Alveolar damage was also significant at 0 h as shown by reduction in percentage area and S.D. in the binary image region restricted to alveoli.

The synchrotron study aimed at following mice lungs before, immediately i.e., at 0 h, and thereafter at 24, 48 or 70 h after saline, bacterial lipopolysaccharide (LPS, 50 μg), or low dose (0.05 ppm for 2 h) O3 exposure. Our results indicate that the lung USAXS and refraction reduces (especially in the cranial part of left lung), with a corresponding increase in absorption upon exposure to LPS or O3 and is detectable up to 70 h time-period which was followed in the current study. The differences could be attributed to the anatomical differences in the single left lobe compared to the four right lung lobes such as lesser branching in left lung (Thiesse et al., 2010). The results from this study reflect the inter-dependence of the X-ray optical properties as the build-up of fluid in the inflamed lungs, as observed in LPS or O3 group, contribute increases in absorption but reduction in refraction and USAXS.

## 5.2 **FUTURE DIRECTIONS**

The microPET-CT study showed its applicability in evaluation of lung inflammation. However, there is a need to examine the total body [18F]F-FDG saturation after multiple injections. This can be conducted by repeating sequential [18F]F-FDG imaging in unexposed mice and quantifying the lung [18F]F-FDG SUR over time. If there is no saturation of [18F]F-FDG, the SUR should not decrease in unexposed mice upon re-injection. Moreover, the same mice should be assessed for lung histology post-mortem and evaluated for leukocyte sub-types.

The synchrotron MIR study showed that it is feasible to calculate the three X-ray optical properties but the MIR image set-up requires improvements such as the implementation of analyzer positioning system to correct for thermal crystal drifts (Glendon et al., 2013). The flats must be acquired at the same angular positions as of the object. The motion artifacts should be aimed at correcting through respiratory gating, in order to validate our free-breathing study. The current detector used for the MIR study had a 25 μm pixel size and a dynamic range of approximately 36,000 intensity units (on a 16-bit range). A detector with better dynamic range would ideally capture the scatter intensity from the thickest lung segments. Finally, future imaging should be aimed at more stable monochromator and analyzer positioning system, faster acquisition times, and larger fields of view to circumvent these artifacts.

# APPENDIX A

# H&E LUNG TISSUE QUANTIFICATION

## A.1 INTRODUCTION

The PET-CT evaluation of lungs over time has proven to be sensitive non-invasive procedure that assesses the distribution of radionuclide. In the first study, we utilized [18F]F-FDG PET-CT to evaluate its regional lung and whole-body distribution as well as lung CT-based total and tissue/fluid specific volume. In the second study, we imaged the mice lungs with MIR to visualize the changes that occurred up to 70 h showing build of fluid and loss of air-tissue boundaries in the upper regions of right and left lungs of mice. While [18F]F-FDG is a useful marker to highlight areas with high metabolic uptake of glucose in cells such as neutrophils and macrophages recruited during inflammation, the resolution of PET-CT (hundreds of μm) precludes the evaluation of microscopic histopathologic changes especially in the alveoli.

The hematoxylin and eosin (H&E) stain is the standard used for microscopic examination of tissues that have been fixed, embedded, and sectioned (Morton & Snider, 2017). Due to its ease and better results, it is usually performed by routine staining protocols. In H&E-stained tissues, the nucleic acids stain dark blue, and the proteins stain red to pink. If performed properly, staining of the H&E helps identify many pathological changes in the lung inflammation for a proper diagnosis. The first cells attracted to a site of injury are neutrophils followed by monocytes, lymphocytes (natural killer cells, NK cells), T cells, B cells and mast cells. Monocytes can differentiate into macrophages and dendritic cells and are recruited via chemotaxis into damaged tissues. Neutrophils are essential effector cells in the innate arm of the immune system**.** They constantly patrol the organism for signs of microbial infections, and when found, these cells quickly respond to trap and kill the invading pathogens. The primary role of

the neutrophil in acute inflammation is to phagocytose microorganisms and foreign materials. Neutrophils express and release cytokines, which amplify inflammatory reactions by several other cells of the immune system. The H&E stain also provides full detail about the microanatomy of organs and tissues.

Results from image analysis are more sensitive to variations in staining than microscopic evaluation by researchers (Gurcan et al., 2009). Using, binary masks of the lung H&E stained cryosections, I assessed the ratio of lung and alveolar parenchyma to air spaces in mice left lungs exposed to 0.05 ppm O3 for 2 h. Quantification was performed by using Fiji/ Image J software. Our results show that image analysis of H&E-stained tissue sections is a quick and viable method for assessing and verifying these parameters. Although, H&E staining quality and reproducibility are critical considerations in the interpretation of results, I found that the most important variable affecting the image analysis was the structural distortion due to broncho-alveolar lavage, vascular perfusion, and *in-situ* trachea-bronchial fixation procedure performed prior to the collection of lung tissue.

## A.2 MATERIALS AND METHODS

### A.2.1 **Tissues and slides**

The mouse left lung tissues (N=4 per group) were obtained from four different groups, collected in an earlier study performed in the Aulakh lab, namely baseline i.e., before exposure, immediately after 2 h of 0.05 ppm O3 exposure (0 h), 6 h after O3 exposure i.e. (6 h) and finally 22 h after O3 exposure (22 h). Left lung cryo-sections (of 5 μm thickness), representative of a typical middle ortho-slice, were taken out from the freezer stored boxes, and the tissue samples were assembled periodically. Selected tissues were chosen to perform the H&E staining protocol. Total lung capacity is the volume of air present in the chest after full inspiration. The total lung

capacity of the mouse is about 1 ml, and it measures the total amount of air in the lungs. The alveolar region is the most common site for gas exchange, and it takes place in the alveolar region (parenchyma), where air and blood are brought in proximity over a large surface. The alveolar region (parenchyma) of the lung comprises about 90% of its total volume**.** During respiration, the distal airspaces of the lung alveolar region change due to changes in the lung volumes. These changes in the lung volume can result in changes in the lung parameters, including length, surface area or volume (Cereda et al., 2016)**.**

### A.2.2 **Image analysis**

The stained H&E slides were imaged at 2x (Figs. A.1a-d) and 10x (Figs. A.2a-d) using identical exposures of the upright Olympus BX43 brightfield microscope in the histopathology lab. The images (*.tiff* files) were then converted into binary images using the automatic threshold function in ImageJ. The binary operation resulted in assignment of a value of 1 to the stained tissue and 0 to unstained tissue. After checking for the thresholded output against the original H&E image, each lung tissue slide was analyzed separately (Gurcan et al., 2009). The 2x images were divided into minimal number of rectangular regions of interest (ROI) that covered the maximum part of lung section, and devoid of structural distortion or microtome artifacts. In this way, a lung could be covered with 3-8 ROIs (Figs. A.1e-h). The 10x images were divided into 150 pixels by 150 pixels ROIs that were placed in a sequential manner in order to cover the alveolar region (Figs. A.2e-h). Every care was taken to avoid any peri-bronchiolar, peri-vascular, and bronchiolar, vascular regions. This procedure resulted in 150-300 alveolar ROIs per section. The ROIs were then utilized for measuring the percentage of stained lung tissue area as well as the variability or standard deviation (S.D.) in the distribution of these stained binary structures in

the entire lung or alveolar region(Dylag et al., 2020; Gurcan et al., 2009). The data files (.csv) were exported and compiled using excel and finally analyzed.

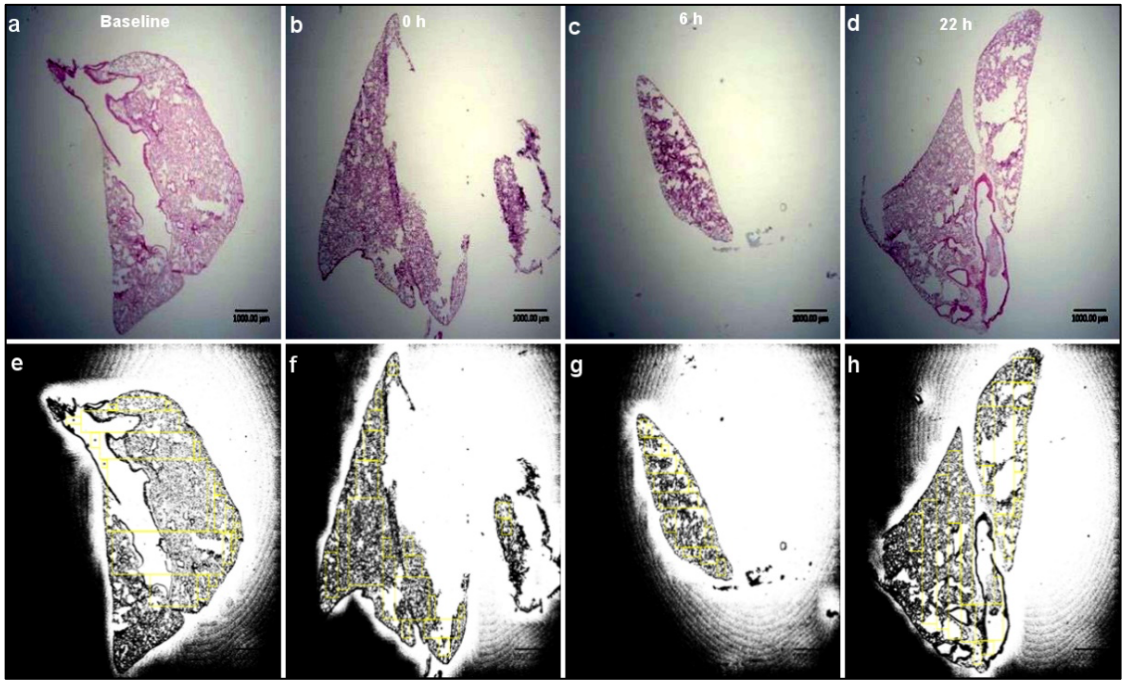


**Fig.A.1Representative 2X left lung cryo-sections stained with Hematoxylin & Eosin (a-d), converted into binary images** (e-h) from mice at four different time points, starting at baseline i.e., before exposure, immediately i.e., at 0h and at 6 and 22 h after 2 h of 0.05 ppm O3 treatment. Images taken from brightfield microscope at 2x. Scale bar is 100 µm.

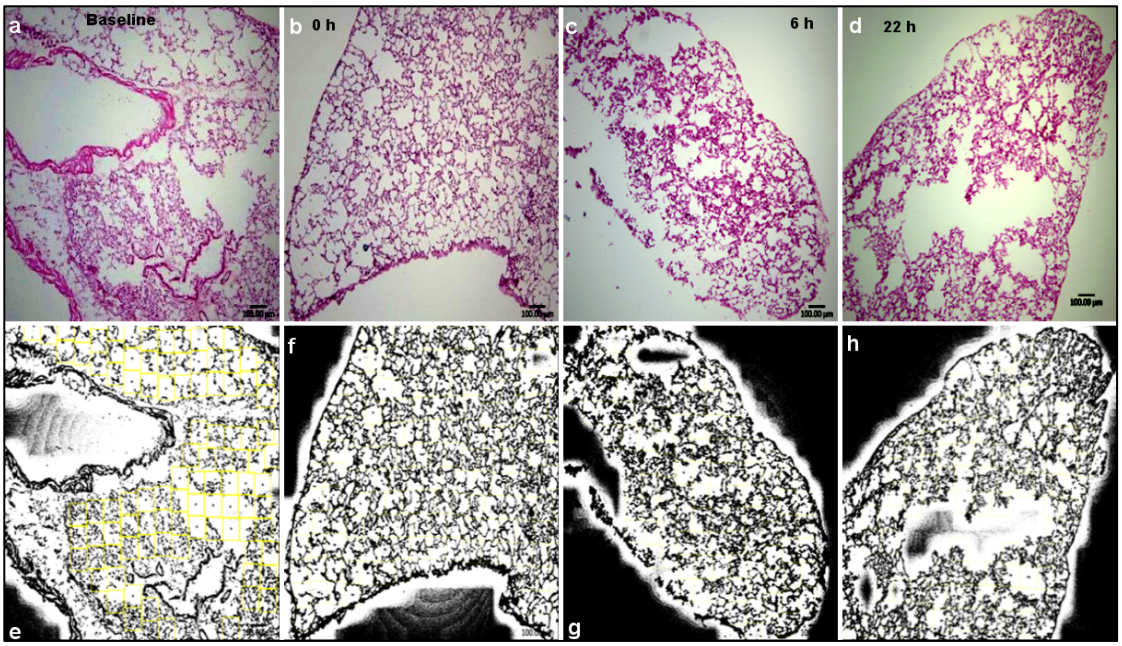


**Fig. A.2. Representative 10X left lung cryo-sections stained with Hematoxylin & Eosin (a-d), converted into binary images** (e-h) from mice lungs at four different time points, starting at baseline i.e., before exposure, immediately i.e., at 0h and at 6 and 22 h after 2 h of 0.05 ppm O3 treatment. Images taken from brightfield microscope at 10x. Scale bar is 100 µm.

## STATISTICAL ANALYSIS

The data were not normally distributed. Results are expressed as median with 95% CI. Percent total-stained tissue in lung S.D in anatomical lung structures at 2x and percent parenchyma in the alveolar region and S.D in lung alveoli at 10x were not normally distributed. Thus, the Kruskal-Wallis tests followed by post-hoc Tukey's multiple comparisons were used to analyze these endpoints. A $p < 0.05$ was set as the cut-off for significant differences across or between groups (Graphpad Prism 9, Graphpad Software, LLC v9.2.0).

## A.4 Results

At 2x (n=4), the multiple comparisons of the Kruskal-Wallis test showed that there was a significance at baseline (39.22% with 95% CI: 37.91-42.31%) vs 6 h (30.50% with 95% CI:

29.67-32.51%) with a $p<0.0001$ and 6 vs 22 h (38.26% with 95% CI: 34.39-40.78%) with a p-value of 0.00046, in the percentage (%) of stained lung area (Fig. A.3a). These results depict that there is significant reduction in the amount of stained lung tissue at 6 h but increases at 22 h due to the inflammatory response to O3. Over time there is an increase in tissue destruction from baseline to 6 h. Then there is a rebounding factor at 22 h due to an increase in cellularity and inflammation. At 2x, the S.D. in binary lung tissue structures is significantly high at baseline (194.5 with 95% CI: 123.7-126.0) vs 6 h (117.4 with 95% CI: 116.5-119.5) with a p-value of 0.001 and low at 6 vs. 22 h (123.9 with 95% CI: 121.1-125.3) with a p-value of 0.0048, due to the above-mentioned effects of O3 (Fig. A.3b). Again, the Kruskal-Wallis test for multiple comparisons was conducted at 10x for percent alveolar parenchymal area (n=4). We found out that there are additional significant changes at the 0 h (21.38% with 95% CI: 20.41-22.32%) time point ($p<0.0001$ compared to baseline (31.99% with 95% CI: 30.32-33.44%), $p<0.001$ compared to 6 h (24.84% with 95% CI: 23.82-25.71%)) in addition to the 22 h (26.03% with 95% CI: 24.96-27.08%) ($p<0.0001$) O3 treatment group (Fig. A.3c).

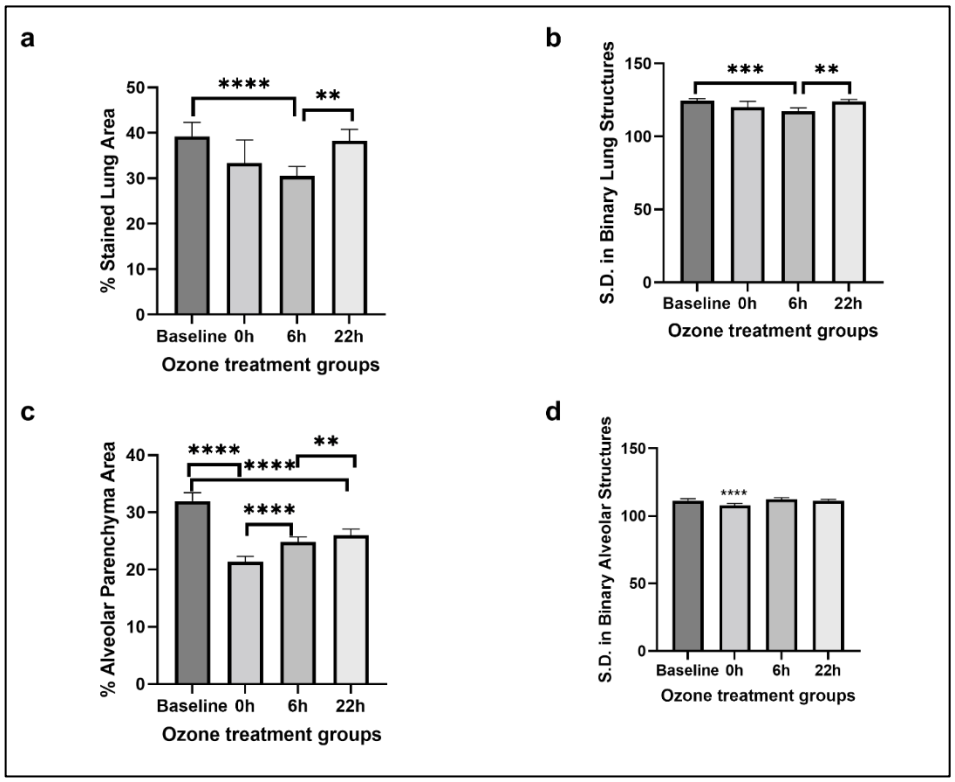


**Fig. A.3. Binary regions of interest (ROI) from 2X quantified** for the a) % stained lung area and b) variation or standard deviation (S.D.) in binary lung structures. **Binary regions of interest (ROI) from 10X quantified** for the c) % Alveolar Parenchyma Area and d) S.D in binary alveolar structures. ** denotes $p<0.01$, *** denotes $p<0.001$, **** denotes $p<0.00001$. N=4. Mice per group. Results are expressed as median with 95% CI.

We concluded that there is a lot of tissue damage occurring at 0 and 6 h with rebound lung leukocyte infiltration at 22 h post O3 exposure (Fig. A.3c). At 10x, multiple comparisons test showed that S.D in binary alveolar structures was significantly low at 0 h (107.8 with 95% CI: 105.8-109.3) with $p<0.0001$ compared to baseline (111.3 with 95% CI: 109.7-112.8) and the rest of O3 exposure groups (Fig. A.3d). Thus, the 10x analysis highlights the marked acute effects of O3 on the alveolar architecture compared to the 2x analysis.

## A.5 DISCUSSION

Acute exposure to O3 damages many compartments of lungs like the bronchiolar epithelium, bronchiolar and alveolar space enlargement along with inflammatory changes in the

alveolar septa, capillaries, and big vessels (Michaudel et al., 2018). Our results show similar changes as noted by an increase in the percentage of lung as well as alveolar area covered by air spaces. Moreover, we found that the variability in the binarized structures, as measured by standard deviation in lung and alveolar regions, reduces immediately after O3 exposure i.e., at 0 h, likely due to widening of the alveolar and bronchiolar spaces. Our findings corroborate with PET-CT results whereby we identified heterogenous regions of [18F]F-FDG uptake following O3 exposure (G. K. Aulakh et al., 2020b) due to the observation of regions with no uptake in O3 affected areas but enhanced uptake in the inflamed regions. As PET X-ray CT resolution enabled successful thresholding of lung tissue/fluid from air, and not tissue from accumulated fluid, the calculated total lung or tissue volumes after O3 exposure did not detect statistical differences before or after O3 exposure. Nevertheless, there were trends towards reduced lung tissue volume i.e., higher lung volume occupied by air-spaces after O3 exposure.

We noted the following artifacts in the lung sections: 1) The thick and thin sectioning is most often a result of poor technique at the cutting station due to the uneven rotation of the microtome. 2) These sections were obtained from a prior study where bronchoalveolar lavage, vascular perfusion and in-situ tracheobronchial fixation were performed before collecting the tissue. The lung architecture is noticeably perturbed. Therefore, the changes in standard deviation should be interpreted with extreme caution.

A microtome is a specialized cutting instrument that can be used for the accuracy and precision of slices sections from a block of embedded tissues. Different kinds of microtomes are used for additional section cutting based on your choice of an experiment. The H&E stain is part of tissue analysis in basic research and diagnostic pathology. Qualitative evaluation of stained

sections is considered necessary for clinical purposes, but the use of image analysis software serves as the best possible method for fulfilling the research objectives.

## A.6 CONCLUSIONS

Our results from the X-ray CT lung tissue volume quantifications as well as the histologically derived percent-stained lung or alveolar area quantifications point towards significant damage that is observed as reduced percentage area as well as variability or S.D. of binary lung images in mice immediately i.e., at 0 h and 6 h after exposure to 2 h of 0.05 ppm O3 exposure. At 24 h time-point, we observed a return in the percentage area as well as variability or S.D. of binary lung images likely due to ongoing inflammatory changes such as leukocyte recruitment and capillary dilatation. Alveolar damage was also significant at 0 h as shown by reduction in percentage area and S.D. in the binary image region restricted to alveoli.

## REFERENCES


Au - Duda, J. A. B., Au - Kaur, M., & Au - Aulakh, G. K. (2021). Visualizing Lung Cellular Adaptations during Combined Ozone and LPS Induced Murine Acute Lung Injury. *JoVE*(169), e62097. doi:doi:10.3791/62097

Aulakh, G. K. (2018). Neutrophils in the lung: "the first responders". *Cell Tissue Res, 371*(3), 577-588. doi:10.1007/s00441-017-2748-z

Aulakh, G. K., Brocos Duda, J. A., Guerrero Soler, C. M., Snead, E., & Singh, J. (2020a). Characterization of low-dose ozone-induced murine acute lung injury. *Physiol Rep, 8*(11), e14463. doi:10.14814/phy2.14463

Aulakh, G. K., Kaur, M., Brown, V., Ekanayake, S., Khan, B., & Fonge, H. (2020b). Quantification of regional murine ozone-induced lung inflammation using [18F]F-FDG microPET/CT imaging. *Sci Rep, 10*(1), 15699. doi:10.1038/s41598-020-72832-8

Aulakh, G. K., Mann, A., Belev, G., Wiebe, S., Kuebler, W. M., Singh, B., & Chapman, D. (2018). Multiple image x-radiography for functional lung imaging. *Physics in Medicine & Biology, 63*(1), 015009.

Aulakh, G. K., Singh, J., & Snead, E. (2019). Visualizing Cellular Adaptations during Ozone-induced Lung Inflammation. *The FASEB Journal, 33*(1_supplement), 767.711-767.711. doi:10.1096/fasebj.2019.33.1_supplement.767.11

Aulakh, G. K., Suri, S. S., & Singh, B. (2014). Angiostatin inhibits acute lung injury in a mouse model. *Am J Physiol Lung Cell Mol Physiol, 306*(1), L58-68. doi:10.1152/ajplung.00368.2012

Bajc, M., Neilly, B., Miniati, M., Mortensen, J., & Jonson, B. (2010). Methodology for ventilation/perfusion SPECT. *Semin Nucl Med, 40*(6), 415-425. doi:10.1053/j.semnuclmed.2010.07.002

Barreiro, O., Martín, P., González-Amaro, R., & Sánchez-Madrid, F. (2010). Molecular cues guiding inflammatory responses. *Cardiovasc Res, 86*(2), 174-182. doi:10.1093/cvr/cvq001

Bayat, S., Porra, L., Suortti, P., & Thomlinson, W. (2020). Functional lung imaging with synchrotron radiation: Methods and preclinical applications. *Physica Medica: European Journal of Medical Physics, 79*, 22-35. doi:10.1016/j.ejmp.2020.10.001

Bayat, S., Strengell, S., Porra, L., Janosi, T. Z., Petak, F., Suhonen, H., . . . Habre, W. (2009). Methacholine and ovalbumin challenges assessed by forced oscillations and synchrotron lung imaging. *Am J Respir Crit Care Med, 180*(4), 296-303. doi:10.1164/rccm.200808-1211OC

Bech, M., Tapfer, A., Velroyen, A., Yaroshenko, A., Pauwels, B., Hostens, J., . . . Pfeiffer, F. (2013). In-vivo dark-field and phase-contrast x-ray imaging. *Sci Rep, 3*, 3209. doi:10.1038/srep03209

Behnke, J., Kremer, S., Shahzad, T., Chao, C. M., Böttcher-Friebertshäuser, E., Morty, R. E., . . . Ehrhardt, H. (2020). MSC Based Therapies-New Perspectives for the Injured Lung. *J Clin Med, 9*(3). doi:10.3390/jcm9030682

Beitler, J. R., Sarge, T., Banner-Goodspeed, V. M., Gong, M. N., Cook, D., Novack, V., . . . Talmor, D. (2019). Effect of Titrating Positive End-Expiratory Pressure (PEEP) With an Esophageal Pressure-Guided Strategy vs an Empirical High PEEP-Fio2 Strategy on Death and Days Free From Mechanical Ventilation Among Patients With Acute

Respiratory Distress Syndrome: A Randomized Clinical Trial. *JAMA, 321*(9), 846-857. doi:10.1001/jama.2019.0555

Bouthillier, L., Vincent, R., Goegan, P., Adamson, I. Y., Bjarnason, S., Stewart, M., . . . Kumarathasan, P. (1998). Acute effects of inhaled urban particles and ozone: lung morphology, macrophage activity, and plasma endothelin-1. *Am J Pathol, 153*(6), 1873-1884. doi:10.1016/s0002-9440(10)65701-x

Bravin, A., Coan, P., & Suortti, P. (2012). X-ray phase-contrast imaging: from pre-clinical applications towards clinics. *Physics in Medicine and Biology, 58*(1), R1-R35. doi:10.1088/0031-9155/58/1/r1

Brocos, J. A., Aulakh, G. K., Snead, E., & Singh, J. (2019). Understanding Leukocyte Recruitment in Murine Ozone-Induced Lung Inflammation. *The FASEB Journal, 33*(1_supplement), 375.310-375.310. doi:10.1096/fasebj.2019.33.1_supplement.375.10

Broeckaert, F., Arsalane, K., Hermans, C., Bergamaschi, E., Brustolin, A., Mutti, A., & Bernard, A. (1999). Lung epithelial damage at low concentrations of ambient ozone. *Lancet, 353*(9156), 900-901. doi:10.1016/s0140-6736(99)00540-1

Cakmak, S., Hebbern, C., Pinault, L., Lavigne, E., Vanos, J., Crouse, D. L., & Tjepkema, M. (2018). Associations between long-term PM2.5 and ozone exposure and mortality in the Canadian Census Health and Environment Cohort (CANCHEC), by spatial synoptic classification zone. *Environment International, 111*, 200-211. doi:https://doi.org/10.1016/j.envint.2017.11.030

Cereda, M., Xin, Y., Goffi, A., Herrmann, J., Kaczka, D. W., Kavanagh, B. P., . . . Rizi, R. R. (2019). Imaging the Injured Lung: Mechanisms of Action and Clinical Use. *Anesthesiology, 131*(3), 716-749. doi:10.1097/aln.0000000000002583

Cereda, M., Xin, Y., Meeder, N., Zeng, J., Jiang, Y., Hamedani, H., . . . Rizi, R. R. (2016). Visualizing the Propagation of Acute Lung Injury. *Anesthesiology, 124*(1), 121-131. doi:10.1097/ALN.0000000000000916

Chapman, D., Nesch, I., Hasnah, M. O., & Morrison, T. I. (2006). X-ray optics for emission line X-ray source diffraction enhanced systems. *Nuclear Instruments and Methods in Physics Research, Section A: Accelerators, Spectrometers, Detectors and Associated Equipment, 562*(1), 461-467. doi:10.1016/j.nima.2006.02.185

Chapman, D., Pisano, E., Thomlinson, W., Zhong, Z., Johnston, R. E., Washburn, D., . . . Malinowska, K. (1998). Medical applications of diffraction enhanced imaging. *Breast Disease, 10*(3-4), 197-207.

Chapman, D., Thomlinson, W., Johnston, R. E., Washburn, D., Pisano, E., Gmür, N., . . . Sayers, D. (1997). Diffraction enhanced x-ray imaging. *Physics in Medicine and Biology, 42*(11), 2015-2025. doi:10.1088/0031-9155/42/11/001

Charo, I. F., & Ransohoff, R. M. (2006). The Many Roles of Chemokines and Chemokine Receptors in Inflammation. *New England Journal of Medicine, 354*(6), 610-621. doi:10.1056/NEJMra052723

Chen, D. L., Bedient, T. J., Kozlowski, J., Rosenbluth, D. B., Isakow, W., Ferkol, T. W., . . . Walter, M. J. (2009). [18F]fluorodeoxyglucose positron emission tomography for lung antiinflammatory response evaluation. *Am J Respir Crit Care Med, 180*(6), 533-539. doi:10.1164/rccm.200904-0501OC

Chen, D. L., Cheriyan, J., Chilvers, E. R., Choudhury, G., Coello, C., Connell, M., . . . Wilson, F. J. (2017). Quantification of Lung PET Images: Challenges and Opportunities. *Journal of Nuclear Medicine, 58*(2), 201-207. doi:10.2967/jnumed.116.184796

Chen, D. L., Ferkol, T. W., Mintun, M. A., Pittman, J. E., Rosenbluth, D. B., & Schuster, D. P. (2006). Quantifying pulmonary inflammation in cystic fibrosis with positron emission tomography. *Am J Respir Crit Care Med, 173*(12), 1363-1369. doi:10.1164/rccm.200506-934OC

Cheung, O.-Y., Graziano, P., & Smith, M. L. (2018). Acute Lung Injury. *Practical Pulmonary Pathology: A Diagnostic Approach*, 125-146.e123. doi:10.1016/B978-0-323-44284-8.00006-5

Dauchet, L., Hulo, S., Cherot-Kornobis, N., Matran, R., Amouyel, P., Edme, J. L., & Giovannelli, J. (2018). Short-term exposure to air pollution: Associations with lung function and inflammatory markers in non-smoking, healthy adults. *Environ Int, 121*(Pt 1), 610-619. doi:10.1016/j.envint.2018.09.036

de Prost, N., Tucci, M. R., & Melo, M. F. (2010). Assessment of lung inflammation with 18F-FDG PET during acute lung injury. *AJR Am J Roentgenol, 195*(2), 292-300. doi:10.2214/ajr.10.4499

Delfino, R. J., Murphy-Moulton, A. M., Burnett, R. T., Brook, J. R., & Becklake, M. R. (1997). Effects of air pollution on emergency room visits for respiratory illnesses in Montreal, Quebec. *Am J Respir Crit Care Med, 155*(2), 568-576. doi:10.1164/ajrccm.155.2.9032196

Devlin, R. B., McDonnell, W. F., Mann, R., Becker, S., House, D. E., Schreinemachers, D., & Koren, H. S. (1991). Exposure of humans to ambient levels of ozone for 6.6 hours causes cellular and biochemical changes in the lung. *Am J Respir Cell Mol Biol, 4*(1), 72-81. doi:10.1165/ajrcmb/4.1.72

Dong, Z., & Yuan, Y. (2018). Accelerated inflammation and oxidative stress induced by LPS in acute lung injury: Inhibition by ST1926. *Int J Mol Med, 41*(6), 3405-3421. doi:10.3892/ijmm.2018.3574

Donne, M. L., Lechner, A. J., & Rock, J. R. (2015). Evidence for lung epithelial stem cell niches. *BMC Dev Biol, 15*, 32. doi:10.1186/s12861-015-0082-9

Driscoll, K. E., Vollmuth, T. A., & Schlesinger, R. B. (1987). Acute and subchronic ozone inhalation in the rabbit: response of alveolar macrophages. *J Toxicol Environ Health, 21*(1-2), 27-43. doi:10.1080/15287398709531000

Dylag, A. M., Haak, J., Yee, M., & O'Reilly, M. A. (2020). Pulmonary mechanics and structural lung development after neonatal hyperoxia in mice. *Pediatr Res, 87*(7), 1201-1210. doi:10.1038/s41390-019-0723-y

Ehsan Samei, D. J. P. (2019). Nuclear Medicine. In *Hendee's Physics of Medical Imaging* (pp. 271-304): John Wiley & Sons.

Eling, L., Bouchet, A., Nemoz, C., Djonov, V., Balosso, J., Laissue, J., . . . Serduc, R. (2019). Ultra high dose rate Synchrotron Microbeam Radiation Therapy. Preclinical evidence in view of a clinical transfer. *Radiother Oncol, 139*, 56-61. doi:10.1016/j.radonc.2019.06.030

Ellis, H. (2011). The lungs. *Anaesthesia & Intensive Care Medicine, 12*(11), 501-503. doi:https://doi.org/10.1016/j.mpaic.2011.08.007

Evangelista, L., Ravelli, I., Magnani, F., Iacobone, M., Giraudo, C., Camozzi, V., . . . Cecchin, D. (2020). (18)F-choline PET/CT and PET/MRI in primary and recurrent hyperparathyroidism: a systematic review of the literature. *Ann Nucl Med, 34*(9), 601-619. doi:10.1007/s12149-020-01507-1

Giuranno, L., Ient, J., De Ruysscher, D., & Vooijs, M. A. (2019). Radiation-Induced Lung Injury (RILI). *Front Oncol, 9*, 877. doi:10.3389/fonc.2019.00877

Glendon, R., George, B., Alan, R., & Dean, C. (2013). A Novel Analyzer Control System for Diffraction Enhanced Imaging. *Journal of Physics: Conference Series, 425*(2), 022003.

Gradl, R., Dierolf, M., Yang, L., Hehn, L., Günther, B., Möller, W., . . . Morgan, K. S. (2019). Visualizing treatment delivery and deposition in mouse lungs using in vivo x-ray imaging. *J Control Release, 307*, 282-291. doi:10.1016/j.jconrel.2019.06.035

Groves, A. M., Gow, A. J., Massa, C. B., Hall, L., Laskin, J. D., & Laskin, D. L. (2013). Age-related increases in ozone-induced injury and altered pulmonary mechanics in mice with progressive lung inflammation. *American Journal of Physiology-Lung Cellular and Molecular Physiology, 305*(8), L555-L568. doi:10.1152/ajplung.00027.2013

Groves, A. M., Gow, A. J., Massa, C. B., Laskin, J. D., & Laskin, D. L. (2012). Prolonged injury and altered lung function after ozone inhalation in mice with chronic lung inflammation. *Am J Respir Cell Mol Biol, 47*(6), 776-783. doi:10.1165/rcmb.2011-0433OC

Guo, H., Xu, K., Duan, G., Wen, L., & He, Y. (2022). Progress and future prospective of FDG-PET/CT imaging combined with optimized procedures in lung cancer: toward precision medicine. *Ann Nucl Med, 36*(1), 1-14. doi:10.1007/s12149-021-01683-8

Gurcan, M. N., Boucheron, L. E., Can, A., Madabhushi, A., Rajpoot, N. M., & Yener, B. (2009). Histopathological image analysis: a review. *IEEE reviews in biomedical engineering, 2*, 147-171. doi:10.1109/RBME.2009.2034865

Han, S., & Mallampalli, R. K. (2015). The acute respiratory distress syndrome: from mechanism to translation. *J Immunol, 194*(3), 855-860. doi:10.4049/jimmunol.1402513

Harris, R. S., Venegas, J. G., Wongviriyawong, C., Winkler, T., Kone, M., Musch, G., . . . Medoff, B. D. (2011). 18F-FDG uptake rate is a biomarker of eosinophilic inflammation and airway response in asthma. *J Nucl Med, 52*(11), 1713-1720. doi:10.2967/jnumed.110.086355

Hasnah, M. O., Parham, C., Pisano, E. D., Zhong, Z., Oltulu, O., & Chapman, D. (2005). Mass density images from the diffraction enhanced imaging technique. *Med Phys, 32*(2), 549-552. doi:10.1118/1.1852794

Hasnah, M. O., Zhong, Z., Parham, C., Zhang, H., & Chapman, D. (2007). Compositional images from the Diffraction Enhanced Imaging technique. *Nuclear Instruments and Methods in Physics Research, Section A: Accelerators, Spectrometers, Detectors and Associated Equipment, 572*(2), 953-957. doi:10.1016/j.nima.2006.11.066

Heuss, J. M., Nebel, G. J., & Colucci, J. M. (1971). National air quality standards for automotive pollutants--a critical review. *J Air Pollut Control Assoc, 21*(9), 535-544. doi:10.1080/00022470.1971.10469565

Hofheinz, F., Hoff, J., Steffen, I. G., Lougovski, A., Ego, K., Amthauer, H., & Apostolova, I. (2016). Comparative evaluation of SUV, tumor-to-blood standard uptake ratio (SUR), and dual time point measurements for assessment of the metabolic uptake rate in FDG PET. *EJNMMI Res, 6*(1), 53. doi:10.1186/s13550-016-0208-5

Hollingsworth, J. W., Kleeberger, S. R., & Foster, W. M. (2007). Ozone and pulmonary innate immunity. *Proc Am Thorac Soc, 4*(3), 240-246. doi:10.1513/pats.200701-023AW

Hu, Y., Chi, L., Kuebler, W. M., & Goldenberg, N. M. (2020). Perivascular Inflammation in Pulmonary Arterial Hypertension. *Cells, 9*(11), 2338.

Jamar, F., Buscombe, J., Chiti, A., Christian, P. E., Delbeke, D., Donohoe, K. J., . . . Signore, A. (2013). EANM/SNMMI guideline for 18F-FDG use in inflammation and infection. *J Nucl Med, 54*(4), 647-658. doi:10.2967/jnumed.112.112524

Johnston, R. E., Washburn, D., Pisano, E., Burns, C., Thomlinson, W. C., Chapman, L. D., . . . Sayers, D. (1996). Mammographic phantom studies with synchrotron radiation. *Radiology, 200*(3), 659-663. doi:10.1148/radiology.200.3.8756911

Kasahara, D. I., Kim, H. Y., Mathews, J. A., Verbout, N. G., Williams, A. S., Wurmbrand, A. P., . . . Shore, S. A. (2014). Pivotal role of IL-6 in the hyperinflammatory responses to subacute ozone in adiponectin-deficient mice. *Am J Physiol Lung Cell Mol Physiol, 306*(6), L508-520. doi:10.1152/ajplung.00235.2013

Kenyon, N. J., Last, M. S., Eiserich, J. P., Morrissey, B. M., Temple, L. M., & Last, J. A. (2006). Differentiation of the roles of NO from airway epithelium and inflammatory cells in ozone-induced lung inflammation. *Toxicol Appl Pharmacol, 215*(3), 250-259. doi:10.1016/j.taap.2006.03.005

Khelashvili, G., Brankov, J. G., Chapman, D., Anastasio, M. A., Yang, Y., Zhong, Z., & Wernick, M. N. (2006). A physical model of multiple-image radiography. *Physics in Medicine and Biology, 51*(2), 221-236. doi:10.1088/0031-9155/51/2/003

Koo, V., Hamilton, P. W., & Williamson, K. (2006). Non-invasive in vivo imaging in small animal research. *Cell Oncol, 28*(4), 127-139. doi:10.1155/2006/245619

Kusmirek, J. E., Magnusson, J. D., & Perlman, S. B. (2020). Current Applications for Nuclear Medicine Imaging in Pulmonary Disease. *Current Pulmonology Reports, 9*(3), 82-95. doi:10.1007/s13665-020-00251-1

Låg, M., Øvrevik, J., Refsnes, M., & Holme, J. A. (2020). Potential role of polycyclic aromatic hydrocarbons in air pollution-induced non-malignant respiratory diseases. *Respiratory research, 21*(1), 299. doi:10.1186/s12931-020-01563-1

Larcombe, A. N., Foong, R. E., Bozanich, E. M., Berry, L. J., Garratt, L. W., Gualano, R. C., . . . Sly, P. D. (2011). Sexual dimorphism in lung function responses to acute influenza A infection. *Influenza Other Respir Viruses, 5*(5), 334-342. doi:10.1111/j.1750-2659.2011.00236.x

Lewis, R. A., Yagi, N., Kitchen, M. J., Morgan, M. J., Paganin, D., Siu, K. K. W., . . . Hooper, S. B. (2005). Dynamic imaging of the lungs using x-ray phase contrast. *Physics in Medicine and Biology, 50*(21), 5031-5040. doi:10.1088/0031-9155/50/21/006

Ley, K., Laudanna, C., Cybulsky, M. I., & Nourshargh, S. (2007). Getting to the site of inflammation: the leukocyte adhesion cascade updated. *Nature reviews.Immunology, 7*(9), 678-689. doi:10.1038/nri2156

Lorente, J. A., Nin, N., & Esteban, A. (2012). Biomarkers of Acute Lung Injury. In J.-L. Vincent (Ed.), *Annual Update in Intensive Care and Emergency Medicine 2012* (pp. 160-170). Berlin, Heidelberg: Springer Berlin Heidelberg.

Lou, J., Hu, Y., Wu, M.-d., Che, L.-q., Wu, Y.-f., Zhao, Y., . . . Shen, H.-h. (2019). Endothelial cell-specific anticoagulation reduces inflammation in a mouse model of acute lung injury. *Acta Pharmacologica Sinica, 40*(6), 769-780. doi:10.1038/s41401-018-0175-7

Manzer, R., Dinarello, C. A., McConville, G., & Mason, R. J. (2008). Ozone exposure of macrophages induces an alveolar epithelial chemokine response through IL-1alpha. *Am J Respir Cell Mol Biol, 38*(3), 318-323. doi:10.1165/rcmb.2007-0250OC

Markle, J. G., Frank, D. N., Mortin-Toth, S., Robertson, C. E., Feazel, L. M., Rolle-Kampczyk, U., . . . Danska, J. S. (2013). Sex differences in the gut microbiome drive hormone-dependent regulation of autoimmunity. *Science, 339*(6123), 1084-1088. doi:10.1126/science.1233521

Marks, L. B., Munley, M. T., Bentel, G. C., Zhou, S. M., Hollis, D., Scarfone, C., . . . Anscher, M. (1997). Physical and biological predictors of changes in whole-lung function following thoracic irradiation. *Int J Radiat Oncol Biol Phys, 39*(3), 563-570. doi:10.1016/s0360-3016(97)00343-x

Matute-Bello, G., Downey, G., Moore, B. B., Groshong, S. D., Matthay, M. A., Slutsky, A. S., & Kuebler, W. M. (2011). An official American Thoracic Society workshop report: features and measurements of experimental acute lung injury in animals. *Am J Respir Cell Mol Biol, 44*(5), 725-738. doi:10.1165/rcmb.2009-0210ST

Matute-Bello, G., Frevert, C. W., & Martin, T. R. (2008). Animal models of acute lung injury. *Am J Physiol Lung Cell Mol Physiol, 295*(3), L379-399. doi:10.1152/ajplung.00010.2008

Meinel, F. G., Schwab, F., Schleede, S., Bech, M., Herzen, J., Achterhold, K., . . . Nikolaou, K. (2013). Diagnosing and mapping pulmonary emphysema on X-ray projection images: incremental value of grating-based X-ray dark-field imaging. *PLoS One, 8*(3), e59526. doi:10.1371/journal.pone.0059526

Meyerholz, D. K., Sieren, J. C., Beck, A. P., & Flaherty, H. A. (2017). Approaches to Evaluate Lung Inflammation in Translational Research. *Veterinary Pathology, 55*(1), 42-52. doi:10.1177/0300985817726117

Michaudel, C., Fauconnier, L., Jule, Y., & Ryffel, B. (2018). Functional and morphological differences of the lung upon acute and chronic ozone exposure in mice. *Sci Rep, 8*(1), 10611. doi:10.1038/s41598-018-28261-9

Miller, F. J., Mercer, R. R., & Crapo, J. D. (1993). Lower Respiratory Tract Structure of Laboratory Animals and Humans: Dosimetry Implications. *Aerosol Science and Technology, 18*(3), 257-271. doi:10.1080/02786829308959603

Min, J. J., & Gambhir, S. S. (2008). Molecular imaging of PET reporter gene expression. *Handb Exp Pharmacol*(185 Pt 2), 277-303. doi:10.1007/978-3-540-77496-9_12

Mishra, V., DiAngelo, S. L., & Silveyra, P. (2016). Sex-specific IL-6-associated signaling activation in ozone-induced lung inflammation. *Biol Sex Differ, 7*, 16. doi:10.1186/s13293-016-0069-7

Mitchell, S., Vargas, J., & Hoffmann, A. (2016). Signaling via the NFκB system. *Wiley Interdiscip Rev Syst Biol Med, 8*(3), 227-241. doi:10.1002/wsbm.1331

Moitra, J., Evenoski, C., Sammani, S., Wadgaonkar, R., Turner, J. R., Ma, S. F., & Garcia, J. G. (2008). A transgenic mouse with vascular endothelial over-expression of the non-muscle myosin light chain kinase-2 isoform is susceptible to inflammatory lung injury: role of sexual dimorphism and age. *Transl Res, 151*(3), 141-153. doi:10.1016/j.trsl.2007.12.008

Mokra, D., Mikolka, P., Kosutova, P., & Mokry, J. (2019). Corticosteroids in Acute Lung Injury: The Dilemma Continues. *International Journal of Molecular Sciences, 20*(19), 4765.

Morgan, K. S., Parsons, D., Cmielewski, P., McCarron, A., Gradl, R., Farrow, N., . . . Donnelley, M. (2020). Methods for dynamic synchrotron X-ray respiratory imaging in live animals. *Journal of Synchrotron Radiation, 27*(1), 164-175. doi:doi:10.1107/S1600577519014863

Morton, J., & Snider, T. A. (2017). Guidelines for collection and processing of lungs from aged mice for histological studies. *Pathobiology of Aging & Age-related Diseases, 7*(1), 1313676. doi:10.1080/20010001.2017.1313676

Mumby, S., Chung, K. F., & Adcock, I. M. (2019). Transcriptional Effects of Ozone and Impact on Airway Inflammation. *Front Immunol, 10*, 1610. doi:10.3389/fimmu.2019.01610

Netea, M. G., Balkwill, F., Chonchol, M., Cominelli, F., Donath, M. Y., Giamarellos-Bourboulis, E. J., . . . Dinarello, C. A. (2017). A guiding map for inflammation. *Nat Immunol, 18*(8), 826-831. doi:10.1038/ni.3790

Neudecker, V., Brodsky, K. S., Clambey, E. T., Schmidt, E. P., Packard, T. A., Davenport, B., . . . Eltzschig, H. K. (2017). Neutrophil transfer of miR-223 to lung epithelial cells dampens acute lung injury in mice. *Science Translational Medicine, 9*(408), eaah5360. doi:doi:10.1126/scitranslmed.aah5360

Nguyen, L., Castro, O., De Dios, R., Sandoval, J., McKenna, S., & Wright, C. J. (2019). Sex-differences in LPS-induced neonatal lung injury. *Sci Rep, 9*(1), 8514. doi:10.1038/s41598-019-44955-0

Nieman, G. F., Al-Khalisy, H., Kollisch-Singule, M., Satalin, J., Blair, S., Trikha, G., . . . Habashi, N. M. (2020). A Physiologically Informed Strategy to Effectively Open, Stabilize, and Protect the Acutely Injured Lung. *Frontiers in physiology, 11*, 227. doi:10.3389/fphys.2020.00227

Niethamer, T. K., Stabler, C. T., Leach, J. P., Zepp, J. A., Morley, M. P., Babu, A., . . . Morrisey, E. E. (2020). Defining the role of pulmonary endothelial cell heterogeneity in the response to acute lung injury. *Elife, 9*. doi:10.7554/eLife.53072

Nolan, K. E., Baer, L. A., Karekar, P., Nelson, A. M., Stanford, K. I., Doolittle, L. M., . . . Davis, I. C. (2021). Metabolic shifts modulate lung injury caused by infection with H1N1 influenza A virus. *Virology, 559*, 111-119. doi:10.1016/j.virol.2021.03.008

Ostroukhova, M., Goplen, N., Karim, M. Z., Michalec, L., Guo, L., Liang, Q., & Alam, R. (2012). The role of low-level lactate production in airway inflammation in asthma. *Am J Physiol Lung Cell Mol Physiol, 302*(3), L300-307. doi:10.1152/ajplung.00221.2011

Peterson, M. L., Harder, S., Rummo, N., & House, D. (1978). Effect of ozone on leukocyte function in exposed human subjects. *Environ Res, 15*(3), 485-493.

Pourfathi, M., Kadlecek, S. J., Chatterjee, S., & Rizi, R. R. (2020). Metabolic Imaging and Biological Assessment: Platforms to Evaluate Acute Lung Injury and Inflammation. *Frontiers in physiology, 11*, 937-937. doi:10.3389/fphys.2020.00937

Proudfoot, A. G., McAuley, D. F., Griffiths, M. J. D., & Hind, M. (2011). Human models of acute lung injury. *Disease Models & Mechanisms, 4*(2), 145-153. doi:10.1242/dmm.006213

Rao, D. V., Yuasa, T., Akatsuka, T., Tromba, G., Hasan, M. Z., Takeda, T., & Devaraj, B. (2006). Images of biological soft tissue using synchrotron X-ray and laser CT systems. *Radiation Measurements, 41*(2), 177-182. doi:https://doi.org/10.1016/j.radmeas.2005.07.021

Rhoades, G. W., Belev, G. S., Chapman, L. D., Wiebe, S. P., Cooper, D. M., Wong, A. T., & Rosenberg, A. M. (2015). Diffraction-Enhanced Computed Tomographic Imaging of Growing Piglet Joints by Using a Synchrotron Light Source. *Comp Med, 65*(4), 342-347.

Rizzo, A. N., Belvitch, P., Demeritte, R., Garcia, J. G. N., Letsiou, E., & Dudek, S. M. (2020). Arg mediates LPS-induced disruption of the pulmonary endothelial barrier. *Vascul Pharmacol, 128-129*, 106677. doi:10.1016/j.vph.2020.106677

Rodrigues, R. S., Bozza, F. A., Hanrahan, C. J., Wang, L.-M., Wu, Q., Hoffman, J. M., . . . Morton, K. A. (2017). (18)F-fluoro-2-deoxyglucose PET informs neutrophil accumulation and activation in lipopolysaccharide-induced acute lung injury. *Nuclear medicine and biology, 48*, 52-62. doi:10.1016/j.nucmedbio.2017.01.005

Rojas, M., Woods, C. R., Mora, A. L., Xu, J., & Brigham, K. L. (2005). Endotoxin-induced lung injury in mice: structural, functional, and biochemical responses. *American Journal of Physiology-Lung Cellular and Molecular Physiology, 288*(2), L333-L341. doi:10.1152/ajplung.00334.2004

Rossi, A., Roviezzo, F., Sorrentino, R., Riemma, M. A., Cerqua, I., Bilancia, R., . . . Cirino, G. (2019). Leukotriene-mediated sex dimorphism in murine asthma-like features during allergen sensitization. *Pharmacol Res, 139*, 182-190. doi:10.1016/j.phrs.2018.11.024

Rubinstein, A. E., Gay, S., Peterson, C. B., Kingsley, C. V., Tailor, R. C., Pollard-Larkin, J. M., . . . Court, L. E. (2018). Radiation-induced lung toxicity in mice irradiated in a strong magnetic field. *PLoS One, 13*(11), e0205803. doi:10.1371/journal.pone.0205803

Rush, B., McDermid, R. C., Celi, L. A., Walley, K. R., Russell, J. A., & Boyd, J. H. (2017). Association between chronic exposure to air pollution and mortality in the acute respiratory distress syndrome. *Environ Pollut, 224*, 352-356. doi:10.1016/j.envpol.2017.02.014

Rush, B., Wiskar, K., Fruhstorfer, C., Celi, L. A., & Walley, K. R. (2018). The Impact of Chronic Ozone and Particulate Air Pollution on Mortality in Patients With Sepsis Across

the United States. *J Intensive Care Med*, 885066618804497. doi:10.1177/0885066618804497

Savitzky, A., & Golay, M. J. E. (1964). Smoothing and Differentiation of Data by Simplified Least Squares Procedures. *Analytical Chemistry, 36*(8), 1627-1639. doi:10.1021/ac60214a047

Schroeder, T., Vidal Melo, M. F., Musch, G., Harris, R. S., Venegas, J. G., & Winkler, T. (2008). Modeling pulmonary kinetics of 2-deoxy-2-[18F]fluoro-D-glucose during acute lung injury. *Acad Radiol, 15*(6), 763-775. doi:10.1016/j.acra.2007.12.016

Schuster, D. P., Kovacs, A., Garbow, J., & Piwnica-Worms, D. (2004). Recent advances in imaging the lungs of intact small animals. *Am J Respir Cell Mol Biol, 30*(2), 129-138. doi:10.1165/rcmb.2003-0213TR

Serkova, N. J., Rheen, Z. V., Tobias, M., Pitzer, J. E., Wilkinson, J. E., & Stringer, K. A. (2008). Utility of magnetic resonance imaging and nuclear magnetic resonance-based metabolomics for quantification of inflammatory lung injury. *American Journal of Physiology-Lung Cellular and Molecular Physiology, 295*(1), L152-L161. doi:10.1152/ajplung.00515.2007

Snigirev, A., Snigireva, I., Kohn, V., Kuznetsov, S., & Schelokov, I. (1995). On the possibilities of x-ray phase contrast microimaging by coherent high-energy synchrotron radiation. *Review of Scientific Instruments, 66*(12), 5486-5492. doi:10.1063/1.1146073

Srivastava, A., & Mannam, P. (2015). Warburg revisited: lessons for innate immunity and sepsis. *Frontiers in physiology, 6*, 70. doi:10.3389/fphys.2015.00070

Stieb, D. M., Burnett, R. T., Beveridge, R. C., & Brook, J. R. (1996). Association between ozone and asthma emergency department visits in Saint John, New Brunswick, Canada. *Environ Health Perspect, 104*(12), 1354-1360. doi:10.1289/ehp.961041354

Suresh, K., & Shimoda, L. A. (2016). Lung Circulation. *Compr Physiol, 6*(2), 897-943. doi:10.1002/cphy.c140049

Sweeney, T. E., Lofgren, S., Khatri, P., & Rogers, A. J. (2017). Gene Expression Analysis to Assess the Relevance of Rodent Models to Human Lung Injury. *Am J Respir Cell Mol Biol, 57*(2), 184-192. doi:10.1165/rcmb.2016-0395OC

Szarka, R. J., Wang, N., Gordon, L., Nation, P. N., & Smith, R. H. (1997). A murine model of pulmonary damage induced by lipopolysaccharide via intranasal instillation. *Journal of immunological methods, 202*(1), 49-57.

Takeda, K., & Akira, S. (2015). Toll-like receptors. *Curr Protoc Immunol, 109*, 14.12.11-10. doi:10.1002/0471142735.im1412s109

Thiesse, J., Namati, E., Sieren, J. C., Smith, A. R., Reinhardt, J. M., Hoffman, E. A., & McLennan, G. (2010). Lung structure phenotype variation in inbred mouse strains revealed through in vivo micro-CT imaging. *J Appl Physiol (1985), 109*(6), 1960-1968. doi:10.1152/japplphysiol.01322.2009

Thompson, B. T., Chambers, R. C., & Liu, K. D. (2017). Acute Respiratory Distress Syndrome. *New England Journal of Medicine, 377*(6), 562-572. doi:10.1056/NEJMra1608077

Thomson, E. M., Pilon, S., Guenette, J., Williams, A., & Holloway, A. C. (2018). Ozone modifies the metabolic and endocrine response to glucose: Reproduction of effects with the stress hormone corticosterone. *Toxicol Appl Pharmacol, 342*, 31-38. doi:10.1016/j.taap.2018.01.020

Tighe, R. M., Li, Z., Potts, E. N., Frush, S., Liu, N., Gunn, M. D., . . . Hollingsworth, J. W. (2011). Ozone inhalation promotes CX3CR1-dependent maturation of resident lung macrophages that limit oxidative stress and inflammation. *J Immunol, 187*(9), 4800-4808. doi:10.4049/jimmunol.1101312

Umeda, Y., Demura, Y., Ishizaki, T., Ameshima, S., Miyamori, I., Saito, Y., . . . Okazawa, H. (2009). Dual-time-point 18F-FDG PET imaging for diagnosis of disease type and disease activity in patients with idiopathic interstitial pneumonia. *Eur J Nucl Med Mol Imaging, 36*(7), 1121-1130. doi:10.1007/s00259-009-1069-1

Umeda, Y., Demura, Y., Morikawa, M., Anzai, M., Kadowaki, M., Ameshima, S., . . . Ishizuka, T. (2015). Prognostic Value of Dual-Time-Point 18F-FDG PET for Idiopathic Pulmonary Fibrosis. *J Nucl Med, 56*(12), 1869-1875. doi:10.2967/jnumed.115.163360

Umkehrer, S., Morrone, C., Dinkel, J., Aigner, L., Reiser, M. F., Herzen, J., . . . Hellbach, K. (2020). A proof-of principal study using phase-contrast imaging for the detection of large airway pathologies after lung transplantation. *Sci Rep, 10*(1), 18444. doi:10.1038/s41598-020-75185-4

Vanfleteren, L. E., van Meerendonk, A. M., Franssen, F. M., Wouters, E. F., Mottaghy, F. M., van Kroonenburgh, M. J., & Bucerius, J. (2014). A possible link between increased metabolic activity of fat tissue and aortic wall inflammation in subjects with COPD. A retrospective 18F-FDG-PET/CT pilot study. *Respir Med, 108*(6), 883-890. doi:10.1016/j.rmed.2014.04.001

Wernick, M. N., Wirjadi, O., Chapman, D., Zhong, Z., Galatsanos, N. P., Yang, Y., . . . Muehleman, C. (2003). Multiple-image radiography. *Physics in Medicine and Biology, 48*(23), 3875-3895. doi:10.1088/0031-9155/48/23/006

Wysokinski, T. W., Ianowski, J. P., Luan, X., Belev, G., Miller, D., Webb, M. A., . . . Chapman, D. (2016). BMIT facility at the Canadian Light Source: Advances in X-ray phase-sensitive imaging. *Phys Med*. doi:10.1016/j.ejmp.2016.07.090

Yao, Y., Zheng, Z., & Song, Q. (2018). Mesenchymal stem cells: A double-edged sword in radiation-induced lung injury. *Thoracic Cancer, 9*(2), 208-217. doi:https://doi.org/10.1111/1759-7714.12573

Zhong, Z., Thomlinson, W., Chapman, D., & Sayers, D. (2000). Implementation of diffraction-enhanced imaging experiments: at the NSLS and APS. *Nuclear Instruments and Methods in Physics Research, Section A: Accelerators, Spectrometers, Detectors and Associated Equipment, 450*(2), 556-567. doi:10.1016/S0168-9002(00)00308-9

Zychowski, K. E., Lucas, S. N., Sanchez, B., Herbert, G., & Campen, M. J. (2016). Hypoxia-induced pulmonary arterial hypertension augments lung injury and airway reactivity caused by ozone exposure. *Toxicol Appl Pharmacol, 305*, 40-45. doi:10.1016/j.taap.2016.06.003